In situ electron microscopy of nanomaterials dynamics in heterogeneous phase environments

By
Serin Lee

B.S.
Korea Advanced Institute of Science and Technology, 2019

Submitted to the Department of Materials Science and Engineering
in Partial Fulfillment of the Requirements for the Degree of

DOCTOR OF PHILOSOPHY IN MATERIALS SCIENCE AND ENGINEERING
at the

MASSACHUSETTS INSTITUTE OF TECHNOLOGY

MAY 2024

Authored by: Serin Lee
Department of Materials Science and Engineering
May 10, 2024

Certified by: Frances M. Ross
Professor of Materials Science and Engineering, Thesis Supervisor

Accepted by: Robert J. Macfarlane
Associate Professor of Materials Science and Engineering
Chair, Departmental Committee on Graduate Studies

In situ electron microscopy of nanomaterials dynamics in heterogeneous phase environments

By
Serin Lee

Submitted to the Department of Materials Science and Engineering on May 10, 2024
in Partial Fulfillment of the Requirements for the Degree of Doctor of Philosophy in Materials Science and Engineering.

Abstract

Engineered nanomaterials with desired properties and structures are indispensable to catalyze the processes of reliable energy conversion and storage systems for a sustainable future. These functional nanomaterials often experience dynamic physical and chemical changes during the operating cycles. Investigating the dynamics in real-time allows establishing structure-property-performance relationships to optimize the materials design. *In situ* transmission electron microscopy (TEM) is one of the most powerful tools to capture dynamic changes with high spatial and temporal resolution. More importantly, the reaction or operating conditions of the materials can be mimicked by controlling external stimuli of *in situ* TEM experiments, including control of temperature, electrochemical biasing, and exposure to liquid and gas. In this thesis, nanomaterials dynamics are investigated using *in situ* TEM coupled under the control of external stimuli in a heterogeneous phase consisting of solids exposed to a liquid or gas environment. First, I developed a temperature-dependent radiolysis model to explain the effect of temperature on the electron beam-induced radiolysis in liquid cell TEM. Radiolysis leads to the nucleation and growth of metal nanocrystals by reacting with the radicals, and I used the model to address the temperature-dependent chemical environment and corresponding kinetics of nanocrystal growth. The results demonstrated that the combination of microscopy and temperature-dependent modeling of the chemical environment can guide the analysis of the thermally controlled liquid cell TEM experiments. Moreover, the approach can be expanded to engineering the nanocrystal structure in lab-scale synthesis while acknowledging the differences compared with TEM experiments. Next, nanoscale electrochemistry under a controlled environment was discussed. In particular, the effect of temperature and substrate on electrochemical deposition is explained. *In situ* TEM results and modeling of the temporal evolution of the ion concentration demonstrated that the temperature accelerates the growth rate while it also controls the transition of growth modes. When 2D material graphene was used as a substrate for deposition, along with the classical nucleation and growth during the pulse on stage, transient growth and coarsening occurred, which could be attributed to the intrinsic properties of graphene to hold the charges. The results suggested that *in situ* TEM enables addressing the effect of electrochemical parameters and controlling nanoscale electrochemical phenomena. Finally, I applied the simultaneous acquisition of 2D projection and 3D topographic imaging in environmental TEM

(ETEM) setup to analyze the structure dynamics of supported catalytic nanoparticles during heating and gas exposure. Particle migration and coalescence dominated above an onset temperature that depends on the gas. 3D topography captured that particles migrate through the bulk support and across the support surface. The degradation of the support during particle migration was also observed in certain gas environments. In some gas environments, the particle coalescence via oriented attachment took place. These results showed that the combination of imaging modes can provide information to explain the catalyst degradation during operation. This thesis demonstrates that *in situ* TEM coupled with an understanding of the physical and chemical environments can provide insight into the nanostructure dynamics, which could contribute to revealing the degradation mechanisms of functional materials.

Thesis supervisor: Frances M. Ross
Title: Professor of Materials Science and Engineering

Acknowledgments

First, I would like to express my deepest appreciation to my advisor, Prof. Frances M. Ross, for her invaluable support, guidance, and encouragement throughout this journey. Whenever I encountered challenges, discussing them with her not only clarified my complexities but also sparked fresh motivations. Her kindest mind and enthusiasm as a scientist inspired me to pursue my career in academia. I am also thankful to the members of my thesis committee, Prof. Ju Li and Prof. Rob Macfarlane, for their support and insightful comments during my course of this research.

I am also truly grateful to the members of the Frances M. Ross group. I have been lucky to be part of this supporting and dedicated group where I can discuss science and have a great time together. Shu Fen Tan helped me start my journey in the field of liquid cell TEM and passed on her wisdom to be an independent researcher. Kate Reidy always shared invaluable resources and opportunities and brought happiness to the group. Julian Klein's guidance on Python coding has been a substantial part of my research. Also, I would like to thank Hanglong Wu for spending hours with me to discuss the challenging problems in liquid cell TEM. I learned the delicate technique of FIB from Baoming Wang, who helped me with the preparation of the most challenging samples. Alexandre Foucher provided helpful insights on the catalyst study and synthesis. Eugene Park's pastries always made our lives brighter, and I will never forget the birthday cake she baked for me. Including the rest of the group, Joachim Thomsen, Paul Miller, Zhenjing Liu, Pip Knight, Rishabh Kothari, and Haihui Lan, I would like to thank them for their feedback and for sharing their expertise on my research throughout the course.

I would also like to thank former group members and collaborators. It was my greatest pleasure to work with Nicholas Schneider, one of the kindest scientists I know, who made it possible to finish the radiolysis modeling. My research would be incomplete without Jeung Hun Park's invaluable support and resources. I would also like to thank Jasmin-Clara Bürger, who has been a dedicated collaborator. Hae Yeon Lee was my best officemate, and I would like to thank her for her guidance as a senior graduate student. I am also grateful to Yong Zhang, Aubrey Penn, and Zhenyuan Zhang at MRL for countless hours with me in the TEM room.

In addition to academic support, I would like to thank my friends in Boston for making my life as a graduate student happier by spending hours together, including Yehlin Cho, with whom I have been sharing the journey since high school. I have also been lucky to maintain a long-distance friendship with my friends outside Boston, Jiye Choi, Yeonsu Jung, Surim Kim, Seowoo Genevieve Ko, and Yoonji Lee, who always have my back. I am wholeheartedly grateful to my special collaborator, Jinwon Oh, who always supports me and believes in me more than I do. Lastly and most importantly, I am sincerely grateful to my parents, Jaehee Kim and Eunpal Lee, and my brother, Bumjoo Lee, for giving me the courage to finish my journey. Their endless love and support gave me the strength to overcome no matter what challenges I faced.

Serin Lee
May 10, 2024
Cambridge, Massachusetts

Table of Contents

List of Figures

List of Abbreviations

2D	Two-dimensional
3D	Three-dimensional
Ag	Silver
BF	Bright field
Cu	Copper
CV	Cyclic voltammogram
DEC	Diethyl carbonate
DF	Dark field
DMC	Dimethyl carbonate
E_A	Activation energy
E-beam	Electron beam
EC	Ethylene carbonate
EDLC	Electrochemical double-layer capacitance
EELS	Electron energy loss spectroscopy
ETEM	Environmental transmission electron microscope
HAADF	High angle annular dark field
NP	Nanoparticle
OA	Oriented attachment
OR	Ostwald ripening
Pd	Palladium
PMC	Particle migration and coalescence
Pt	Platinum
Pt/C	Platinum on carbon support
SE	Secondary electron
STEM	Scanning transmission electron microscope
TEM	Transmission electron microscope

List of Supplementary Materials

Supplementary Table S1: The reactions describing the radiolysis of aqueous $AgNO_3$ solution.

Supplementary Table S2: ΔI values of the plot shown in Figure 3-2.

Chapter 1. Introduction and Motivation

Functional nanomaterials are the key components of energy storage and conversion technologies as they catalyze reactions such as oxygen evolution in fuel cells,[1] electrolysis,[2] and catalytic converters for CO_2 reduction.[3] For the materials involved in these processes, the functionality arises from nanostructured components that must show a long lifetime without performance degradation during extended reaction cycles. However, the predicted performances of energy materials are often not achieved due to the complexity and dynamic nature of the structural and chemical changes during operation. Measuring the structure and composition of nanostructures before and after reactions is essential in developing these materials, allowing structure-property relationships to be established and used to optimize and guide next-generation design. Measuring structure during operation is even more powerful. This is because nanomaterials often show dramatic changes under reaction conditions including changes in size, morphology, composition, surface structure, and stability of the support when applying stressors such as voltage,[4] temperature,[5] and liquid and gas environments.[6] In this thesis, nanomaterials dynamics under various external stimuli in a heterogeneous phase, mainly solid material exposed to liquid or gas environment, are investigated using *in situ* transmission electron microscopy. I also demonstrate the applications of modeling for accurate assessment of the chemical and physical environment during the reaction as a foundation for interpreting *in situ* microscopy results. In doing so, I aim to establish a reliable platform for characterizing nanomaterials with enhanced performance and lifetime to pursue the development of sustainable energy sources.

1.1 *In situ* electron microscopy (TEM) of materials dynamics

In the last few years, transmission electron microscopy (TEM), especially *in situ* TEM, has provided a powerful tool for directly correlating chemical reactions and material transformation processes. (Figure 1-1) This technique offers critical insights for understanding the fundamental operation principles of materials that serve as a core function in energy storage and conversion technology. Furthermore, the development of TEM holders, highly efficient digital recording system and increased computational power have allowed rapid image acquisition at increased temporal resolution (≈1ms) under the external stimulus, making the *in situ* TEM techniques extremely valuable for probing the fast reaction dynamics.[7] Combined with the high resolution and the controllability of external stimuli, such as temperature, electrical bias, exposure to liquid and gas environment, *in situ* TEM has enabled establishment of a nanoscale laboratory to probe nanomaterial dynamics under environments relevant to the operating conditions of the materials. Moreover, adding unique external stimuli allows the characterization of unique properties of emerging nanomaterials for a sustainable future, such as probing plasmonic responses under light exposure for application in photocatalysts to harness solar energies.

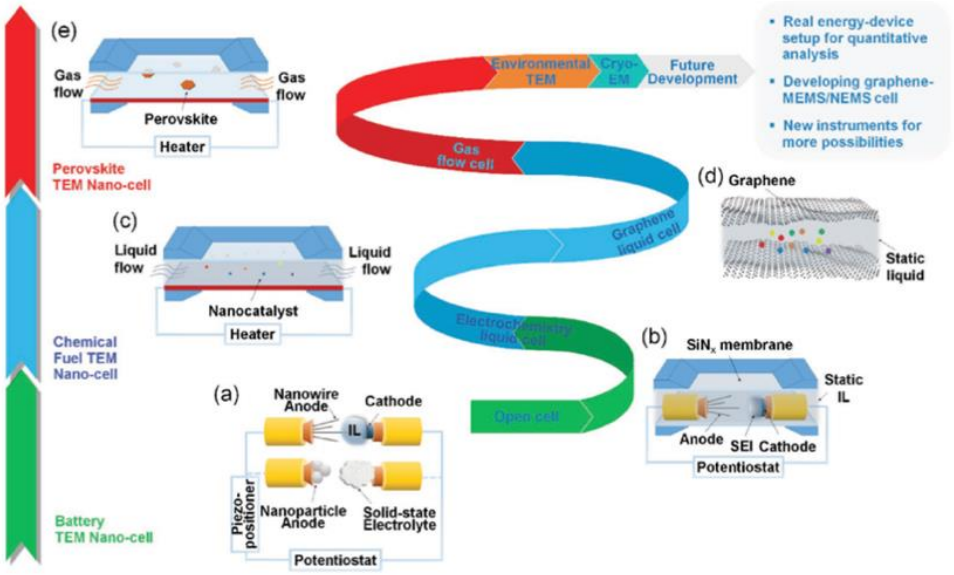

Figure 2-1. The development path of *in situ* TEM and their applications in investigating energy materials. Figure adapted from ref.[8].

1.1.1 Liquid Cell Transmission Electron Microscopy (TEM)

Liquid cell transmission electron microscopy (liquid cell TEM) allows the direct imaging of dynamic phenomena in a liquid environment with a combination of spatial and temporal resolution that is not achievable with other types of microscopy.[9,10] The development of modern microfabrication techniques has enabled the closed liquid cell approach in TEM. Williamson et al. demonstrated the electrochemical deposition of copper at the solid–liquid interface using liquid cells in 2003.[11] The liquid cell itself is a microfabricated enclosure that confines a liquid layer between two electron-transparent membranes with a controlled thickness.[12] Electrons passing through the encapsulated layer enables imaging and recording videos of objects within the liquid. Most of the liquid cells use silicon nitride as the electron transparent window material.

This closed liquid cell TEM provided new opportunities to study the physical and chemical evolutions occurring in samples in solutions.[7]

With the further development of the closed-cell, microelectromechanical system (MEMS) chips are developed, enabling the application of real-time external stimuli. The holder of the liquid cell chip holds the cell securely and also plays an important role in providing electrical connections between the patterned electrode or heater elements on the liquid cell and their external controllers. Combined with the control of parameters such as electron beam dose and dose rate,[13,14] electrical biasing,[15–21] liquid flow,[22] composition,[23–25] and temperature[26] liquid cell TEM has provided useful opportunities to explore reaction mechanisms in a wide range of topics in nanoscience, such as nanoparticle nucleation and growth,[13,14,27–36] self-assembly of nanostructures,[37–39] and structural changes in electrochemical energy materials.[15,18–21,40,41] Therefore, liquid cell TEM has enabled probing the dynamics of materials under various external stimuli which could also be used in understanding the degradation mechanisms of energy materials operated in liquid phase such as lithium-ion batteries[8] and electrochemical catalysts.[42]

1.1.2 Environmental Transmission Electron Microscopy (ETEM)

The gas-solid interaction is one of the most significant dynamics that has impact on the nanostructure's properties and performance. TEM with capabilities of controlling the gas environment, has enabled visualizing the dynamics of the interaction between gas and solid in atomic resolution. Controlled atmosphere conditions are achieved via two different approaches; using a gas holder with closed window cell, and using a differential pumping system to achieve open environment, namely, environmental TEM (ETEM), which we focus on in this chapter.

ETEM uses two pairs of apertures that are positioned above and below the specimen to prevent the gas flow into the microscope column while maintaining the gas exposure near the specimen area through differential pumping. Commercially available ETEM can be coupled with external stimuli such as temperature and electrical biasing, since the specimen holders with MEMS for the control of those stimuli are also compatible with ETEM microscopes. ETEM has been employed to understand a range of fundamental phenomena in materials science, including oxidation,[43] reduction,[44] and crystal growth[45] in a gas phase. In particular, probing heterogeneous catalyst in a gas phase using ETEM has been actively employed to understand a range of fundamental phenomena that can take place during the operation of catalytic materials. [46–49]. Catalyst materials usually consist of metal nanoparticles on support, and they dynamically react to the environmental changes including temperature and gas by going through behaviors such as sintering and dispersion,[50–53] particle dissolution, [42,54] reshaping of meal nanoparticles,[55] composition evolution, [6] and reconstruction of the support[56–58] which could affect the performance. In this regard, ETEM with a controlled gas and temperature environment allows capturing the dynamic interaction between the gas, nanoparticle, and support, and its impact on the kinetics of the catalyst degradation mechanisms.

1.2 Thesis Overview

This thesis focuses on the goal of elucidating the dynamic correlation between structure, property, and performance of functional nanomaterials using *in situ* electron microscopy. I present the spatial and temporal dynamics of the materials under the reaction conditions realized by external stimuli, including electron dose, temperature, electrochemical bias, and exposure liquid/gas. The thesis is arranged as follows: In Chapter 2, I summarize the effect of temperature

on the electron beam induced nanocrystal growth in liquid phase. I develop the temperature-dependent radiolysis model using the kinetic model for radiolysis and temperature-dependent parameters. I showcase the analysis of the kinetics of metal nanocrystal growth using the liquid cell TEM data and the developed radiolysis model. In Chapter 3, I discuss the nanoscale electrochemistry under a controlled environment, including temperature and the substrate as the control parameter. Along with the accelerated growth rate of the electrochemically deposited metal nanostructures, I demonstrate the temperature effect on the transition of growth modes using the modelling of temporal evolution of concentration profile. Transient deposition, coarsening, and dissolution of nanoparticles electrochemically grown on graphene substrate is also discussed, considering the intrinsic chemical and physical properties of graphene. In Chapter 4, I summarize the structural dynamics of nanoparticles in a gas environment using environmental TEM couples with 2D projection image and 3D topographical images. I explain the interplay between particle-support-gas and how to apply those findings to design catalyst materials. In Chapter 5, I discuss the challenges to overcome in order to expand the scope of electrochemical liquid cell TEM, mainly focusing on the effect of organic components in the system and the role of pulse duration. Furthermore, I discuss the future direction of *in situ* electron microscopy using light stimuli and spectroscopy to analyze the optical properties of materials and their applications.

Chapter 2. Temperature-Dependent Electron Beam-Induced Nanocrystal Growth

This chapter is adapted with permission from ref. 26

Lee, S., Schneider, N. M., Tan, S. F., & Ross, F. M. Temperature Dependent Nanochemistry and Growth Kinetics Using Liquid Cell Transmission Electron Microscopy. *ACS nano*, *17*(6), 5609-5619 (2023).

Liquid cell transmission electron microscopy (liquid cell TEM), with its high temporal and spatial resolution, has been used extensively to capture and quantify the complicated kinetics of nanocrystal formation in liquids.[30,31,35,36,59–61] A common route to form nanocrystals in liquid cell TEM is via the reaction of electron beam-induced radiolysis products with metal ions in the solution. In this liquid cell TEM growth process, experimental parameters including electron dose rate affect the growth kinetics and morphology.[13,28,34] Temperature is expected to be one of the most important parameters and the effects of temperature on nanocrystal formation[62] and on electron beam-induced radiolysis[63] have been reported in literature. To quantify the effects of temperature on a dynamic process imaged within the liquid cell, we have carried out a series of crystal growth experiments and simulations at different temperatures using a liquid heating system that provides a controlled thermal environment at the imaged area. We develop a radiolysis simulation model by as well as including temperature effects on reaction kinetics to assess the effects of temperature-dependent local chemistry. We show how the radiolytic environment changes with temperature and solution composition, including effects that show

complex, non-monotonic dependencies on temperature and dose rate. Combining our observations and calculations of radiolysis species, we discuss the morphology changes in terms of the balance between nucleation, growth, surface diffusion and surface reaction rates at different temperatures. These results suggest strategies for the design and interpretation of liquid cell experiments that measure the structural and compositional evolution of materials with temperature-dependent kinetics, and more broadly suggest that liquid cell TEM can provide insights into control of nanocrystal morphology in lab-scale synthesis using the understanding of the temperature dependent chemical environment and growth morphologies obtained from *in situ* experiments.

2.1 Temperature Control in Liquid Cell TEM and Application

One of the critical objectives in ongoing liquid cell TEM experiments is temperature control, since temperature arguably represents the most important thermodynamic variable.[64] Controlling the temperature in liquid cell TEM, especially elevating the temperature by heating, enables experiments that probe phase transformations[65] and phenomena not present at room temperature,[66,67] as well as allowing more quantitative analysis of reaction kinetics and mechanisms.[62,68] Temperature is a critical variable in understanding the physics of structural evolution of nanomaterials, since an Arrhenius temperature dependence can give information on the rate-determining step of the overall process. Temperature-dependent electrochemical processes play a key role in the operation of energy materials.[69,70] Finally, using temperature as a control knob offers fundamental insights into growth kinetics, including design of strategies for synthesis and to achieve structural and compositional control of materials with temperature-dependent kinetics.[16,71–73] The control of temperature must be coupled with an understanding of

how the resulting phenomena in the liquid cell relate to larger scale, real-world processes. At room temperature, it has been shown how the radiolytic and chemical environment within the liquid cell can be controlled during nanoparticle reactions[74] so that the results are relevant to the environment present in *ex situ* processing. We therefore anticipate that quantifying temperature effects on the chemical environment in liquid cell TEM will increase the relevance and impact of liquid cell experiments to lab-scale processes such as nanoparticle synthesis.

2.1.1 Heating Capabilities and Temperature Effect in Liquid Cell TEM

Although most liquid cell experiments to date have been carried out at room temperature, several strategies have been developed for temperature control in TEM experiments: Joule heating, equilibration with a remote thermal source, photon heating, and thermal fluid circulation.[64] The most commonly used is Joule heating, where calibration of resistance values allows a Joule heater to be used to both heat and measure temperature. In any heating experiment we need to consider all the ways that temperature can affect the result. This includes quantifying temperature as a function of position within the liquid, temperature effects on the liquid dynamics, and temperature effects on the interaction of the imaging electrons with the liquid and sample.

2.1.2 Temperature-Dependent Factors in Radiolysis

The temperature dependence of electron beam effects is particularly important to quantify since beam effects occur in every experiment, affecting the solution chemistry or driving reactions. In liquid cell TEM, the irradiating electrons change the chemistry of the suspending medium, typically an aqueous solution, by creating molecular and radical products such as H_2, O_2, and e_h^-

(hydrated electrons) by radiolysis. This is modelled[75] by incorporating the rate at which incident electrons transfer energy to water and create radiolysis species, and the subsequent diffusion and interactions of these species with each other and with other molecules present. All steps of this process are temperature-dependent: the reaction rates scale with an Arrhenius behavior and the rate of generation or destruction of the primary products (the G-value, or number of molecules created or destroyed per 100 eV), depends on temperature. [63] Thus, it is possible to improve radiolysis modelling by including the temperature dependence of the component processes. Radiolysis models become even more useful for practical experiments if we include the effect of all the species initially present in the aqueous solution. This has been achieved in some cases, such as the inclusion of chloride ions[28,76] as well as reactions between a polymer, a radical scavenger and gold. Temperature effects have not been included in these calculations. To understand the influence of temperature and ion species on a liquid phase process, temperature-dependent radiolysis should be considered in the presence of the complete set of species present, such as metal ions. This will result in more quantitative knowledge of the interactions between the electron beam and an irradiated liquid medium under thermal conditions.

2.2 Structural Evolution of Silver in Liquid Cell TEM at Different Temperatures

To quantify the effects of temperature on a dynamic process imaged within the liquid cell, we have carried out a series of crystal growth experiments and simulations at different temperatures using a liquid heating system that provides a controlled thermal environment at the imaged area. We use a well-studied system, Ag nanocrystal growth that is driven by the changes in redox environment caused by the electron beam. In this process, Ag^+ ions in aqueous solution are reduced by radiolytically generated species and then undergo nucleation and growth to form

nanocrystals. Nanocrystal growth is governed by multiple processes, including the local chemistry due to radiolysis, the formation rate of reduced Ag (Ag^0), nucleation of clusters, the diffusion and attachment of Ag atoms to the nanocrystal surface, surface diffusion, and the reaction rate at the surface.[14] The experiments, therefore, provide opportunities for assessing the role of temperature and comparing with an enhanced model for radiolysis effects. We find that nanocrystal growth takes place over a range of temperatures but with substantial changes in growth rate and morphology of the deposited material. To assess the effects of temperature-dependent local chemistry, we extend the radiolysis simulation model by including both silver and nitrate ions and their derived species in the reaction set, as well as including temperature effects on reaction kinetics.

2.2.1 In situ TEM of Silver Nanocrystal Growth

We carried out Ag nanocrystal growth by irradiating silver nitrate solution, using the radiolytically generated species to reduce the metal ions and drive nanocrystal nucleation and growth. Typical results are shown in Figure 2-1, which displays a time series of bright field images of Ag nanocrystal growth at three different temperatures during irradiation of a 2μm diameter region of a cell filled with 0.01 M $AgNO_3$ solution. The does rate, ψ, can be calculated from the electron flux using the following equation, $\psi = \frac{10^5 SI}{\pi a^2}$ (Gy/s), where S ($MeV \cdot cm^2/g/electron$) is the density-normalized stopping power in the medium, I (A) is the beam current and a (m) the beam radius. The factor 10^5 ($m^2 \cdot electron \cdot Gy \cdot g/cm^2/MeV/C$) converts between units. The estimated constant dose rate using the equation is 2.8×10^7 Gy/s. We limited irradiation of the region of interest between each experiment and observed no nucleation and

growth of crystals after this period, as expected since no reducing agents are present in the solution other than the beam-induced species.

Clear differences are visible in the reaction as the temperature is varied. At room temperature, growth takes place by formation of small particles or nanocrystals.[13,14,28–33,35,36] At a higher temperature of 50 ˚C the morphology is similar but both the number of visible nuclei and the growth rate of nanocrystals are larger than at room temperature. Room temperature growth is shown in Figure 2-1. Visible particles appeared after around 72 seconds of electron beam irradiation. At 50 ˚C, shown in Figure 2-1b, particles became visible more rapidly (24 seconds). The nanocrystal contrast becomes darker as their radii increase, which suggests that the crystals grow in three dimensions. We therefore assume hemispherical growth on the SiN_x window of the cell. Hemispherical particles are of course expected from considerations of interfacial energy, which favors minimizing the solid-liquid interface area.[77]

The growth of hemispherical particles with rates higher at 50 ˚C than at room temperature is consistent with a systematic variable-temperature study of beam-induced growth in Au.[62] In that case, the higher growth rate at elevated temperature was explained through a shortening of the time over which nucleation occurred followed by faster growth kinetics. The decrease in nucleation duration was attributed to a faster drop in supersaturation (the ratio between the metal atom concentration and equilibrium solubility) during nucleation at higher temperature. As we discuss below, the change in morphology we observe at higher temperatures suggests that factors other than solubility play a role in our Ag experiments, and we will describe possible effects of changes in the reaction rates and surface diffusion.

At an even higher temperature of 70 ˚C (Figure 2-1c), the growth mode is distinctively different. The most notable feature is an elongated nanocrystal growth morphology, although a few

hemispherical particles are also present. We refer to the structures as blade-like dendrites, a terminology used in other metal growth studies that show approximately similar structures.[78,79] The experiment shown in Figure 1c is one of several in which we consistently observed similar dendrite growth at higher temperatures.

To quantify the temperature-dependent time scale of nanocrystal growth, we tracked the volume growth of nanocrystal features at different temperatures (Figure 2-1 d, for which a log scale plot is shown in Supporting Information Figure S2 to clarify the lower rate data points). The volume growth at room temperature and 50˚C were calculated by taking the average of 10 typical (and non-overlapping) particles indicated by white circles in Figure 2-1a and 2-1b. We assume these are heterogeneously nucleated on the SiN_x window of the cell as no Brownian motion was observed, [13,29,34] hence the volumes were calculated by measuring the diameters of the particles and taking the corresponding volume of a hemisphere. For experiments at 70 ˚C, the volume growth of a single dendrite branch was tracked, estimating its thickness by comparing its contrast with that of other nanocrystals of assumed (hemispherical) thickness. Measuring this single nanostructure gives an estimate of the high growth rate possible under the dendrite growth conditions. As shown in Figure 2-1e, the time scale of propagation of the dendrite is below 0.2 seconds. It is clear from the plot that the time scale of nanocrystal growth at 70 ˚C, even considering only this one nanostructure, is 10^6 times faster than at room temperature, while the rate at 50 ˚C is 3 times higher than that at room temperature when the growth started, illustrating an extremely strong role of temperature in elevating this beam-induced process rate. The symmetry and apparent uniform thickness of this dendrite in Figure 2-1e suggest that it contains {111} top and bottom facets. This is consistent with surface energy considerations: {111} surfaces of silver have the lowest surface energies, followed by {110} and {100},[52] in the

absence of any capping agents preferentially binding to specific facets. Similarly, the equilibrium structure of Ag nanowires was calculated[53] to consist of {111} sidewalls. We therefore expect that dendrite in Figure 2-1(e), and presumably others, are generally {111} terminated although smaller areas, including possibly the growth surface, may be composed of facets with higher energy such as {110} and {100}.

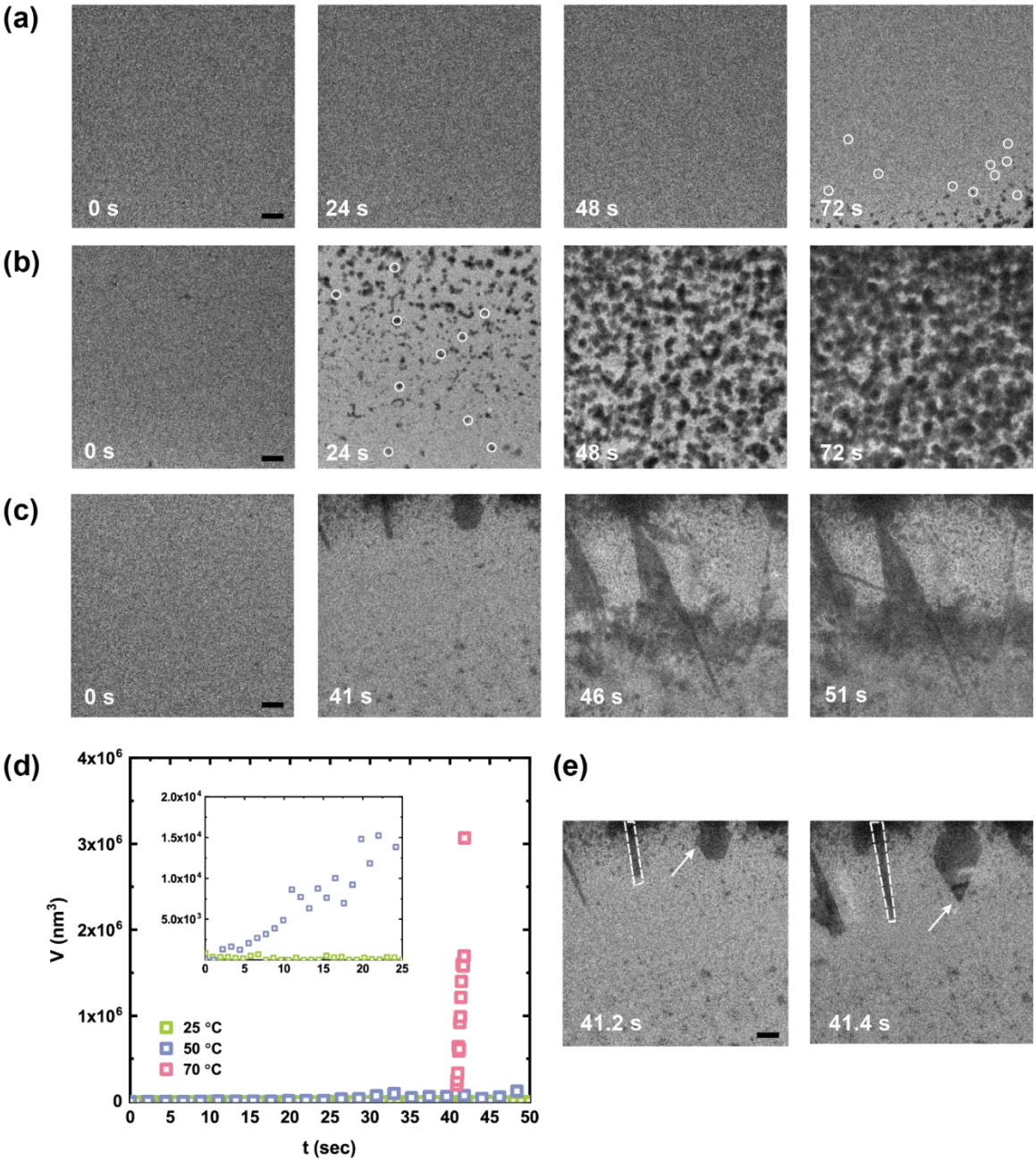

Figure 2-1. Growth of Ag nanocrystals at different temperatures. Time series of *in situ* TEM images showing the growth of Ag nanocrystals during beam exposure at (a) 25 ˚C, (b) 50 ˚C, and (c) 70 ˚C. Note the different time scales in (c). In (a), the appearance of islands at the bottom of the image will be discussed below. (d) Calculated volume of a nanocrystal versus time at different temperatures. The average volumes at 25 ˚C and 50 ˚C were calculated using the measured radii for each frame and assuming hemispherical shapes. Ten particles that could be tracked without overlapping with neighboring particles, indicated in white circles in (a) and (b), were used in this calculation. The volume at 70 ˚C was calculated by measuring the projected area of the crystal indicated by dotted lines in the image and estimating the thickness by comparing its pixel intensity with a hemispherical island with known thickness. Note the orders of magnitude change in the volume and the sharp slope of the curve of nanocrystal growth at 70 ˚C. The inset plot shows the volume versus time at 25 ˚C and 50 ˚C. (e) Images showing blade-like dendrite growth occurring within 0.2 s. Note the arrows indicating a dendrite showing 120 ^{o} and 60 ^{o} angles and a constant thickness; this symmetry is consistent with top and bottom facets being {111}. The solution used was 0.01 M aqueous $AgNO_3$ and the electron dose rate was 2.8×10^7 Gy/s. Images (a), (b), (c) and (e) are recorded in bright-field conditions. Scale bars are 200 nm.

We now discuss further details of this higher-temperature growth mode. Figure 2-2 shows a time series of the blade-like dendrite growth at 70 ˚C; note that Figure 2-2a, c and Figure 2-2b have a different times between frames. After growth of discrete small particles, more deposition propagates from the upper left corner of the frame (Figure 2-2a). After 24 seconds (Figure 2-2b) a blade-like dendrite forms, propagates and grows additional branches. At longer times (Figure

2-2c), another platelike crystal partly covers the frame. These metal dendrites, which represent a highly non-planar growth front, are similar to those often observed in liquid-to-solid phase transformations. In these cases, growth can be driven by ion concentration gradients (electrochemical), temperature gradients (solidification), localized catalytic surfaces (as in catalytic nanowire growth), localized stress effects (extrusion of microfilaments) or combinations of these factors.[80] To analyze the phenomena that may dominate in the liquid cell environment, we now consider changes in the overall growth rate arising from radiolysis, since this determines the supply of Ag^0 needed for subsequent growth.

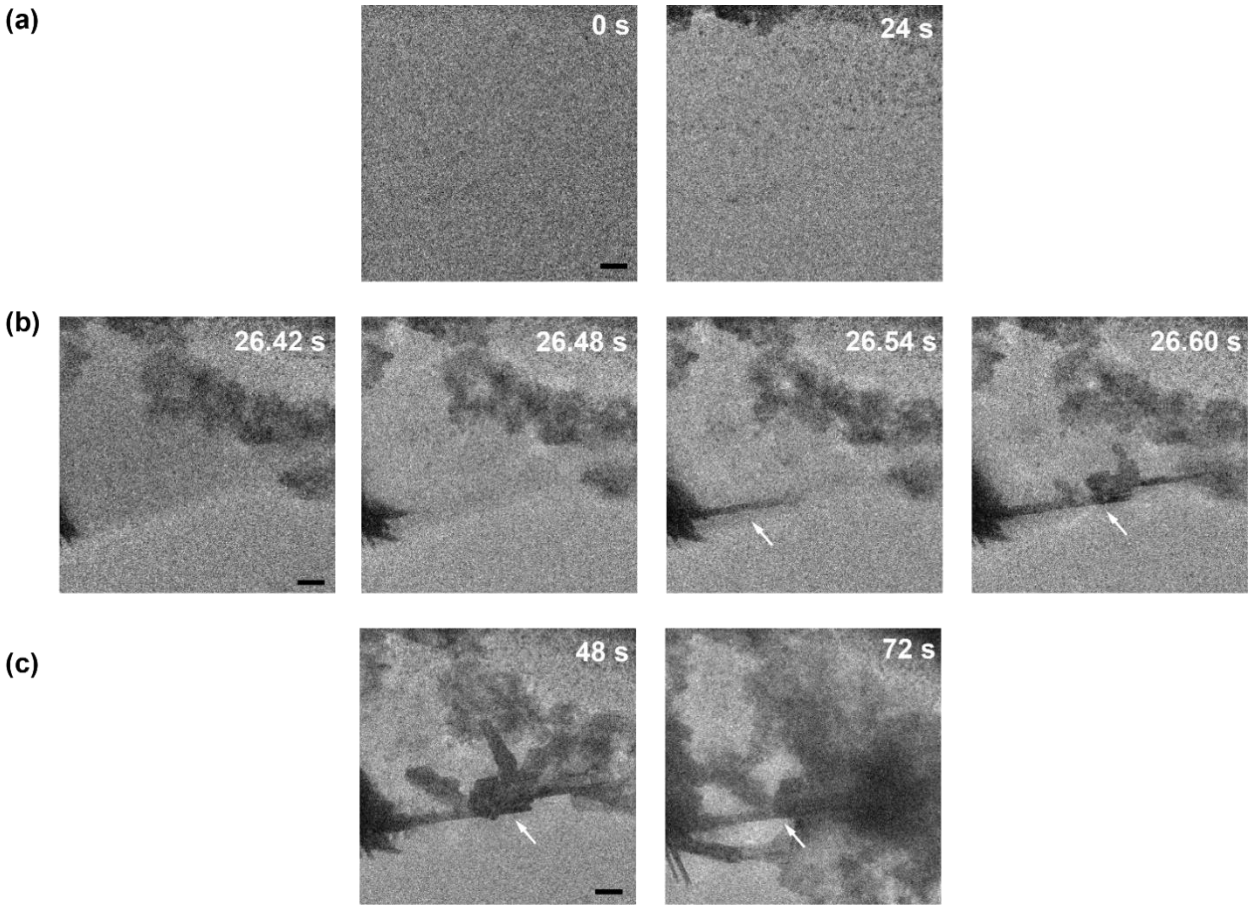

Figure 2-2. Growth of Ag blade-like dendrite at 70 ˚C. (a) and (c) Time series of liquid cell TEM images showing the overall growth of Ag, with 24 seconds between images. (b) The onset of Ag

blade-like dendrite growth within a second. Blade-like dendrites are indicated as white arrows. The solution used was 0.01 M aqueous $AgNO_3$ and the dose rate was 2.8×10^7 Gy/s. Images are recorded in bright-field. The time is given since irradiation started. Scale bars are 200 nm.

2.2.2 Developing Temperature-Dependent Radiolysis Model

To understand the chemical environment of Ag nanocrystal formation, we calculated the temperature-dependent steady state equilibrium concentrations (C_{ss}) of the radiolysis species as well as the cation (silver) and the counter ion (nitrate). The relative concentrations of the equilibrium radiolysis products is expected to influence nanocrystal growth since the ratio between reducing agent and oxidizing agents determines the redox chemistry environment. We used the complete set of reactions for 0.01 M aqueous $AgNO_3$ to solve the series of reaction rate equations implemented with temperature-dependent parameters. To compute the concentrations of radiolysis products and Ag ion in the presence of nitrate, we use the kinetic model of Elliot and McCracken implemented by Schneider et.al.[75] to include the dominant reactions and species associated with irradiation of silver nitrate. The kinetic model includes the species e_h^-, H•, H_2, H_2O, H_2O_2, HO_2•, HO_2^-, H^+, O_2, $O_2^{\bullet-}$, OH•, OH^-, Ag^0, Ag^+, NO_2•, NO_2^-, NO_3^-, $NO_3^{\bullet 2-}$, HNO_2, and HNO_3 as reactants and products of the reactions. The redox reactions of Ag species we include are the Ag^+ reaction with e_h^- and H• and the Ag reaction with OH• and O_2. The Ag^+ precursor is reduced to Ag^0, whereas Ag^0 can be oxidized to re-form Ag^+. To fully account for the ion species in the solution, we include nitrate species in the reaction set. Nitrate species react with water radiolysis species with rates similar to those of Ag^+ with water radiolysis species. $O^{\bullet-}$, O_3, HO_3•, and O_2• are not included in the model due to the lack of kinetic data at higher temperatures and low concentrations at neutral and low initial pH.[63] Modeling the

temperature dependence involves two modifications. We scaled the reaction rates with an Arrhenius relationship[63] by using the known reaction rates at room temperature and the activation energy from literature to estimate the reaction rates at intermediate temperatures. We also include the dependence of G-values on temperature, which we interpolate from known values at room temperature and 100 ˚C. [63]

The initial concentrations used for the calculations were C_{H2O} (0) = 55.56M, $C_{H+}(0) = C_{OH-}(0) = 10^{-7}$M, $C_{Ag+}(0) = C_{NO3-}(0) = 0.01$ M , $C_{O2}(0) = 0.255$ mM. The last value is based on an aerated solution as expected from the sample preparation procedure. This model accounts for forming the primary radiolytic products (e_h^-, H^+, OH^-, H_2O_2, H•, OH•, H_2, HO_2•) via G values and the longer-time kinetic reactions. The G-values are defined as the moles of each radiolysis species that are created (+) or annihilated (-) per 100 eV of energy absorbed; they are determined empirically for pure water, although not at dose rates as high as those used in electron microscopy. The temperature-dependent G-values are interpolated from the known value at different temperatures. [63] The reaction rates are scaled with Arrhenius behavior by using the reaction rates and activation energy at room temperature from literature. The rates of reactions with unknown activation energy were scaled with the average activation energy of known reactions. The full list of reaction and the boundary conditions used for the calculation are listed in Supplementary Table S1 with rate constant, known Arrhenius constant and activation energy. The constants for these and additional reactions can be found in the NIST databases[81] unless stated otherwise. The reaction sets from 49-57 are taken from Horne et al.[82] Note that reaction 47 corresponds to oxidation of Ag^0, and reduces the rate of Ag^0 formation,[83] and therefore we used this reaction as the counteracting reaction of the metal ion reduction.

Using the temperature-dependent rate constants, G-values, and kinetic equations in the table, we formulated a set of differential equations of the form

$$\frac{\partial C_i}{\partial t} = -\sum_j k_{ij} C_i C_j + \sum_{j,k \neq i} k_{jk} C_j C_k + R_i \qquad \text{(Eq. 1)}$$

to describe the temporal evolution and calculate the steady state equilibrium concentration of 20 radiolysis constituents. In the above, k_{ij} are the reaction rate constants. The first two terms on the right-hand side account for destruction and production of species *i* through chemical reactions. The last term,

$$R_i = \rho \psi \frac{G_i}{F} \quad \text{(M/s)} \qquad \text{(Eq. 2)}$$

is the volumetric production rate of species *i* due to irradiation (radiolysis) in the region illuminated by the beam. G_i is non-zero only for the primary products and is temperature dependent. ρ is the density, ψ is the dose rate and F is Faraday's constant. Since the concentration of water is much greater than that of the radiolysis products, we can simplify the mathematical model by assuming that water acts as a solvent. This allows us to describe the system as a set of first order reactions. This assumption is implemented in the reaction rates by dividing out the water concentration when water is a reactant (reactions 6, 10, 18, 21 etc.).

The plots in Figure 2-3a-c show the calculated steady state concentrations (C_{ss}) of the radiolysis products, Ag species, and nitrate species for aerated 0.01 M aqueous $AgNO_3$ solution experiencing a dose rate of 2.8×10^7 Gy/s. In Figure 2-3a, temperature dependent C_{ss} of the main redox species along with H_2 and H_2O_2 are plotted to show that the C_{ss} values decrease by 20-90 % when the temperature increases from room temperature to 70 ˚C. The change in the concentration of the main redox species is a result of interplay between multiple factors. However, it can be understood most easily by considering that the rates of the reactions that

remove those species are exponentially dependent on temperature, whereas the creation rates (G-values) are linearly scaled (within 15%).

Temperature-dependent C_{ss} of Ag species are shown in Figure 2-3b. It is evident that the equilibrium concentration of Ag^0 increases almost 3 times on going from room temperature to 70 ˚C. Note that the dotted line showing the concentration ratio of Ag^+ is relatively constant as the temperature changes. The absolute concentration of Ag^+ is significantly larger than Ag^0 but we do not expect it to change much with temperature in the experiment because Ag^+ is continuously replenished from diffusion from the bulk of the $AgNO_3$ solution. From the relative increase in C_{ss} of Ag^0 and the redox agents in Figure 2-3c, it appears that higher temperature leads to a redox environment with stronger trend in reducing the metal ions and therefore forming nanocrystals.

We finally consider the combined effect of dose rate and temperature on Ag nanocrystal growth. In Figure 2-3d we plot the Ag^0/Ag^+ concentration as a function of temperature and dose rate. At every dose rate a relative increase in the Ag^0/Ag^+ concentration with temperature is still visible. However, Ag^0/Ag^+ is lowest around the experimental condition used (10^7 Gy/s), and is larger at both low and high dose rates (10^5 to 10^{11} Gy/s can be considered a typical dose rate range for liquid cell TEM experiments). Interestingly, the dependence on temperature is more pronounced at low and high dose rates. The valley along the dose rate axis is a result of 57 interlinked reactions, and although understanding the details is challenging, the overall behavior of the system in terms of Ag deposition is a result of the rate of reactions where Ag^0 and Ag^+ are reactants or products. At relatively low dose rate, the oxidizing reaction of Ag^0 with O_2 and OH• appears dominant over the reduction of Ag^+ to Ag^0. On the other hand, G-values producing the reducing species e_h^- and H• become more dominant at higher dose rate, which could make the reduction of Ag^+ to Ag^0 relatively more important. This surprising outcome of the interlinked

reactions is that the growth rate is not necessarily monotonic with respect to dose rate, and in general the effect of dose rate and temperature should be considered together using a calculation that includes a full set of the species present.

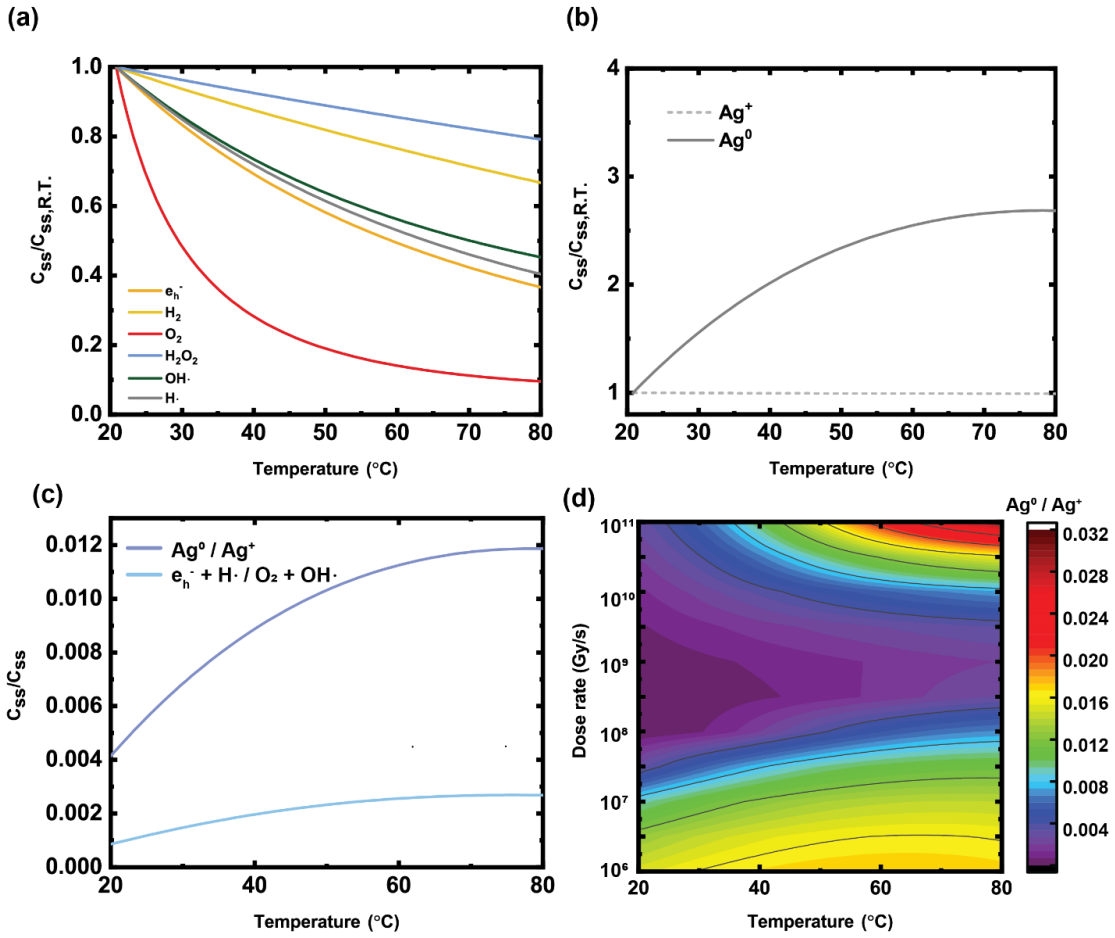

Figure 2-3. Temperature dependent radiolysis simulation model results. (a) Steady-state equilibrium molar concentration (C_{ss}) of the main redox species (e_h^-, OH•, H•, and O_2), H_2, and H_2O_2. (b) C_{ss} of Ag^+ and Ag^0 (reduced Ag) at different temperatures divided by the C_{ss} at room temperature (C_{ss} / $C_{ss,\,R.T.}$). (c) Ratio between C_{ss} of Ag^0 and Ag^+, and ratio between the sum of reducing agents (e_h^-, H•), and the sum of oxidizing agents (O_2, OH•). The conditions used in the simulation match the experimental conditions of aerated 0.01 M aqueous $AgNO_3$ solution and

dose rate 2.8×10^7 Gy/s. (d) Heat map of dose rate and temperature showing the ratio between the C_{ss} of Ag^0 and Ag^+.

2.2.3 Revealing the Growth Kinetics of Silver Nanocrystal

Having calculated the expected changes in chemical environment with temperature, we now discuss the possible factors that could lead to the dynamic change of growth mode we observe at higher temperature. As described in literature, several factors may determine the growth rate and morphology of the reaction we have measured: diffusion of ions from the bulk solution,[14,28] reduction of ions within the beam,[13,29,34] diffusion of reduced ions,[14,34] nucleation of clusters, which depends on critical nucleus size and diffusion on the substrate,[13,27,62] and incorporation at the cluster surface, which depends on adsorption and diffusion on the cluster surface[84–86]; all these factors are expected to depend on temperature.

We initially consider the importance of diffusion from the bulk solution in our particular experimental conditions. At lower temperatures we notice that the formation of nanocrystals tends to occur via the propagation of a growth front. Figure 2-4a shows the continued progression of Ag growth for the experiment shown in Figure 2-1a. The propagation of a growth front from the lower right corner of the frame is clearly visible as additional nuclei continue to form. To track the temporal and spatial dependence of growth, we plot particle radius versus time in Figure 2-4c. The time shift between nucleation events reflects the progression of the growth front across the field of view, although after their individual nucleation times, the nanocrystals show similar linear relationships between radius and time (Figure 2-4d) until their growth slows, as will be discussed further below. In the experiments, the electron beam illuminates a circular area of radius 3 μm, larger than the area recorded on the camera (a square of size 1.7×1.7 μm^2

at the magnification used). We observe growth front propagation most clearly when the beam is off center compared to the camera. Furthermore, low magnification images recorded after the end of a growth experiment show a 'ring' of Ag deposited around the beam boundary. Differences between a beam-induced reaction near the beam boundary and at the center of the beam are well known.[87,88] Furthermore, the chemical environment in water at the edges of the illuminated area is different from that at the beam center due to the species-dependent diffusion of radiolysis products.[75] The reaction of ions arriving from the bulk liquid on reaching the edge of the illuminated area result in enhanced growth at the beam boundary and spatially and temporally dependent growth rates within the illuminated area, consistent with our observations. We first estimate whether the diffusion of silver ions or reduced silver through the solution could be a limiting process in our experiments. Diffusion of ions in liquid phase is modeled by the Stokes-Einstein equation, $\mathrm{D} = \frac{\mathrm{k_B T}}{6\pi\eta \mathrm{r}}$, where the diffusion coefficient D depends on Boltzmann's constant k_B, the absolute temperature T, the dynamic viscosity η and an assumed radius r of the ion, assumed spherical. Along with the direct linear dependence on temperature, D has another temperature dependence because the viscosity of water decreases by a factor of 2 (from 0.89 to 0.40×10^{-3} Pa·s) on going from room temperature to 70 ºC).[89] Temperature effects on the diffusivity of ions in liquid cell TEM have not been measured directly. Electrochemical nucleation and growth measurements for copper have confirmed D values for copper ions, and by implication viscosity, consistent with bulk values.[90] However, viscosity values that are derived from nanoparticle motion show extreme discrepancies between thin water films in the liquid cell and bulk values: values obtained are in the range of 1MPa·s for water at room temperature in liquid cell,[91–93] orders of magnitude larger than the bulk viscosity. The mechanism of decreased nanoparticle mobility is unclear, but hypotheses include viscous drag near the

window surface, surface roughness, and strong nanoparticle-window interactions.[92] For Ag^+ ion diffusion in our experiments, we assume a bulk D value and that this value scales with temperature with the temperature dependence of viscosity in bulk water. Thus we assume D = 1.7×10^{-9} m^2 s^{-1} at room temperature[94] and 2 × (343 K /298 K) = 2.3 times this value at 70 ºC. This leads to estimates for diffusion length, $r = \sqrt{2Dt}$, of 30 μm for one second at room temperature and 45 μm at 70 ºC.

At our highest growth rates, for example in Figure 2-1d, the volume change of one dendrite at 70 ˚C from t= 40.8 to 41.8 s is 3.0×10^6 nm^3, which corresponds to 1.8×10^8 ions. Extrapolating the dendrites in the field of view across the illuminated area suggests around 30 dendrites in total. If we assume a liquid thickness of 200 nm, for 0.01 M concentration of $AgNO_3$, this number of ions occupies a cylinder of radius around 30 μm. Since the diffusion length exceeds this, we therefore roughly estimate that the supply by diffusion of silver ions is not a limiting factor for growth at higher temperatures. At lower temperatures the growth rates are orders of magnitude smaller while the ion diffusion is only twice as small. We conclude that ion supply to the irradiated area is not limiting at any temperature, and that the change in ion diffusivity with temperature is insufficient to cause the change from particle growth to rapid dendrite growth.

Once within the beam, the supply of material to the growing clusters is determined by the radiolysis process. Previous liquid cell studies[13,28,34] have shown that controlling the dose rate can switch solution-phase crystal growth between reaction-limited and diffusion-limited growth. Increasing temperature has an effect similar to increasing dose rate, in that the rate of production of Ag^0 is increased. However, the calculations in Figure 2-3 show that the concentration of Ag^0 available for growth increases by at most a factor of 3. This does not match the overall growth

rate increase, suggesting that the change in Ag^0 concentration caused by the temperature rise may contribute but is not the main cause of the changes in growth mode at higher temperature. Instead, we suggest that changes in the relative rates of nucleation and growth may play the most direct role in the temperature dependence of this growth experiment. We develop this argument by considering the factors affecting relative nucleation and growth rates of neighboring nanocrystals. Figure 2-4b shows growth in the presence of pre-existing nuclei, and can be compared with the case already shown, Figure 2-4a, which took place on a surface on which no nuclei were present initially. On the pristine surface, Figure 2-4a, new nuclei form sequentially and grow quickly (Figure 2-4c and d). In Figure 2-4b the presence of nanocrystals inhibits formation of new nuclei, and all nuclei grow slowly (Figure 2-4e). This result is unsurprising, based on crystal growth kinetics, where nuclei do not form closer than a distance that depends on the surface diffusion distance or the density of heterogeneous sites. Comparing the two experiments shows the importance of this competition between nuclei. At elevated temperatures, we suggest that the pattern of nucleation is also important, but now nucleation is taking place in the presence of greatly increased kinetics of attachment of the (readily available) Ag^0 to the nanocrystals. Certain nuclei or sites show rapid growth while nucleation and growth nearby appear suppressed. To explain the shapes of the nanocrystals under these conditions, we furthermore suggest that diffusion of Ag^0 over the nanocrystal surface is also faster, and the anisotropy of surface energies, diffusion and attachment enable these nanocrystals to adopt lower-energy faceted shapes rather than simply growing into large hemispheres. In this context, the diffusion rate of silver atoms on an Ag surface is known to increase by three orders of magnitude when the temperature is increased from room temperature to 70 ^oC.[95] (It is possible that the presence of defects such as twin boundaries or screw dislocations may drive the

anisotropic growth, but we do not see compelling evidence of such defects in the image contrast.) Thus, the formation of dendrites in our experiments is not due to diffusion limitations within the liquid; instead, it is an effect of limited growth sites and rapid kinetics for attachment and surface diffusion on these growing crystals.

Overall, we therefore attribute the growth mode change with temperature to a shift in the balance between growth and nucleation rates. The fact that deposition can result in two distinctly different morphologies is known from other crystal growth processes such as solidification of ingots.[79] Here, cooler regions show equiaxed grains. When nucleation takes place forming separate grains or paricles, their growth is limited by similar neighboring crystals nucleated at approximately identical times. The regions that solidify later show anisotropic, parallel columnar crystals referred to as dendrites; little other nucleation is observed, and the existing nuclei grow anisotropically to fill the volume available in the ingot. In the liquid cell experiment, Ag^0 formed in the beam irradiated region drives nucleation and growth, propagating a growth front from the periphery as in Figure 2-4a. At room temperature, nucleation results in an array of compact small crystallites that compete for the growth flux. No crystallite grows extremely quickly, and additional nuclei continue to form over an extended time period. At higher temperatures we expect a higher incorporation rate due to the enhanced kinetics. The earliest crystals to nucleate dominate the experiment and appear to inhibit formation of new nuclei nearby.

It is interesting to compare these results for the temperature-dependent growth of Ag with that of Au studied previously.[37] Common features of the growth include more faceted structures formed at higher temperatures, although nanorods with less extreme aspect ratios formed in the case of Au.[37] Although Au and Ag have many similarities, they are known to show differences in the morphology of their nanostructures. For example, silver nanowires with lengths of up to 20 μm

are relatively common where gold nanorods more than 500 nm in length are uncommon in the literature for reasons that are not fully understood.[96] It will be interesting to compare the temperature-dependent growth morphologies of Au and Ag with that of other materials to explore the common themes and differences in more detail.

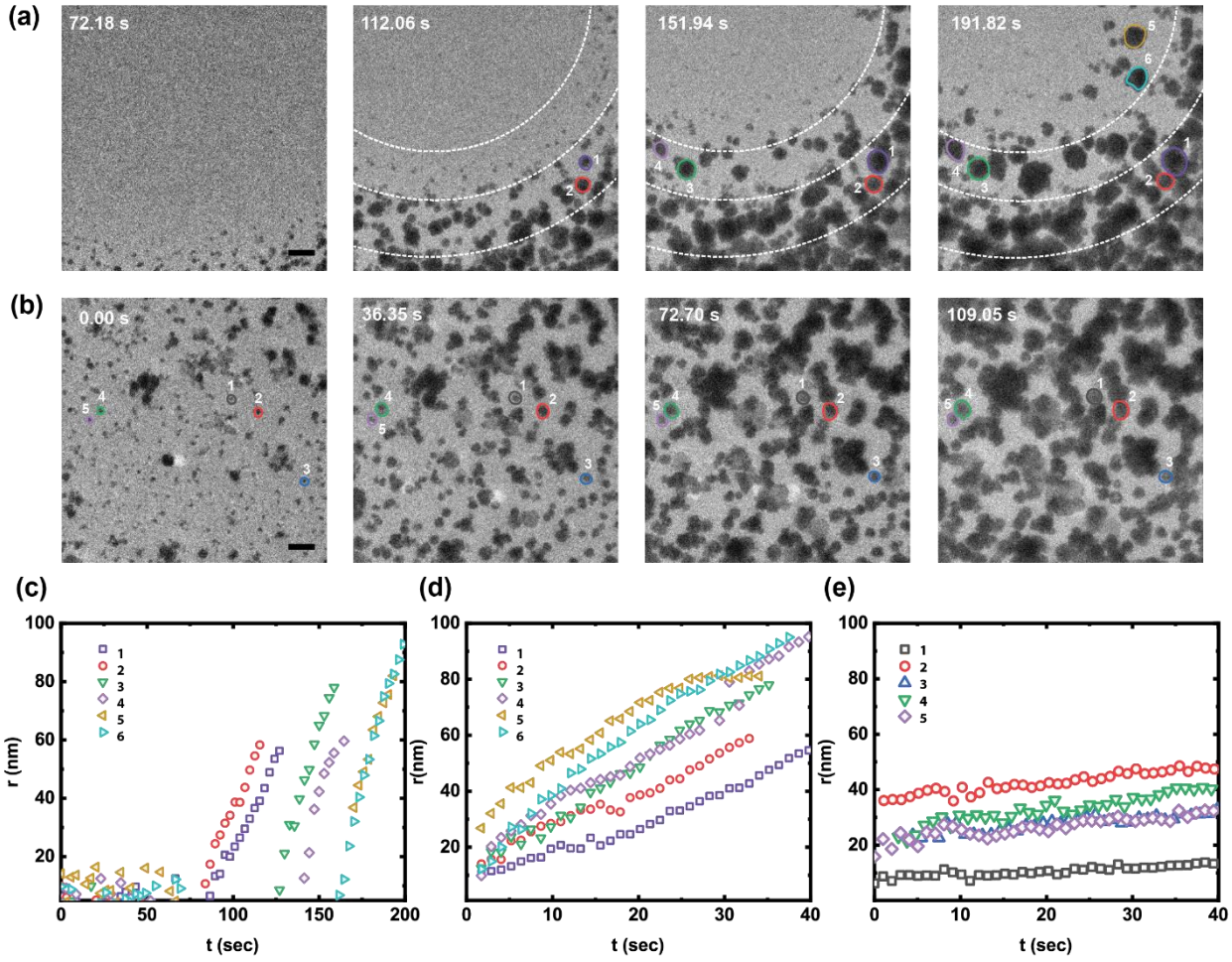

Figure 2-4. Ag particle growth at room temperature with different initial conditions. (a) Time series of *in situ* TEM images showing the growth of Ag nanocrystals during beam exposure at 25 ˚C on a previously unirradiated area. The beam is off-center showing progressive growth from the beam periphery. (b) A second growth experiment where small nuclei were pre-formed by a separate beam exposure. The solution was 0.01 M aqueous $AgNO_3$ and the dose rate was 2.8 ×

10^7 Gy/s. Scale bars are 200 nm. Dotted lines in (a) approximately indicate areas with different radial distances from the beam center. (c-e) Plot of radius versus time of individual particles indicated by the same color symbol in (a) and (b). Nanocrystals with minimum overlap throughout the video were selected for analysis. c Radius versus time for 6 individual particles in (a). (d) Radius versus time for the same particles after shifting the plots to align the onset time. (e) Radius versus time for 5 individual particles in (b).

Solution phase Ag growth in liquid cell TEM is temperature-dependent, showing compact isotropic nanocrystal growth at lower temperatures and growth of blade-like dendrites at higher temperatures. To explain the temperature effects, we considered multiple factors that could be relevant during crystal growth in liquid cell TEM. We modelled a temperature-dependent chemical environment in liquid cell TEM using temperature-dependent parameters and the full set of reactions involved in electron beam-induced radiolysis and redox reactions of $AgNO_3$. This kinetic model shows that the equilibrium concentration of Ag^0 and the ratio between Ag^0 and Ag^+ both increase with temperature. The model also shows that another important factor in liquid cell experimentation, the dose rate, may not monotonically affect the growth rate. The comparison between the depletion and diffusion lengths of ions suggests that ion supply and the changes in diffusivity are insufficient to account for the different growth modes at lower and higher temperatures. Instead, we explain rapid dendrite formation at higher temperatures by a dominant effect of faster surface attachment and diffusion processes taking place at relatively few nucleation sites, in contrast to the slower growth processes forming isotropic structures at multiple nucleation sites seen at lower temperatures.

2.3 Application: Palladium Nanocrystal Growth at Different Temperatures

We apply the temperature dependent radiolysis simulation to study the growth kinetics of other metal nanocrystal growth system. Engineering metal nanocrystals with tailored structures is necessary for developing applications[97] that use their catalytic,[98,99] electronic,[100,101] magnetic,[102,103]and plasmonic[104,105] performance. Solution phase synthesis is one of the best-known strategies for nanocrystal synthesis. This synthesis route involves chemically and physically complex processes that may include precursor reduction, nucleation, monomer attachment, growth, and surface termination due to organic ligands and stabilizers. Experimental parameters during synthesis control the nanocrystal growth kinetics; this in turn governs the resulting nanocrystal size, structure, and composition.[106] Therefore, understanding the effect of experimental parameters on the growth kinetics is an important challenge in the nanomaterials research community that offers opportunities for new pathways to synthesize nanocrystals with complex structures under precise control.[107]

Among metal nanocrystals, palladium (Pd) nanocrystals are especially vital catalysts for reactions such as hydrogenation[108] and hydrocarbon combustion.[109–111] They are known to show crystal facet-dependent catalytic activity.[112,113] Recent studies have therefore developed methods to synthesize nanocrystals with high index facets, including in hierarchically branched structures, aiming to increase the activity as catalysts.[114–116] Moreover, synthesis of Pd nanocrystals in aqueous solutions, avoiding organic solvents, is in high demand due to the improved controllability of the resulting nanocrystals that can be free from organic surfactants and ligands which can potentially decrease the catalytic activity and hinder further growth.[117–120] However, reliable protocols for synthesis of optimally shaped, aqueous-based Pd nanocrystals free of organic stabilizers are limited, due to the number of parameters that influence the nucleation and

growth process.[121] In particular, the synthesis of nanocrystals in aqueous solutions is often studied at room temperature,[122,123] whereas control of temperature in bulk-scale synthesis could offer new opportunities for structural and size control by allowing different pathways and morphologies to be accessed that are not dominant at room temperature.[124]

Here, we use liquid cell TEM and temperature dependent radiolysis simulation model to study the electron beam-induced growth of Pd nanocrystals under conditions in which heavily branched, high surface area morphologies are formed. We find that branched structures are formed over a range of temperature. Measurements of the size evolution of individual nanocrystals show growth kinetics consistent with surface reaction-limited growth at early times and supply-limited growth at later times. We compare the absolute growth rates at different temperatures, showing temperature dependence in the early regime but a lack of strong variation with temperature in the later regime. We discuss the diffusion, formation and surface reaction processes that can account for these findings. Based on this understanding of the rate-limiting steps, we discuss the fact that an irregular, branched nanocrystal morphology appears to form even in a regime that is controlled by the surface reaction rate. Since unstable growth morphologies are generally attributed to diffusion-limited growth process, this observation suggests additional opportunities to create high surface area, rough crystal morphologies that may optimize catalytic or other properties.

2.3.1 In situ TEM of Branched Palladium Nanocrystal Growth

We first show the process of Pd nanocrystal synthesis *in situ* in our liquid cell TEM experiments. Selected frames of bright-field videos of Pd nanocrystal growth without heating (i.e. at a temperature around 25 ˚C) and during heating to 50 ˚C are shown in Figures 2-5a and 2-5b. Heating

is achieved by flowing current through a resistive Pt strip embedded in the SiN_x viewing window of the chip and the temperature is calibrated through the Pt resistance.[26] The nanocrystals grow due to the reduction of metal ion precursors in the 0.1M H_2SO_4 + 0.5 mM $PdSO_4$ solution by radiolytically generated species. Growth therefore takes place within the volume irradiated by the TEM beam, a cylinder with a radius of 3 μm. For all experiments, observations were made near the edge of the window in regions where the liquid thickness was nominally 200nm. The visible nanocrystals have nucleated on the interior walls of the liquid cell enclosure. The typical value of electron flux is 13.6 $e^-/Å^2$ s and dose rate 5.6×10^7 Gy/s. To investigate the kinetics of the Pd nanocrystal growth at different temperatures, we first plot the radius r and r^3 of nanocrystals versus time (Figure 2-5 c-h). We define $t = 0$ sec as the time when we start the recording, immediately after the irradiation starts. Nanocrystals that enable individual tracking with minimum overlap with each other are denoted in Figure 1, and the corresponding size and volume are shown in Figures 2-5c, 2-5d, and Figures 2-5f, 2-5g, respectively. The most evident observation from the plots is that the nanocrystals display overall faster growth kinetics at 50 ˚C. Furthermore, the growth is faster up to a time (referred to as the transition time, t_c), after which the rate of size and volume growth slows at both temperatures. Determining t_c at the two temperatures will be discussed in detail below. When the volume of each nanocrystal is normalized by its maximum volume at t = 600 seconds (Figures 2-5e, 2-5h) the trajectories for individual nanocrystals are generally consistent, showing at both temperatures the initial rapid growth followed by slower growth. The spread in growth rates at each temperature becomes more apparent when specific Pd nanocrystals are tracked.

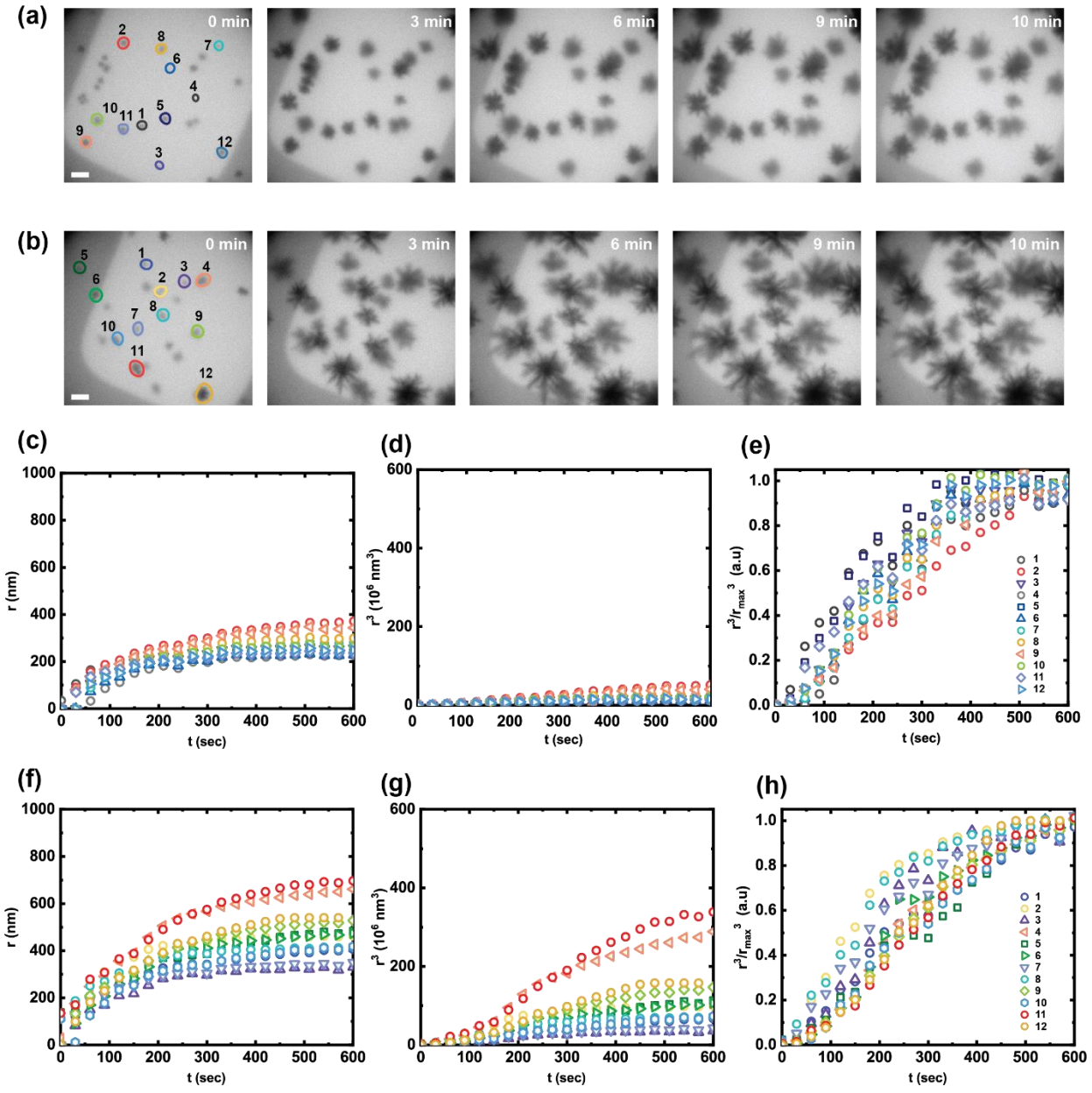

Figure 2-5. *In situ* observation and kinetic analyses of Pd nanocrystal growth at 25 ˚C and 50 ˚C. Image series showing the growth of Pd nanocrystals during beam exposure when (a) unheated, assumed to be 25 ˚C, (b) heated to 50 ˚C. The solution used is aqueous 0.1M H_2SO_4 + 0.5 mM $PdSO_4$ and the electron dose rate is 5.6 × 10^7 Gy/s. (c, d) Plots of r and r^3 versus t for the nanocrystals shown in Figure (a). $t = 0$ sec is the time the recording started. The beam was on the area for 1-2 seconds before this time, but some nuclei are already present. (e) Plot of r^3 / r_{max}^3

versus t for the nanocrystals shown in (a) where r_{max} is the maximum radius of each nanocrystal at t = 600 sec. (f, g) Plots of r and r^3 versus t for the nanocrystals shown in (b). (h) Plot of r^3 / r_{max}^3 versus t for the nanocrystals shown in Figure (b). The radius r of each nanocrystal is defined as the radius of a circle with an equivalent area. Images (a) and (b) are recorded in bright-field conditions. Scale bars are 500 nm.

A second observation from the videos is that nanocrystals develop branched or rough surfaces early in the growth process. This occurs at both temperatures, but the developing morphology is more apparent at 50 ˚C. Branching behavior is quantified using the circularity parameter $\lambda = 4\pi A/P^2$ with A = area and P = perimeter, a measure commonly applied to describe the characteristics of fractal structure. Structures with $\lambda < 1$ are generally characteristic of branched structures, and as the branching degree of a structure becomes stronger by the elongation of each branch or increase in the number of branches, the corresponding λ decreases. Figures 2-6a and 2-6b show that nanocrystals grown at both temperatures have $\lambda < 1$ from early times, indicating early formation of branched structures. Branch or roughness development in the nanocrystals will be discussed below in more detail.

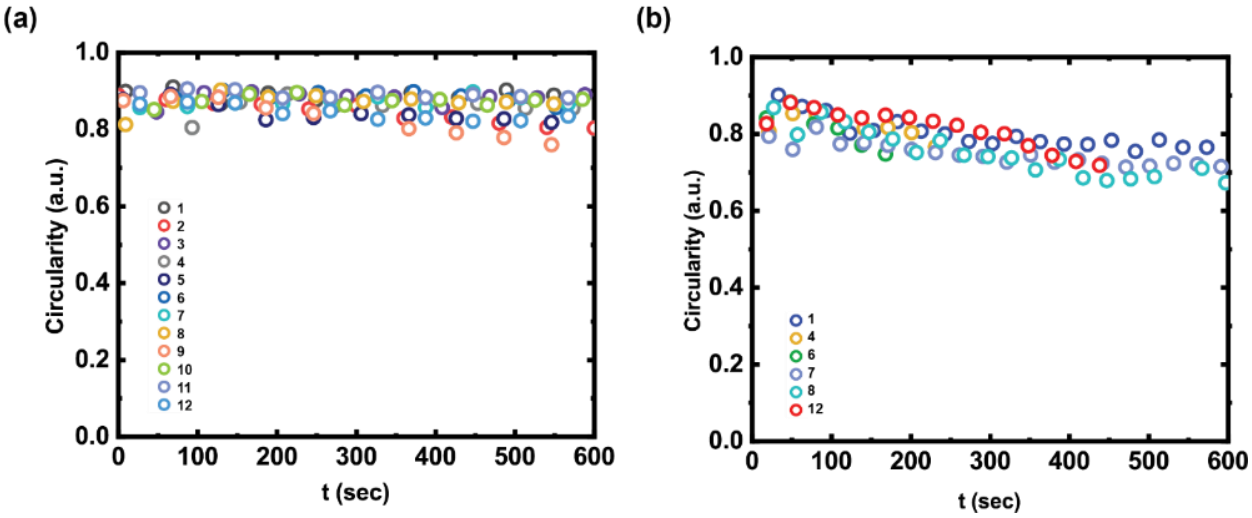

Figure 2-6. Circularity parameter (λ) of nanocrystals shown in Figures 2-5a and 2-5b**.** (a) Calculated circularity versus time of nanocrystals at 25 ˚C and (b) 50 ˚C.

2.3.2 Revealing the Growth Kinetics of Palladium Nanocrystal

The growth kinetics we observe for these branched Pd nanocrystals, involving beam-induced processes (and in the absence of a capping agent), may be controlled by several factors. Reaction-limiting steps may be the supply rate of Pd atoms to the growing nanocrystal or the rate of the surface reaction that results in incorporation of Pd atoms into the nanocrystal. Supply of Pd atoms requires multiple steps: diffusion of Pd ions to the region in which growth is taking place, reduction of Pd ion to form Pd atoms, which is mediated by radiolytically generated species and may occur in solution or at the nanocrystal surface, and diffusion to and incorporation of Pd atoms at the nanocrystal surface.[116] Surface diffusion of these atoms would then be expected to form facets and determine the nanocrystal morphology. The rate of Pd atom formation from Pd ions is sensitive to the concentration of hydrated electrons, which is calculated from a radiolysis model as discussed below. To infer the importance of each of these factors, we analyze the kinetics of Pd nanocrystal growth by testing whether the radius growth rate follows $r \sim \alpha t^{\beta}$, with α a prefactor and β the exponent. A value of $\beta = 1/3$ is expected for bulk diffusion-limited growth while 1/2 is expected for surface reaction-limited growth.[13] In Figures 2-7a and 2-7b we show radius-time log plots starting from the time at which nuclei are observed. At 25 ˚C and 50 ˚C, in the early time regime, the average exponents are 0.52 ± 0.14 and 0.50 ± 0.13, respectively, consistent with surface reaction-limited growth. Furthermore, the values of log a are 1.1 and 1.4 at the two temperatures, which corresponds to $\alpha = 12.6$ at 25 ˚C and $\alpha = 25.1$ at 50 ˚C. Comparing these coefficients indicates that the radial growth rate at 50 ˚C

is approximately 2 times larger than that at 25˚C. The transition times (t_c) after which the growth slows is t_c = 240 sec and 258 sec at the two temperatures, respectively. Considering the statistical spread in the parameters of the fitted plots, we assume that the difference in t_c is not significant. In the late time regime (after t_c), the exponents decrease to 0.11 ± 0.07 and 0.18 ± 0.09, respectively at 25 ˚C and 50 ˚C. However, the log α values are 2.1 and 2.2 respectively, showing similar growth rates in this later regime.

To interpret these fitting results, we develop a model for the growth process. Before the transition time, exponents that are close to 1/2 suggest surface reaction limited growth. Since the surface reaction is the process in which atoms attach and incorporate on the surface of the growing nanocrystal, the increase in the growth rate at the higher temperature can be explained by the increase in the surface reaction rate, which is indeed known to be proportional to exp(-E_A/RT), where E_A is the activation energy.[116] By comparing the growth rate at the two temperatures, we very roughly estimate that E_A for Pd atom incorporation is 2.2×10^4 J/mol, or 0.23 eV/atom. This estimated E_A may be roughly comparable to the binding energy between Pd atoms, and indeed an estimate of 0.57eV has been obtained for the dissociation energy when converting a Pd dimer to two adatoms.[125] Within this reaction-limited kinetic regime, we now consider the significance of the branched morphology. Circularity values lower than 1 from t = 0 sec at both temperatures indicate that the formation of the branched structure starts early in growth (Figure 2-7). It is well known [14] that branched structures can develop when the growth front becomes unstable under diffusion-limited growth. However, in our case, growth does not appear to be limited by diffusion at this time; instead, we suggest that this unexpectedly early branch formation can be attributed to the difference in reaction rates between facets, perhaps

leading to the development of branches with similar crystal planes. This finding demonstrates that structures with surface asperities can be formed not only as a result of diffusion-limited kinetics but also during reaction-limited kinetics.

We now address the growth kinetics in the late regime, after t_c. In this regime, the exponents have decreased to well below 0.5, suggesting that the process is limited by the supply of Pd atoms rather than by the surface reaction. We therefore consider the steps required for Pd atom supply, which are the diffusion of Pd ions and atoms and the formation of Pd atoms by Pd ion reduction. We first note that exponents lower than 1/3 have been explained in terms of diffusion-limited growth modified by phenomena such as overlap of the hemispherical depletion regions[126] which can give an exponent as low as 1/6, or hindrance of diffusion by liquid cell geometry,[13] giving an exponent of 1/8. Our data is consistent with either of these models or with some other modification of the diffusion process. If we now consider the expected effect of temperature, we first note that the diffusion coefficient (D) of Pd ions in water is about 2 times higher at 50 ˚C when calculated using the Stokes-Einstein equation, $\mathrm{D} = \frac{\mathrm{k_B T}}{6\pi\eta \mathrm{R}}$. Here k_B is Boltzmann's constant, R is the assumed radius of the ion, and the dynamic viscosity of water η is taken as 0.89 and 0.55 $\times 10^{-3}$ Pa·s at 25 ˚C and 50 ˚C, respectively. [89] Thus, we would expect faster diffusion by a factor of 2 at the top of our temperature range. (For simplicity, we assume that the Pd atom has a similar trend in its temperature-dependent diffusion coefficient.) However, the fitted coefficients a are similar, with similar growth rates at 25 ˚C and 50 ˚C in this regime. To explain this discrepancy, we suggest that the formation rate of Pd atoms also plays a role in the later regime. Since the reduction of Pd ions to Pd atoms is mediated by radiolytic hydrated electrons (e_h^-), we now discuss the effect we might expect temperature to have on the formation rate of Pd atoms, via a temperature-dependent radiolysis model.

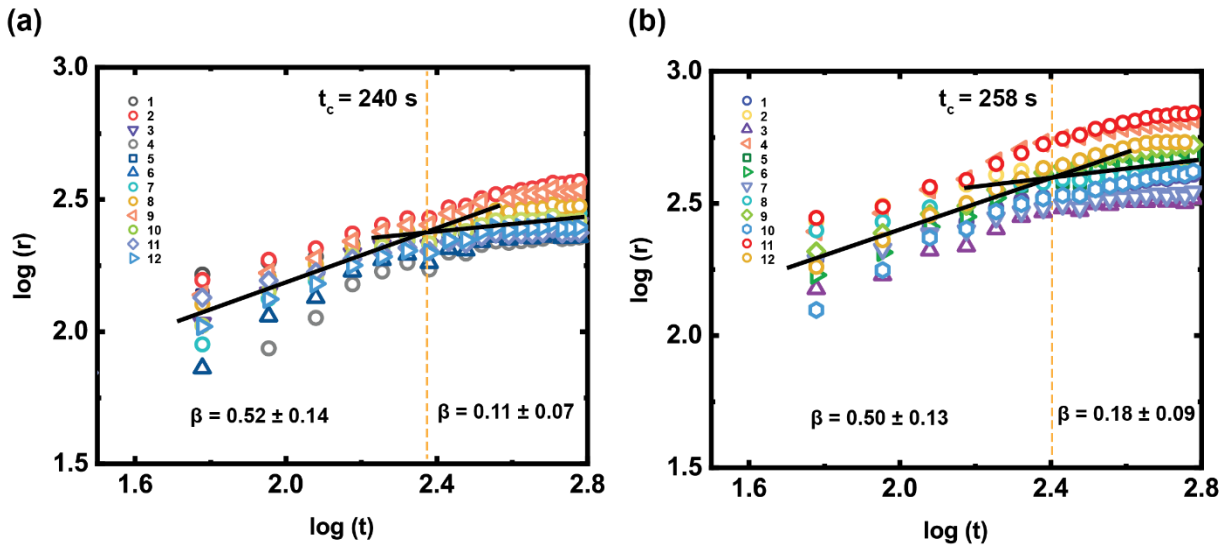

Figure 2-7. Kinetic analysis of Pd nanocrystal growth at 25 ˚C and 50 ˚C. (a) Log (*r*) versus log (*t*) plot of the nanocrystals at 25 ˚C from Figure 2-5a. (b) Log (*r*) versus log (*t*) plot of the nanocrystals at 50 ˚C from Figure 2-5b. The nucleation time for each individual nanocrystal is not included since all nucleated within 1-2 seconds. The β values shown were obtained by fitting each individual nanocrystal then averaging the fitted parameters. The black lines show fits with the average of the α and β values obtained in this way. The yellow dotted lines denote the transition time (t_c) at which these lines cross.

Figure 2-8 shows the results of a radiolysis simulation using the model developed in the previous section (2.2.2) We simplify the calculation by assuming pure water, using temperature-dependent reaction rates of pure water species. Thus, the calculations do not include the Pd species (Pd ion or Pd^{2+}, and reduced Pd atom or Pd^0) and the sulfate ion species, as their reaction parameters are not sufficiently well known.[81] Although these reactions are not included, the model provides a guide to interpreting the results of our Pd experiments at different temperatures. This is because

the step of converting Pd^{2+} ions into Pd^0 is mediated by reaction with the hydrated electron, e_h^-; increasing the e_h^- concentration will increase the Pd^0 concentration.

The results in Figure 2-8a show steady state concentrations C_{ss} of the species present in pure water: the main redox species e_h^-, H_2, O_2, OH•, and H• . These are shown at different temperatures for aerated solution at pH = 1 under the experimental dose rate of 5.6×10^7 Gy/s. When C_{ss} at different temperatures are divided by the C_{ss} at room temperature ($C_{ss}/C_{ss,\,R.T.}$), it becomes apparent that all values decrease by 10–40 % (Figure 2-8b). We can understand this as a higher rate of all reactions consuming these species, without a compensating change in the rate at which the high energy electrons create the species. In particular, the concentration of e_h^- decreases by about 40 % when the temperature increases from room temperature to 50 ˚C. The lifetime of e_h^- is short and they are localized within the beam cylinder; Pd ions diffuse in from the outside of the illuminated cylinder and react with e_h^- once inside. The C_{ss} values of e_h^- are calculated to be 6.8×10^{-9} and 4.5×10^{-9} M at 25 ˚C and 50 ˚C, respectively. For context, this corresponds to 2.3×10^9 and 1.5×10^9 hydrated electrons in the beam cylinder of radius 3 μm and thickness of 200 nm. These e_h^- rapidly react (e_h^- has a lifetime in the microsecond timescale[127]) to form Pd atoms within the beam. The lower concentration of e_h^- at higher temperature suggests that the Pd^0 formation rate will also be lower at this temperature. At higher temperature, a lower Pd^0 concentration coupled with the higher diffusion rates may provide an explanation for the similarity of growth rates at late times (Pd atom supply limited regime): lower Pd^0 concentration but faster diffusion. The compensation between the rates of Pd ion diffusion and Pd atom formation may result in an overall late-time growth rate that is similar at these two temperatures.

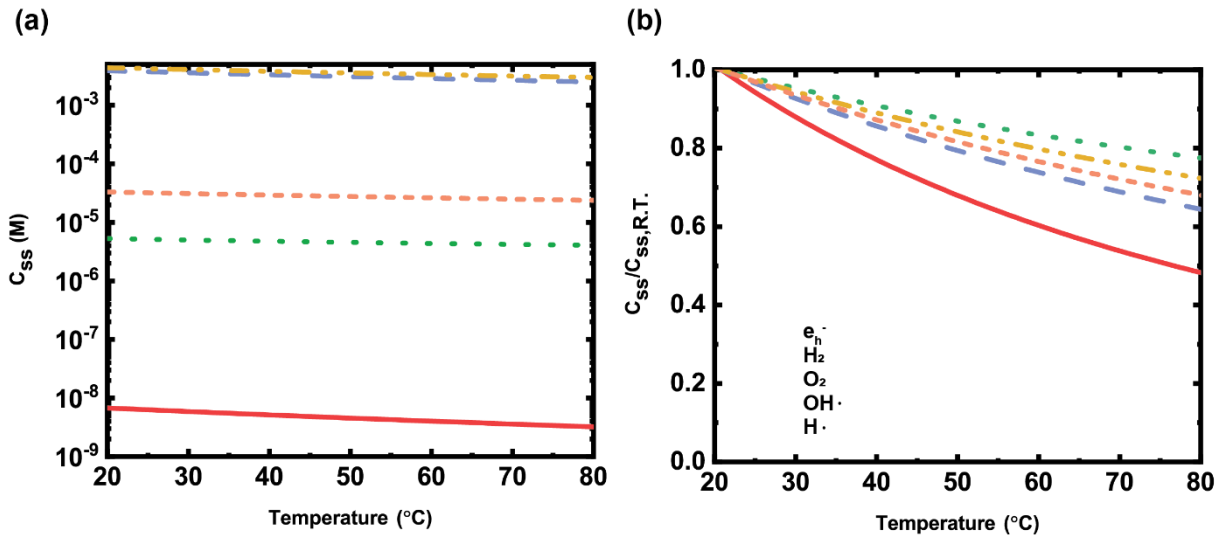

Figure 2-8. Results of temperature-dependent radiolysis simulation. (a) Steady-state concentrations (C_{ss}) of the main redox species e_h^-, H_2, O_2, OH•, and H•. (b) C_{ss} of the main redox species e_h^-, H_2, O_2, OH•, and H• at different temperatures divided by the C_{ss} at room temperature ($C_{ss}/C_{ss,\,R.T.}$). The conditions used in the simulation match the experimental conditions of aerated 0.1M H_2SO_4 + 0.5 mM $PdSO_4$ solution and dose rate 5.6×10^7 Gy/s.

Consistent with this model of initial surface reaction-limited kinetics followed by supply-limited kinetics are the results of a separate growth experiment, also at elevated temperature and with the same dose rate, but with different initial (nucleation) conditions. Figure 2-9 shows an image series of the growth at 50 ˚C of nuclei at a lower density, a result perhaps of a different surface condition or liquid thickness. Measuring values of t_c, α and β for this experiment, we find that the initial growth exponent is similar, the later exponent is slightly higher, and t_c is longer than those of the growths shown in Figure 2-5. The α values that reflect the growth rates are also similar to the growth rates of Figure 2-5 in both regimes. At early times, we would expect nanocrystal growth to follow surface reaction-limited growth, irrespective of their density, and

display β ~ 1/2. At later times, we might expect the interaction between diffusion fields to become important after more time has elapsed and the exponent to be closer to 1/3, due to reduced geometrical constraints from the larger distance between the nanocrystals. The growth process therefore is consistent with the sequence of limiting steps outlined above.

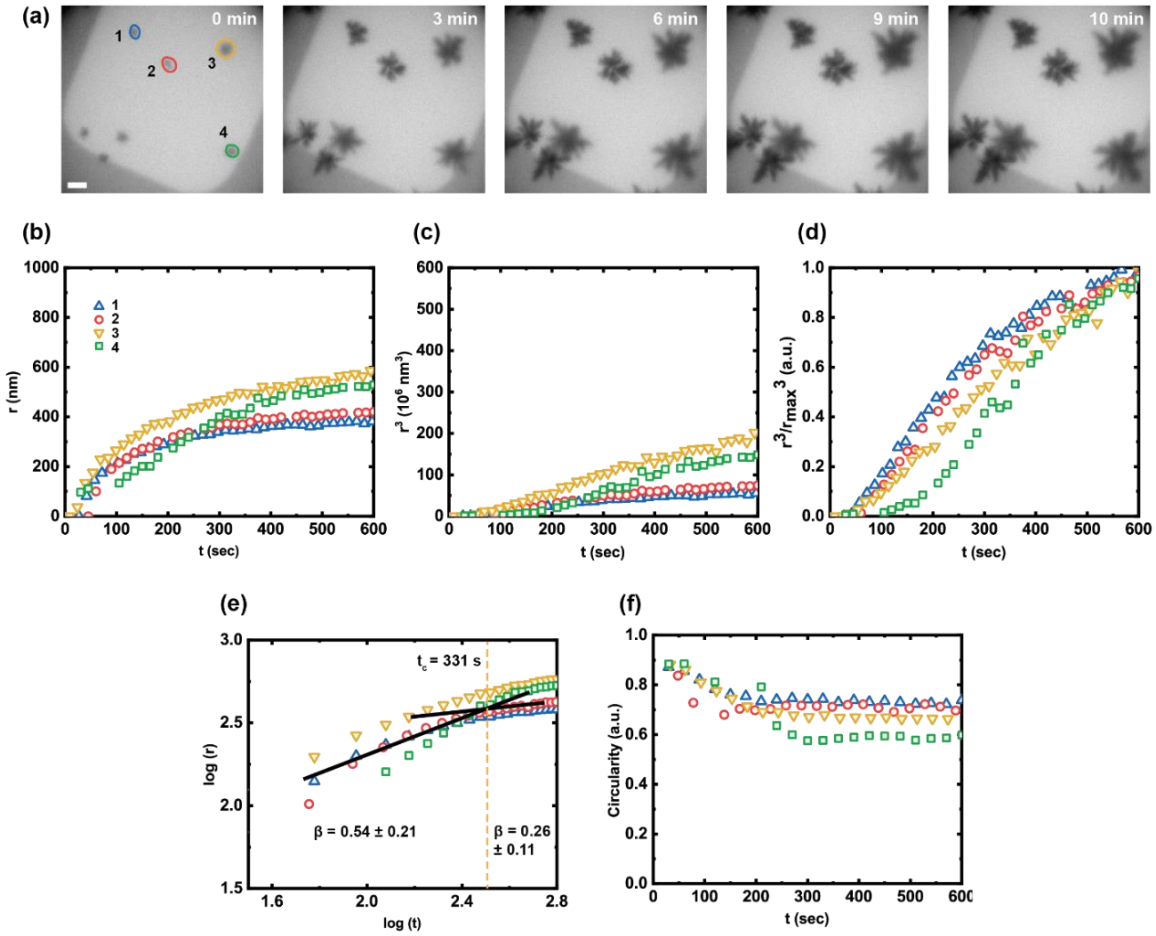

Figure 2-9. *In situ* observation and kinetic analyses of low density Pd nanocrystal growth at 50 ˚C. (a) Time series of TEM images showing the growth of Pd nanocrystals during beam exposure at 50 ˚C. (b, c) r and r^3 versus t plots of the nanocrystals shown in (a). (d) r^3 / r_{max}^3 versus t plot of the nanocrystals shown in (a) where r_{max} is its maximum radius at t = 600 sec. (e) Log (r) versus log (t) plot of the nanocrystals at 50 ˚C from (a). (f) Circularity versus t plot of the

nanocrystals at 50 ˚C from (a). The yellow dotted line denotes transition time (t_c). Intercepts of the plot, or log a are 1.2 and 2.0, respectively. Images (a) are recorded in bright-field condition. Scale bar is 500 nm.

We have interpreted measurements of the temperature-dependent growth of Pd nanocrystals through a combination of kinetic analysis and radiolysis modeling. Over the range of temperatures we have examined, the growth appears first limited by the surface reaction and later on transitions to kinetics consistent with a Pd atom supply-limited growth regime. During the earlier regime, the growth rate is faster at higher temperatures, consistent with a higher incorporation rate on the surface. During the later regime, the Pd atom supply, which is the combined process of Pd ion and atom diffusion and formation of Pd atoms, becomes the limiting factor for growth. We suggest that although the diffusion rate is expected to be higher at higher temperatures, the concentration of Pd ions is lower since our radiolysis calculations show a lower concentration of the hydrated electrons that mediate the formation of Pd atoms. We suggest that the temperature-dependent rates can compensate to result in overall similar growth rates. Unexpectedly, we find that an irregular branched morphology forms early during growth of the nanocrystals, in the regime that we believe is limited by the surface reaction. Although it is generally expected that branch formation in nanocrystals is driven by diffusion-limited growth, these results show that branches can also be formed during growth that is limited by the surface reaction rate. Instead of diffusion driven instability, it appears that a difference in growth rates on different facets may lead to branch formation. This finding is relevant to the production of large surface area nanocrystals to optimize catalytic activity. If the driving force to create such structures can arise from factors other than diffusion limited growth, this potentially broadens the range of growth conditions that may be useful in synthesis.

2.4 Conclusion

Combining a temperature-dependent radiolysis simulation that includes a complete reaction set with measurements of crystal growth morphology at different temperatures helps us to bridge part of the gap between liquid cell TEM experiments and real-world processes. It provides a template for future experiments exploring synthesis methods in other materials. It may even allow us to take advantage of certain benefits of liquid cell TEM, for example the ability to change temperature and chemical environment rapidly compared to larger-scale processes, to develop strategies that use temperature variations to achieve more precise control over nucleation, growth, etching or other processes. We suggest that initially this could be especially useful in systems where nanocrystal shape responds sensitively to well-controlled changes in the chemical environment in the liquid cell;[74] in the longer term we hope that these findings may contribute to a more realistic understanding of ex situ synthesis under temperature control.

To explore the range of applicability of the method developed in this study, it is useful to acknowledge the differences and similarities of nanocrystal formation in this work and in lab-scale synthesis. Nanocrystal growth in liquid cell TEM and lab-scale synthesis both involve the processes of metal precursor reduction to metal atoms, nanocrystal nucleation and growth. The most critical difference is the source of reducing agent. Lab-scale nanocrystal synthesis commonly introduces chemical reducing agents, whereas the reducing agents in liquid cell TEM experiments are reactive radicals created by radiolysis.[128] However, radiation-induced nanoparticle synthesis is a recognized strategy with certain benefits and is even more similar to liquid cell TEM conditions.[129] A critical difference between radiolytic and chemical reducing species is that the thermodynamic and kinetic driving forces of radiolytic agents are generally stronger than commonly used chemical reagents but their concentrations are typically orders of

magnitude smaller than reagent concentrations used for synthesis. It has been suggested[59] that concentration and reducing power can compensate such that appropriate selection of conditions can create liquid cell TEM experiments that guide strategies for synthesis outside the TEM. In lab-scale synthesis the conditions chosen (concentration, temperature) determine the final yield and morphology. In this work, we varied temperature while using the same precursor concentration, assuming that the local metal precursor concentration reaches equilibrium within the irradiated region. This is comparable with lab-scale synthesis that utilizes well-stirred reactors to distribute species homogeneously and avoid buildup of concentration gradients. Since the simulation model incorporates concentration, dose rate, and temperature, future studies can use this type of model with experimental results to gain insights relevant to lab-scale synthesis. An interesting extension would be to separate the effects of dose and dose rate in radiolytic synthesis by varying the beam intensity and image exposure time.

Overall, these results showcase how liquid cell TEM combined with a detailed, temperature-dependent radiolysis model can help develop an understanding of temperature dependent beam-induced nanocrystal growth. The factors of nanocrystal growth addressed in this study, including temperature- and dose-dependent chemical environment, diffusivity, and surface processes, should be quantified if we wish to tune the solution phase growth kinetics and morphology evolution of nanocrystals. This is not a simple task in general, but we hope that the results of this study and particularly the temperature-dependent radiolysis model could contribute to properly designing and understanding the results of liquid cell TEM experiments and connect to the formation of nanocrystals outside the TEM under thermal control.

Chapter 3. Nanoscale Electrochemistry under a Controlled Environment

Electrochemical liquid cell transmission electron microscopy (TEM) enables imaging of nanomaterials in a liquid phase, coupled with simultaneous measurements of electrochemical signals during cycling. For many electrochemical processes, liquid cell TEM has provided unique insights into reaction mechanisms [130–134] for fundamental electrochemical reactions such as deposition, etching, and corrosion, as well as the dynamics of materials applied for electrochemical energy storage technologies, including batteries and electrocatalysts. In this chapter, we describe the electrochemical parameters in liquid cell TEM, namely, temperature and the substrate, that strongly affect the chemical and physical environment of the system, and therefore leading to the control of the kinetics of the electrochemical phenomena including deposition, coarsening, and etching.

3.1 Thermally Controlled Electrochemical Deposition

The effects of temperature on electrochemical processes are important in systems that must operate over a range of conditions, including batteries for transport and storage.[135,136] The elevated temperature also enables electrocatalytic[137–139], galvanic[71] and corrosion[70] processes that occur slowly or not at all at room temperature. More generally, the use of temperature as a variable parameter in electrochemical reactions provides benefits in controlling reaction pathways[140–142] and measuring kinetic parameters.[143–147] Mechanistic studies of electrochemical processes as a function of temperature can therefore yield information useful for both applications and fundamental understanding. Previous literature has used ex-situ TEM[148] or *in*

situ optical microscopy[149] to study the effect of temperature on nucleation and growth of electrochemically formed nanocrystals, and liquid cell TEM experiments to date have examined an electrochemical etching process at elevated temperature. [16]

3.1.1 Electrochemical Liquid Cell TEM with Temperature Control

We implement temperature control in liquid cell TEM during electrochemical deposition to image copper deposition from an acidic electrolyte. Electrochemical deposition of copper is a critical process used in fabricating interconnect structures in microelectronics and has been examined in detail in liquid cell TEM at room temperature.[90,126,150] When adapting these measurements to elevated temperatures, it is critical to consider parameters added to the experiment, in particular, the exact temperature distribution in the liquid cell, diffusion through the liquid and the effect of the electron beam on the process. In this chapter, we find that deposition can be carried out at controlled temperatures and that as the temperature rises, the process takes place at an increased rate, as expected. We calculate the temperature distribution in the cell, showing that the temperature increase is localized, leading to the hot spot formation. Finally, we discuss the transition of growth mode from reaction-limited to diffusion-limited based on the temporal evolution of the Cu ion concentration profile. We expect that this study would be the useful guidance for temperature-dependent electrochemistry experiments in liquid cell TEM and connecting the results to the understanding of kinetic parameters in bulk electrochemical phenomena.

3.1.2 Temperature-Dependent Electrochemical Copper Deposition

We first show the electrochemical deposition of Cu on electrodes at different temperatures. We use the experimental configuration shown in Figure 3-1a that enables simultaneous heating and electrochemical control in liquid cell TEM recently demonstrated by our group, S[16] The chip has a Pt heating strip with an array of viewing windows(Figure 3-1b) embedded in one of the SiN_x windows, and it controls the temperature by Joule heating. We added 50 nm thick Pt electrodes for electrochemical biasing using electron beam deposition. These electrodes are placed on top of the SiNx window, and it is electrically isolated from the heating strip. Using this configuration, temperature and electrochemical biasing can be separately controlled at the same time. To carry out electrochemical deposition of copper, the liquid cell was filled before each set of experiments with an electrolyte consisting of aqueous 0.1M $CuSO_4$ + 0.18M H_2SO_4 solution, a conventional electrolyte used for copper deposition. Electrochemical deposition of Cu is carried out in the liquid cell chip with two-electrodes for electrochemical biasing under current controlled conditions, pulses of 5 mA for 5 s followed by 0 mA for 5 s, with this cycle repeated up to 20 times. Repeated pulsing is used to give the comparison of on and off currents.

We compare the electrochemical deposition of Cu at three different temperatures using a liquid heating system with the capability to control the thermal environment by Joule heating. Figure 1c shows the electrochemical deposition under the given pulsing condition at each temperature of room temperature (blue), 35 °C(green), and 45 °C(red). The lower intensity of the image indicates the thicker deposition of Cu, and it is apparent from the image that the intensity drops most rapidly at 45 °C, suggesting the fastest deposition at higher temperatures. Intensity change during the electrochemical pulsing is tracked and plotted in Figure 3-1c with

corresponding voltage and current response. The region indicated with a dotted rectangle in Figure 3-1b is used to measure and average the intensity. The topmost panel of Figure 3-1d displays the time versus intensity of the indicated region, where the drop in the plot indicates the decrease in intensity and, therefore increase in the thickness of the deposited Cu. Note that the electrochemical response for each experiment is similar, where the intensity drops 'step-wise' as the current is applied in repeated pulses, showing that the temperature change leads to a deposition rate change but the electrode behave the same as when unheated. The amount of deposited Cu increases and the intensity drops during current application, followed by plateau of intensity during the flow of resting current.

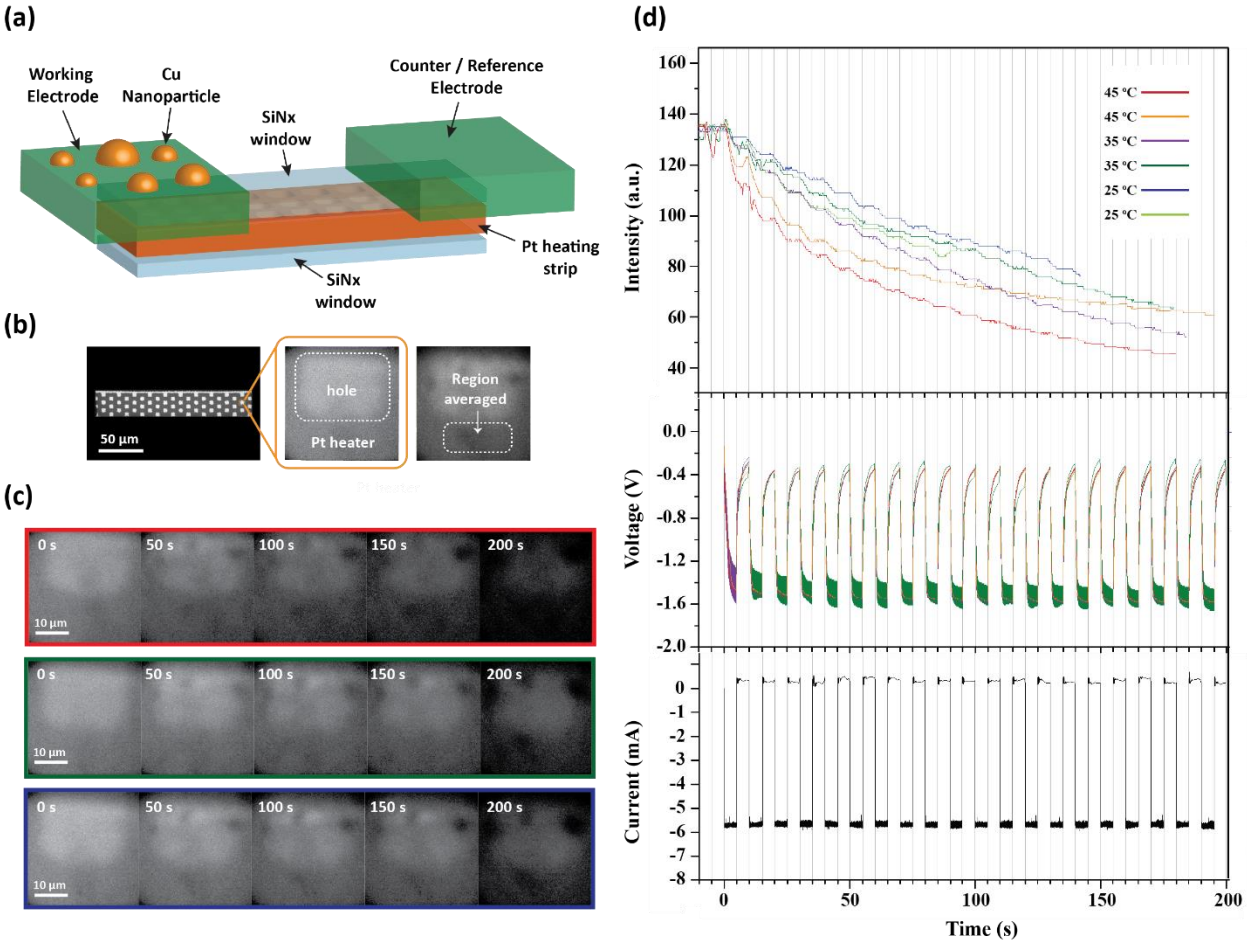

Figure 3-1. Electrochemical Cu deposition under temperature control in liquid cell TEM. (a) Schematic drawing showing the experimental setup where electrochemical biasing electrodes(green) are placed on top of the electron transparent SiN_x window (light blue), which has Pt heating strip in between (red). (b) Low magnification TEM image of Pt heating strip with an array of viewing holes to allow electrons to pass. (c) Time series of *in situ* TEM images showing the Cu deposition at 45 ˚C (red), 35 ˚C (green), and 25 ˚C (blue). (d) Intensity, voltage, and current measured during Cu deposition at different temperatures. The region below the hole indicated by dotted rectangle in (b) is where intensity was measured and averaged.

Figure 3-2 shows that at all temperatures, the intensity drop per each pulse (ΔI) decreases with the number of pulses, and therefore the difference between ΔI per each temperature is most apparent at early pulses. When ΔI values are compared between temperatures, the intensity drop per each pulse(ΔI) is larger at higher temperatures, as expected from the images. ΔI for higher temperatures decreases rapidly as the pulse continues, and the final slops at each temperature converge to a similar value. Figure 3-2a and Supplementary Table S2 show that at the early pulses, ΔI at 45 °C is 2 to 4 times larger than at room temperature or 35 °C. After the first 3 pulses, ΔI rapidly decreases, and ΔI at the given three temperatures are similar throughout the rest of the pulses. This indicates that temperature-dependent kinetics is most apparent during the early stages of the deposition. We then calculate the number of pulses required to deposit the same amount of Cu at different temperatures (Figure 3-2b). We first convert the intensity to the thickness of Cu in the image, using the intensity at the regions with known amounts of materials as a reference. From the images shown above in the figure, the windows and the heater strip differ by the heater thickness of 30nm of Pt. After the intensity calibration, we find the number of

pulses required at each temperature to reach the intensity of the reference (30nm Pt), which corresponds to 120 nm thick Cu. Although the growth rate of Cu deposition decreases at higher temperatures as the pulse continues, due to the large rate difference at the earlier stages, the numbers required for the deposition of 120 nm thick Cu is around 3 pulses for 45 °C, and 6 pulses for lower temperatures. Therefore, we estimate that 40 nm and 20 nm thick Cu are deposited per pulse at 45 °C, and 25 °C in the first pulses, respectively.

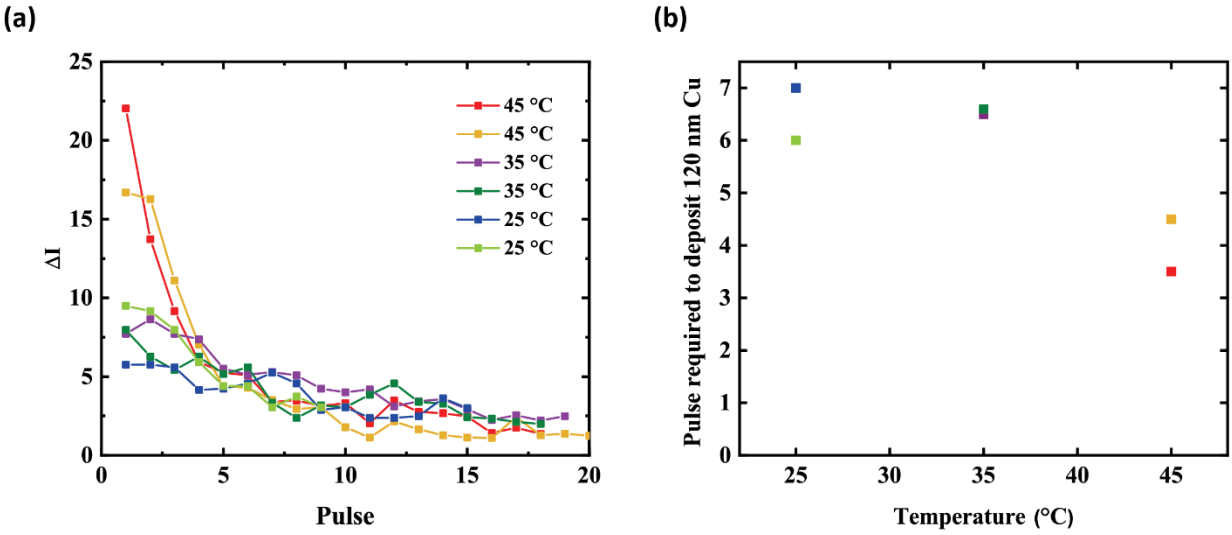

Figure 3-2. Estimation of Cu deposition from the averaged intensity of images series**.** (a) Intensity drops per each pulse(ΔI) versus pulse at each temperature and (b) number of pulses required to deposit 120 nm thick Cu.

To quantify the measurements from Figure 3-2 and address the temperature effect on the electrochemical deposition of Cu in the liquid cell, we calculate the temperature distribution in the liquid cell with a heating element. We adapt finite element analysis on the simplified model geometry of the system used in this study (Figure 3-3a, b). A simplified geometry of the liquid

cell with Si chip, liquid electrolyte layer, Pt electrode for electrochemistry, electron transparent SiNx window, and Pt heating strip was constructed for calculation. In the calculation, the heating sources is the Pt heating strip set at 45 °C. To clearly visualize the temperature distribution near the working electrode for electrochemistry, Si chip and liquid electrolyte layer are not included in the figure. The detailed boundary condition of the analysis is described in the Method. As seen from Figure 1a, the region of elevated temperature with an area of 30 × 30 μm^2 is localized near where the heater lies under since the thick Si substrate of the chip around the window acts as an efficient heat sink. Temperature distribution plot across the working electrode also shows that the Pt working electrode is locally heated by the Pt heating electrode underneath it, through a 30 nm thick SiN_x layer in between (Figure 3-3b). One important thing to note is that the temperature of the Pt working electrode reaches that of the heating strip (45 °C), which indicates that the deposition temperature of Cu on the working electrode can be directly adapted from the heater temperature. Figure 3-3b also shows that the temperature drops from 45 °C to room temperature across the heated Pt working electrode is confined within less than 10 μm. Therefore, the calculated temperature gradient around the thin boundary near the heater region indicates the confined heating effect.

After confirming the localization of the hot spot on the electrode, we then calculate the 'effective area' of electrochemical deposition. Under the assumption that every Cu deposition is taking place at the hot spot of the electrode with an area of 30 × 30 μm^2 when a 5 mA pulse is applied, the thickness of Cu grows 1000 μm per pulse. This number is inconsistent with our experimental observation from Figure 3-2b, which showed that Cu grows 20 nm and 40 nm per pulse at room temperature and 45 °C. Using the experimentally calculated growth rate of deposited Cu, the

current density per pulse is calculated as 110 A/m^2 and 220 A/m^2 at room temperature and 45 °C, respectively.

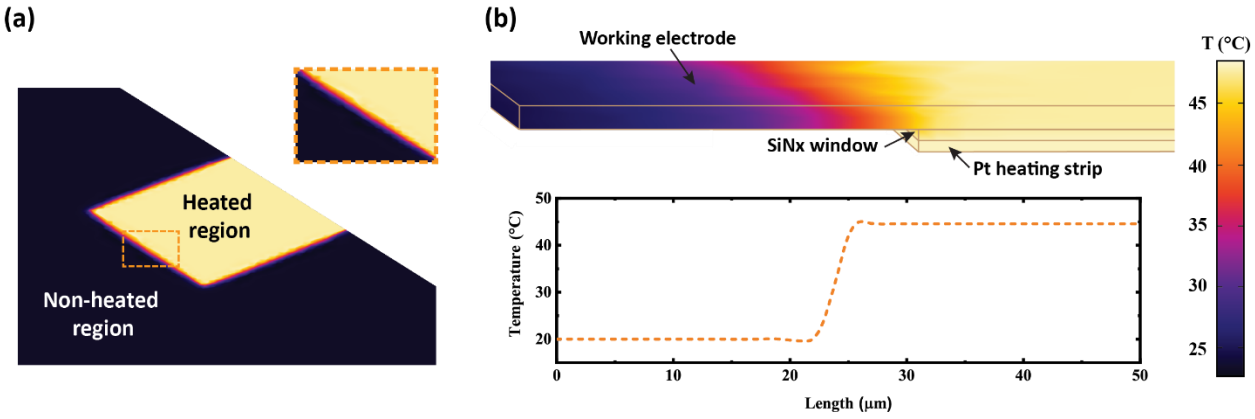

Figure 3-3. Finite element calculation of the temperature distribution in the liquid cell. (a) Top view of the temperature distribution where the bright yellow square denotes the locally heated region of the biasing electrode from the heater below. The inset image shows the narrow range of temperature gradient between the non-heated and heated region. The size of the heated region is set as 30 × 30 μm^2. (b) Temperature distribution of the cross section of and corresponding plot across the dash line. The operating temperature of the heater is set at 45 °C.

We then address the temperature-dependent growth kinetics of electrochemically deposited Cu using the experimentally determined current density at different temperatures. The kinetics of deposition is relevant to the current density distribution, which is known to be having three main contributions.[151] The primary current distribution is originated from the resistance to the current flow dictated by the conductivity of the electrolyte. The difference in specific conductivity of 0.1 M $CuSO_4$ acidic solution at 25 and 45 °C is 0.05 S/cm.[152] In this regard, we focus on the role of temperature on the second and the third contributions, while each of the contributions is relevant

to the reaction-limited or diffusion-limited growth of the Cu ion nanocrystals on the electrode. The effect of temperature on the transition of the Cu deposition kinetics from the reaction-limited growth to the diffusion-limited growth captured in this study will be further explained while considering those two contributions to the current density distribution.

The second contribution is due to the presence of electrochemical faradaic reactions at electrodes. In the system we analyze, the Faradaic reaction is the electrochemical growth of the nanocrystals by the reduction of the ions, which is relevant to the reaction-limited growth of the nanocrystals. Finally, the third contribution is inherited from the mass transfer phenomena that determines the concentration gradient potentially affecting the capacity for the faradaic reaction to be sustained. In the liquid cell, mass transfer is mainly dictated by the diffusion of Cu in the bulk electrolyte to the region near the electrode driven by the concentration gradient formed after the application of potential pulses. Therefore, the third contribution is connected to the diffusion-limited growth regime of process.

It is shown from the intensity measurements above (Figure 3-2) that at all temperatures, the growth rate decreases with later pulses, suggesting that diffusion becomes the limiting factor of the electrochemical deposition. This is not surprising as the Cu deposition on already existing Cu crystal has zero overpotential required, which means that there is a low thermodynamic barrier for the electrochemical reduction reaction. Therefore, under the conditions we used in the experiments, the growth rate is reaction-limited initially and later becomes diffusion-limited. When the growth rate is reaction-limited during the early pulses, the rate depends on the temperature, which could be explained using the exponential dependence on temperature of current density calculated by the Butler-Volmer equation. After a few pulses, growth rates

substantially decrease since the Cu ions are exhausted from the reduction reaction consuming the ions, which will be discussed in detail with the calculation shown in Figure 3-4 below. Note that the reduction potential E of Cu ion defined from the Nernst equation is temperature dependent. The Nernst Equation is given as follows,

$$E = E° - \frac{RT}{nF} lnQ \qquad \text{(Eq. 3)}$$

where E is the total potential difference, $E°$ is the standard cell potential, R is the gas constant, T is the temperature, n is the number of electrons transferred in the reaction, F is the Faraday constant, and Q is the reaction quotient. The temperature coefficient of reduction potential $\frac{dE}{dT} = \frac{RlnQ}{nF}$ is calculated as 0.1 mV/ K when the concentration of Cu^{2+} ion is 0.1 M and $n = 2$. This is similar to $\frac{dE}{dT}$ values of common electrochemical reactions.[153] Standard reduction potential E˚ is also linearly dependent on the temperature while the temperature coefficient $\frac{dE°}{dT}$ is 0.011 mV/K between 0 ˚C and 100 ˚C.[154] Therefore, the total difference of E at 25 ˚C and 45 ˚C is $20K \times (0.1 + 0.011)\frac{mV}{K} = 2.22\,mV = 0.00222\,V$.

However, we suggest that the difference in E would need additional parameters to cause two times of growth rate difference, sine the total difference of E at 25 ˚C and 45 ˚C is less than 0.003 V.

To determine the transition point of growth mode from reaction-limited growth to diffusion-limited growth at different temperatures, we calculate the temporal evolution of the Cu ion concentration profile during the pulsing based on the experimentally determined current density calculation above. In the calculation, we consider the diffusion of ions through the bulk electrolyte as the major diffusion process. Note that the diffusion coefficient of ions (D_{bulk}) scales

exponentially with temperature following the Arrhenius behavior with an activation energy of 19.6kJ / mol for the case of Cu ion.[155,156]

Figure 3-4a shows how Cu ion concentration evolves at room temperature during 5 seconds of the first pulse-on stage, where the concentration near the electrode decreases from 0.1 M to 0.05 M. In contrast, Cu ion concentration reaches 0 M near the electrode at 45 °C at the end of the first pulse-on stage (Figure 3-4b). During the pulse-off stage, Cu ion concentration is recovered up to 0.08 M at room temperature (Figure 3-4c), and 0.06 M at 45 °C (Figure 3-4d). We then tracked the wall concentration, the concentration at the electrode, over several pulses at room temperature (Figure 3-4e) and at 45 °C (Figure 3-4f). At both temperatures, during the pulse-off stage, the wall concentrations recover to over 0 M within three pulse applications. However, the wall concentration reaches 0 M and does not recover after three pulses at 45 °C. The comparison of wall concentration recovery again supports the faster transition from reaction- limited to diffusion-limited at higher temperatures. This also agrees with the observation in Figure 3-2a which displayed the rapid drop in growth rate after 3 pulses at 45 °C.

Combined with the previous discussion on the temperature distribution in the liquid cell and the temperature effect on the Cu nanocrystal growth process, we can deduce the evolution of temperature-dependent growth process. During the initial pulsed deposition, increased temperature enhances the reaction-limited growth kinetics. Faster reaction kinetics is reflected by the higher measured deposition rate and calculated current densities at 45 ˚C that are two times larger than at 25 ˚C. Increased reaction rate (reduction of ions) in the earlier stage at the high temperature leads to the faster transition to the stage with non-recoverable wall concentration of 0 M, which is the diffusion limited growth stage. In the late regime, the growth rate is no longer dependent on temperature. This is because we are only heating localized small region of the

liquid, and the diffusion in the non-heated region remains the level of room temperature diffusion.

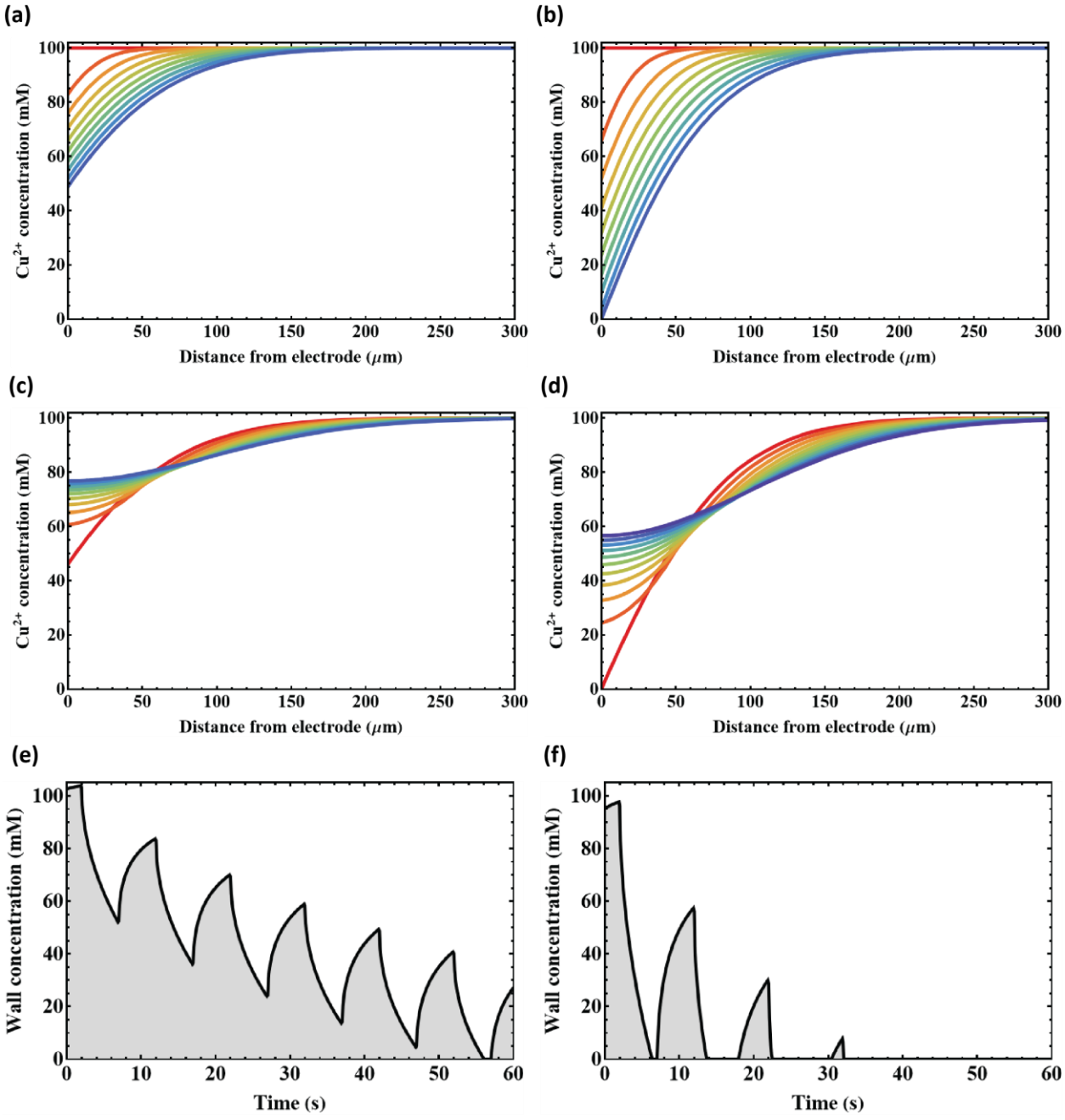

Figure 3-4. Calculated Cu ion concentration in liquid cell at different temperatures. (a, b) Cu ion concentration profile during pulse-on stage for 5 seconds at room temperature(a) and 45 °C(b). Experimentally determined current densities at each temperature are 110 A/m^2 and 220 A/m^2

respectively. The concentration recovers during the pulse-off stage of 5 seconds at room temperature (c) and 45 °C (d). The plots depict the evolution of a system over a time interval of five seconds, with each plot corresponding to a time step of 0.5 seconds. The color scheme of the plots transitions from red at the first time step to blue at the final time step. (e, f) Time evolution of wall concentration of Cu ion showing the decrease in recovered concentration at room temperature (e) and 45 °C (f).

In this chapter, we study the temperature effect on the electrochemical deposition of Cu in liquid cell TEM by measuring the intensity and corresponding voltage and current coupled with the calculation of temperature distribution and ion concentration gradient. Averaged intensity indicating the thickness of the deposited Cu in liquid cell TEM decreases step-wise following the repeated application of pulsed current at all three different temperatures. The intensity drop per pulse shows the highest at 45 ˚C during the pulses in the earlier stage due to the faster reaction kinetics. After a couple pulses, the growth mode is controlled by diffusion, which is also reflected in the calculation of ion concentration, showing that the wall concentration is reaching 0 M earlier at higher temperatures. Therefore, slow pulsing or slow growth is necessary to realize the benefits of heating. Moreover, although it hasn't been shown directly in this study, temperature should also affect the morphology of the grown Cu particles as the process affecting the morphology is controlled by the temperature. Finally, it is shown in this study that the local heating can control the deposition on the electrode in liquid cell TEM. Patterning deposition at nanoscale over a large electrode could have a useful application in electrochemically manufacturing nanostructures. We therefore expect that the approach in our study would be a

useful platform to study the localized electrochemical patterning using spatially controlled heating while understanding the kinetics of the electrochemical growth.

3.2 Electrochemical Nanostructure Deposition on 2D Materials

Heterostructures that combine metal nanoparticles and two-dimensional (2D) materials fabricated by electrochemical deposition offer the opportunity to enhance performance and develop unique material properties for technological applications ranging from catalysis[98,157] to nanoelectronic devices.[158] Continued improvements in the precision and application of electrochemical fabrication requires a deep understanding of the interplay of kinetic and thermodynamic phenomena that operate during the process. In this chapter, we explore the deposition of copper (Cu) metal on a graphene electrode using liquid cell transmission electron microscopy (TEM), using the temporal and spatial resolution of this technique to explore the nucleation and growth of nanocrystals. The technique reveals an unexpected transient phenomenon under certain applied voltage conditions, and we discuss possible mechanisms.

3.2.1 Electrochemical Deposition of Metal Nanoparticles on 2D Materials

We fabricated the 2D material electrode liquid cell chip by transferring exfoliated graphene on the Pt electrode of the standard chip (Figure 3-5a) based on the protocol.[17] The graphene is used as a working electrode onto liquid cell chips patterned with multiple platinum (Pt) electrodes, and Pt was used as reference and counter electrodes. We then performed electrochemical deposition of Cu on graphene by controlling the deposition potential in an 0.1 M $CuSO_4$ + 0.1 M H_2SO_4 electrolyte solution.

We first investigate the effect of applied potential on the size and density of electrochemically deposited copper islands. We first apply a potential of -40 mV in 10 s pulses ('*V on*' state) to the Pt/graphene electrode system and repeat the cycle for -60 mV, -80 mV and -100 mV as shown in the first row of Figure 3-5b. Then the applied potential is negatively increased to -180 mV, -200 mV, -240 mV, and -260 mV for 10 s pulses as shown in the second row of Figure 3-5b. The average radius of the electrochemically generated cluster (Figure 3-5c) at different potentials show that the higher driving potential gives smaller nuclei as expected from the standard model. [90] We also measure the Cu island density (N_0) and the maximum radius of the isolated hemispherical diffusion zones of the islands (R_{diff}), where R_{diff} is approximately $N_0^{-1/2}/2$. [90] The island densities measured at different applied potentials in Figure 3-5d are in the range of 10^9 cm^{-2}, and the numbers increase as the applied potential increases, which is similar to the Cu island growth on Au electrode reported previously.[126] R_{diff} decreases accordingly as the island density and applied potential increases. Island densities in the scale of 10^9 cm^{-2} are 3 orders of magnitude larger than calculated by using the Sharifker-Hills model, and this discrepancy was previously explained based on adatom adsorption.[90] Adatom adsorptions take place on the substrate, resulting in the formation of additional islands, and therefore increasing the island density above the expected values. Another important feature to note is that when the applied potential is relatively low (-40 mV, -60 mV, -80 mV, and -100 mV), electrochemically deposited islands immediately dissolve as the potential is turned off. On the other hand, at higher applied potentials, islands persist even after the potential is turned off, followed by additional deposition and coarsening. The comparison of cyclic voltammetry curves among different configurations of graphene electrodes, where 1, 2 or all 3 of the Pt electrodes are covered with separate graphene flakes, suggests that there is an intrinsic potential ($<\pm 60$ mV) between the graphene and Pt

electrodes. [17] We conclude that this built-in potential is high enough to dissolve the deposited Cu even when the applied potential is 0 mV. This would be in effect when the potential applied for growth is small (-40 mV, -60 mV, -80 mV, and -100 mV) and the nanocrystals dissolve immediately after the applied potential is turned off, as well as when the applied potential is large (-180 mV, -220 mV, -240 mV and -260 mV), when continued growth takes place, but nanocrystals eventually dissolve, requiring up to 2 minutes, which will be discussed in detail in the following section.

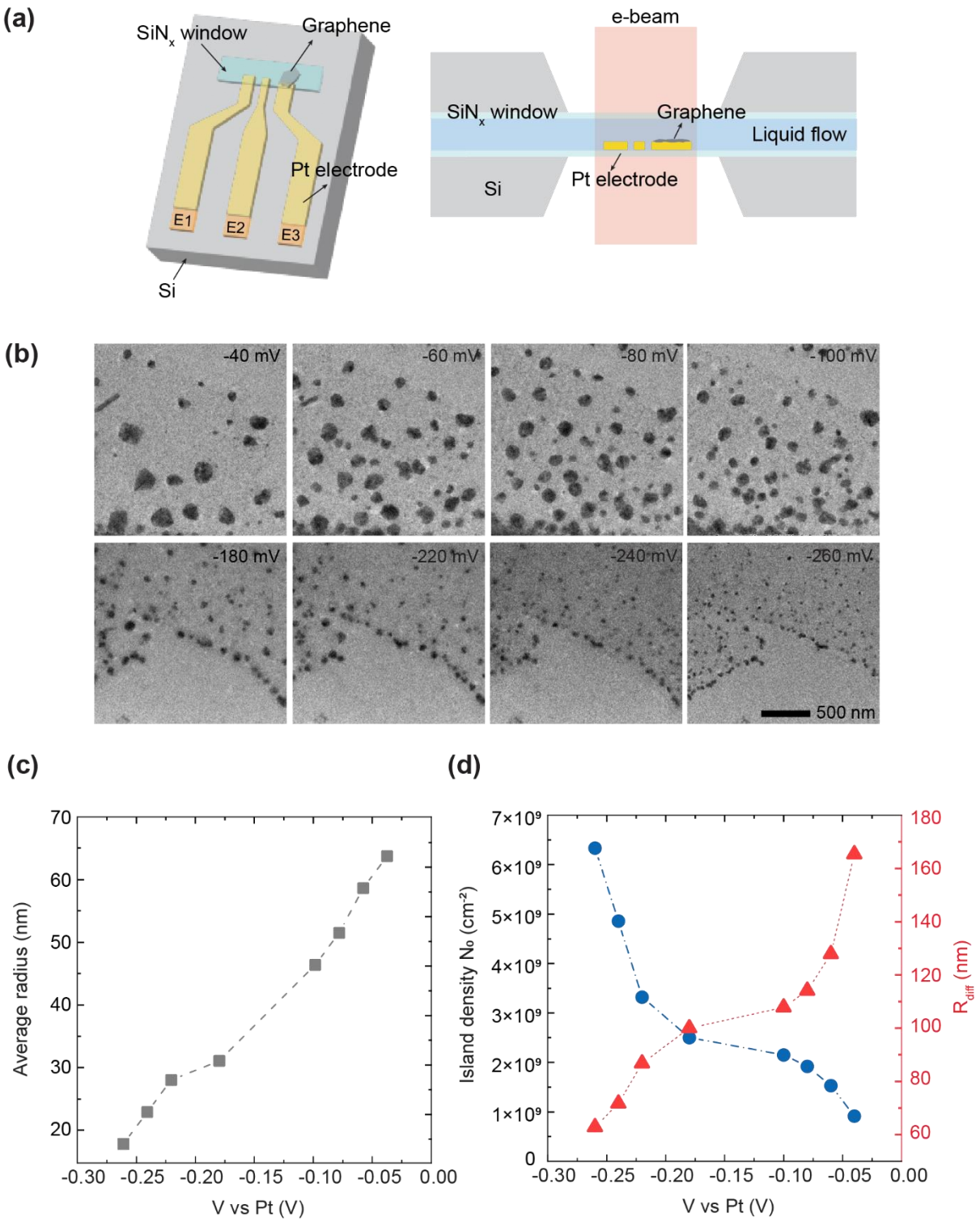

Figure 3-5. 2D materials liquid cell chip and electrochemical pulsing. (a) Schematic view of transferred graphene(grey) onto the Pt electrode (yellow) of the electrochemical liquid cell chip. Electrodes are crossing the SiNx viewing window(cyan) and connected to three contact pads E1,

E2, and E3 which are assigned to counter, reference, and working electrodes. Only the working electrode is modified with the graphene flake unless stated otherwise. (b) *In situ* TEM images at the end of V-on state (t= 10 s) where applied potentials are -40 mV, -60 mV, -80 mV, -100 mV, -180 mV, -220 mV, -240 mV, and –260 mV. Cu islands are deposited on graphene electrode in a chip shown in Fig.1 and filled with 0.1 M $CuSO_4$ + 0.1 M H_2SO_4 electrolyte. (c) Average radius of Cu islands as a function of applied potential. (d) Island nucleation density and maximum hemispherical distance of diffusion of island measured from the image in (b).

3.2.2 Transient Deposition of Nanoparticles

We then discuss the transient deposition and coarsening of nanoparticles during the pulse off stage. As mentioned in the previous section, we observe that when a higher potential is applied during the deposition, the growth of Cu nanocrystals continues after the voltage goes off. The total amount of Cu deposited can greatly exceed the amount deposited in the 10s voltage pulse. This mode of deposition of Cu on graphene is shown in Figure 3-6, with images extracted from a movie recorded during and after pulse voltammetry at -180 mV, -220 mV, -240 mV, and -260 mV for 10 s in the same electrolyte. The first and second row Figure 3-6a Fig shows that Cu islands nucleate and grow on the graphene electrode during the ‘V on’ stage, consistent with results from Figure 3-5. Instead of completely dissolving when the applied potential is turned off, the particles remain at the sites and the growth keeps taking place for at least 50 seconds more, followed by the eventual disappearance of all islands after tens of seconds. Tracking the size of the individual particles shows that smaller particles disappear earlier while the largest particles grow to quite large sizes before eventually disappearing, suggesting the coarsening (Ostwald

ripening) behavior, which a growth of particles while consuming smaller particles which will be explained in detail below. (Figure 3-6b)

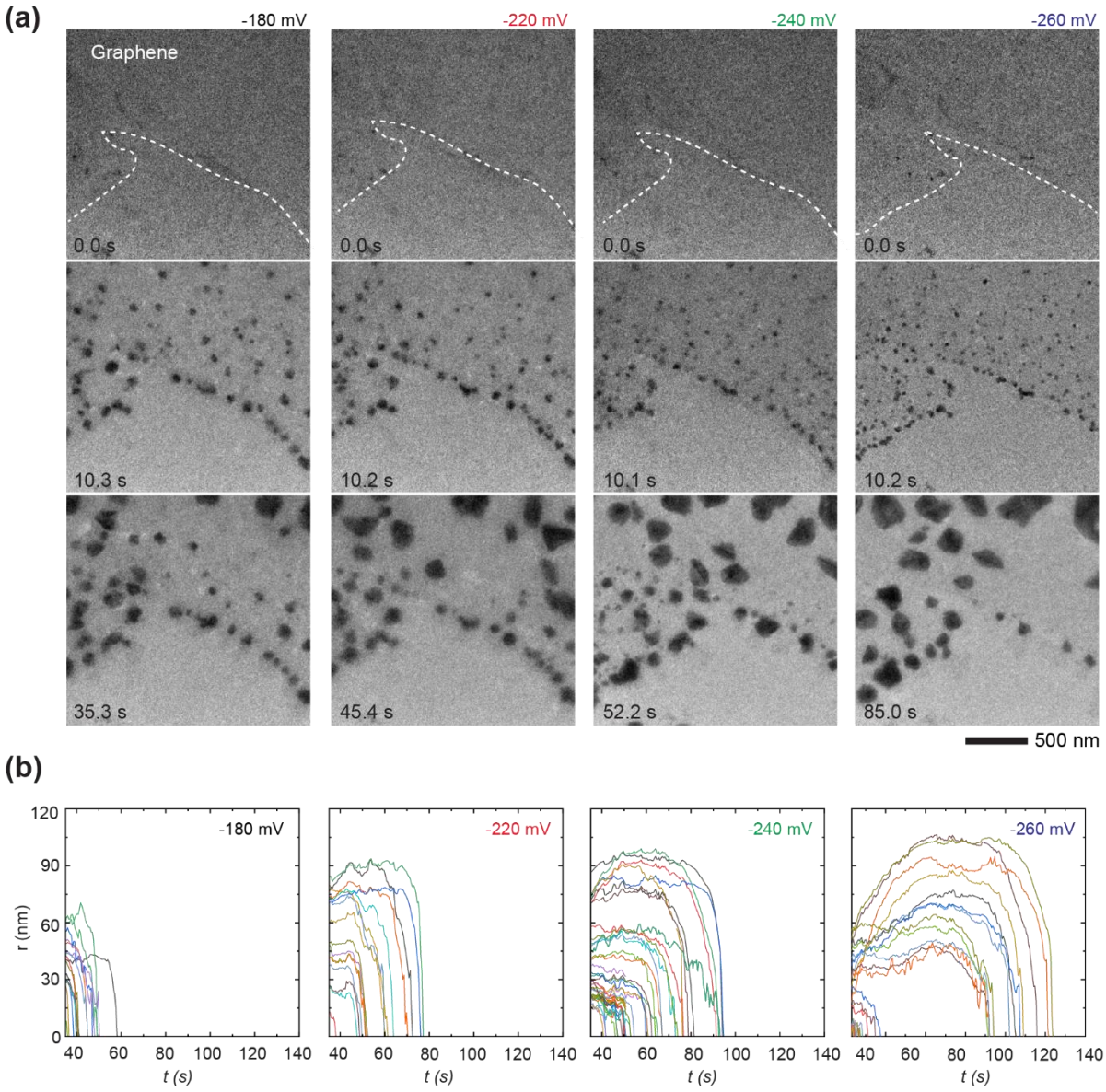

Figure 3-6. Additional growth and coarsening when the potential is off. (a) *In situ* TEM images of Cu islands at potentials of -180 mV (black), -200 mV (red), -240 mV (green) and -280 mV (blue) applied for 10-s pulses for '*V on*' state. The electrochemical liquid cell is filled with 0.1 M $CuSO_4$ + 0.1 M H_2SO_4 electrolyte solution. (b) Radius as a function of time for individual Cu

islands coarsening at different applied potentials: -180 mV, -200 mV, -240 mV and -260 mV. Each line represents radius of islands in the field of view.

We consider several mechanisms that may be responsible for the unexpected transient deposition. One possible explanation for the additional growth could be that Cu is indeed deposited during the potential pulse but does not form into nanocrystals until later. This could arise if Cu is intercalated in the graphene in a uniform manner during the applied potential, with coalescence into islands occurring later.[159] However, the measured charge that flows during the potential pulse is not strongly dependent on voltage, in particular not varying enough to account for the large deposited volume at high potentials. A second possible explanation may be attributed to the capacitance of graphene. Graphene has high capacitance based on electrochemical double-layer capacitance (EDLC) measurements, and it has been shown that the electrochemical interfacial capacitance increases for larger (negative) applied potential. [160] The plots in Figure 3-7a show that the islands grown at negatively higher potential last longer, consistent with additional growth of Cu islands during the pulse-off stage being due to charge accumulation from the capacitance of the graphene when the applied voltage is on. A final mechanism for the effect could be that the application of low cathodic potential may cause the reduction of various oxygen functional groups on the graphene surface, resulting in an increase of –OH groups on the surface. [161] These charged species could sustain additional growth by causing a reduction of Cu ions in the solution.

Finally, we discuss the coarsening of particles accompanied by the additional growth. Coarsening behavior is most clearly shown in the right-most column of Figure 3-6a when the negatively highest potential of -260 mV is applied. This coarsening behavior is still apparent for the

particles formed at -240 mV of applied potential, where the particles with radius 25±5 nm completely dissolves before around t = 50 s as shown in the third panel of Figure 3-6b. At relatively lower applied voltage of -180 mV and – 220 mV, on the other hand, coarsening becomes less obvious.

Temporal evolution of total volume and number of islands after the V on stage (Figure 3-7a) display the potential dependent coarsening behavior. At -180 mV, -220 mV, -240 mV, and -260 mV of applied potential, total particle volume reaches maximum at t =25 s, 45 s, 52 s, and 65 s, and completely dissolve after a few tens of seconds as previously mentioned. The decrease in the number of islands show more apparent coarsening at higher applied potentials. We explain the voltage dependent coarsening of particles by using the classic Ostwald ripening model. The growth rate of particle is as following,[162]

$$\frac{dr}{dt} = -\frac{2(c_0 D)(\bar{V})^2 \gamma_{sl}}{RTr}\left(\frac{1}{r} - \frac{1}{\bar{r}}\right) \qquad \text{(Eq. 4)}$$

where r and $\bar{r}$ are the radius and average radius of the particle, c_0 is the bulk concentration of the electrolyte (0.1 M), D is the diffusion coefficient of Cu^{2+} ions (7.1 x 10^{-10} m^2/s),[163] $\bar{V}$ is the molar volume of copper (7.11 cm^3/mol), γ_{sl} is surface tension or interface energy between Cu particle and electrolyte (19.28 mJ/m^2)[164], R is the gas constant (8.3145 J/mol K), and $T$is temperature (298 K). The above equation explains that particles that are smaller than the average shrink ($\frac{dr}{dt} < 0$, when $r < \bar{r}$), and larger than the average increase ($\frac{dr}{dt} > 0$, when $r > \bar{r}$). Note that the particles that grow the fastest have twice the average size; $r_{max} = 2\bar{r}$. The average sizes of particles formed by applying -260 mV and -240 mV, are 17 and 22 nm. This matches with the

cutoff radius of coarsening at these potentials (15 and 25 nm), which again indicates that the Ostwald ripening is taking place among particles with relatively smaller particle size. Figure 3-7b shows the $\frac{dr}{dt}$ versus r plotted at different potentials, where the average particle sizes used for the plots are measured from the image at t = 10 s. The average sizes correspond to the x- axis intercepts as shown in the inset plot of Figure 3-7b. For smaller magnitude of applied potential of -180 mV and -220 mV, where the coarsening becomes less evident, the average sizes are relatively larger (30 and 29 nm). From the plot, it is evident that the overall growth rate from coarsening is higher when the particle sizes are smaller formed by applying higher potential. This suggests that the coarsening and therefore the final particle sizes at the end can be controlled by tuning the applied potential to form initial particles with desired sizes.

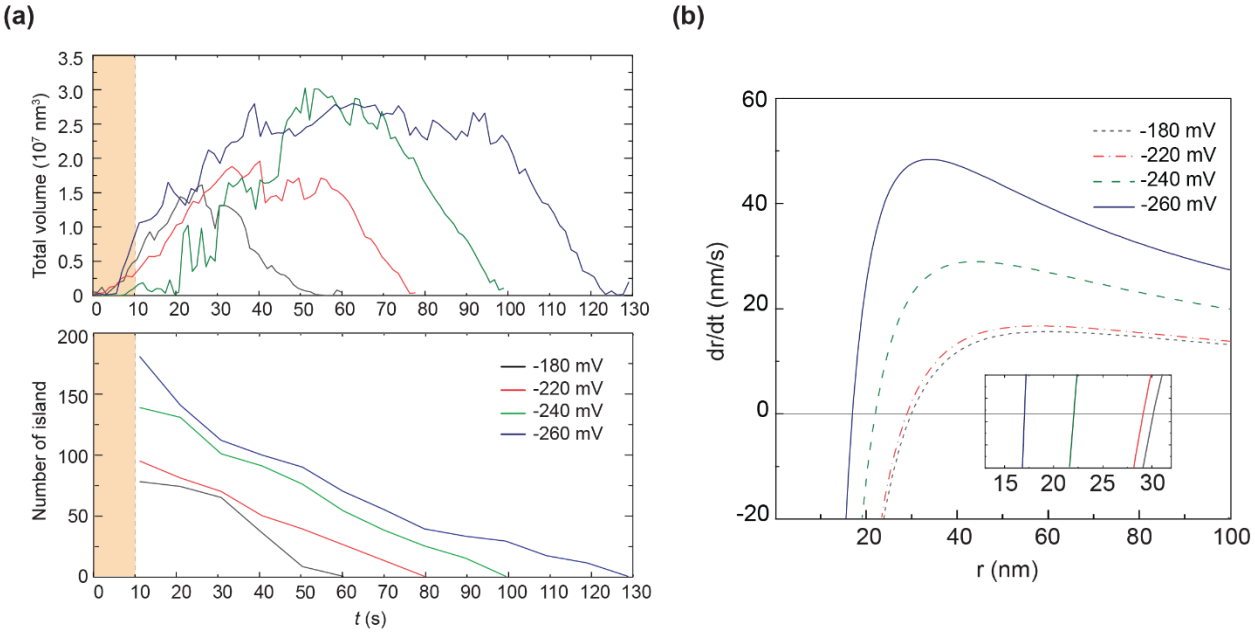

Figure 3-7. Potential dependent volume, number of islands, and coarsening. (a) Total volume and number of islands as a function of time at potentials of -180 mV (black), -220 mV (red), -240 mV (green) and -260 mV (blue). Orange boxes indicate the 10 s of V on state. (b)

Theoretical growth rate of particle (dr/dt) versus radius calculated using the average radius at each potential and

In this chapter, the real-time observations of electrochemical deposition of Cu on graphene using liquid cell TEM show how the applied potential affects the Cu Island size distributions, and corresponding coarsening behavior. The higher driving potential leads to smaller nuclei sizes, which is explained using the nucleation and diffusion-limited growth models. Cu islands dissolve when the potential is turned off to 0 mV, which is attributed to the built-in potential that is near the stripping potential of Cu. When the applied potential is relatively lower, Cu islands immediately dissolve as the potential returns to zero without any coarsening taking place. However, Cu islands continue to grow and dissolve even after the potential is off. We discuss a mechanism arising from the intrinsic chemical and physical properties of graphene. It is possible that the capacitance of graphene and the formation of functional groups for reduction may lead to the growth of other metal nanocrystals too. We also discuss the Ostwald ripening of nanoparticles formed at higher potentials accompanied by additional growth, where the experimentally observed cutoff radii of coarsening agree with the radii calculated from the theories of Ostwald ripening. This study demonstrates the role of graphene as a material that can drive unexpected morphological changes during an electrochemical experiment, and the results could provide guidance for controlling electrochemical growth to tailor deposited structures.

3.3 Conclusion

In this chapter, the role of electrochemical parameters, including temperature, potential, and substrate, in nanoscale electrochemistry is discussed. In particular, we explain how we can

control each parameter to tailor the electrochemical deposition. First, the electrochemical liquid cell TEM experiment coupled with heating capability demonstrates the effect of temperature on the deposition of copper under galvanostatic conditions. On top of the accelerated growth rate at increased temperatures, how temperature affects the kinetics of the electrochemical deposition, namely, the transformation from reaction-limited growth to diffusion-limited growth is explained. This heating strategy can be used to localize electrochemical reactions in the liquid cell for quantitative electrochemical measurements. We also capture the transient deposition phenomena along with coarsening and dissolution on a 2D material substrate. The results show that applied potential can control the nuclei density and size distribution, following the classical electrochemical nucleation and growth theory. However, it is also important to take into account of intrinsic physical and chemical properties of the 2D material substrate on the electrochemical deposition of the metal nanoparticles, as they can induce dissolution, additional growth, and coarsening of the deposited structures. Therefore, we suggest that the findings from electrochemical liquid cell TEM combined with the control of various parameter can give more comprehensive insight on the nanoscale electrochemistry.

Chapter 4. Structural Dynamics of Nanoparticles in a Gas Environment

Real-time observation of these catalysts using *in situ* TEM can lead to comprehensive insights by capturing dynamic structural change under environments with controlled gas and temperature.[165–168] Moreover, due to the 3D nature of the morphological features of catalyst support and surface reaction being the critical process in deactivation, projected 2D images can

be complemented by surface-sensitive topographical 3D images. Tomography[169] is one technique that can provide 3D images, but the temporal resolution is not high enough to capture the dynamics of the catalysts. Therefore, the simultaneous acquisition of 2D images with projected information and 3D images with surface-sensitive information with a high temporal resolution during the gas exposure has the potential to characterize the dynamics of nanoparticles, support, and interplay with gas that could lead to the degradation of the catalyst. In this chapter, we present the real-time observation of 2D and 3D structural dynamics of nanoparticles on support in different gas environments using *in situ* electron microscopy using Pt nanoparticle on carbon (Pt/C) as a model system. Gas environment and temperature are used as stimuli to introduce dynamics in the Pt nanoparticles and carbon support including sintering and support degradation. We use environmental transmission electron microscopy (ETEM) to provide a spatially and temporally resolved view via high-angle annular dark-field scanning TEM (HAADF-STEM) of immediate changes under environments defined by gas composition and temperature. In order to capture the surface-sensitive dynamics in 3D topography, we combine the STEM images with secondary-electron (SE) images acquired using the SE detector during the same scan for complementary information on the surface features of the catalyst particles and their support. A combination of STEM images with SE images has been previously shown high spatial resolution up to atomic scale imaging.[170–172]

4.1 Dynamics of Particles and Support Degradation in Gases

We examined the structural dynamics of Pt nanoparticles on carbon support in O_2, H_2O, and H_2 environments using *in situ* HAADF-STEM and SE images. In order to investigate the effect of the surface area of the support, which interacts with the nanoparticle and therefore affects the

performance, we used two commercial-grade catalysts with different surface areas: Ketjenblack and Vulcan. Vulcan is known as a medium surface area support (250 m^2/g), and since Ketjenblack (800 m^2/g) has almost 3 times higher surface area than Vulcan,[173] we refer to these supports as “higher” and “lower” surface area supports. Commercial-grade catalysts with Pt nanoparticles on the carbon support are deposited on the heating chip and mounted on a holder for temperature control. After inserting the holder, gas is introduced with a flow rate fixed to 1.0 sccm with the temperature control.

In every gas environment, PMC is dominantly observed, but the onset temperature of the migration is dependent on the gas, indicating the different interactions between the gas, particle, and support. Moreover, SE images reveal the Pt nanoparticles dynamics across the carbon support and through the support. SE images also show the degradation of carbon support by forming a trench along the continuous migration of Pt nanoparticle in O_2 and H_2 gas, which could be attributed to the chemical reaction between the gas and the nanoparticle. This indicates that 3D morphology captured by SE images is also an important factor in addressing the structural dynamics and degradation of catalysts. The dynamics observed are not strongly dependent on the porosity of the support, suggesting that the process is more dependent on the particle and gas interaction. Oriented attachment of Pt nanoparticles in an H_2O gas environment is observed, which is coherent with the theoretically studied effect of H_2O gas dissociation and hydrogen bond formation on the oriented attachment in catalytic nanoparticles.

4.1.1 Dynamics in Oxygen Environment

We first discuss the effect of the gas environment on the migration rates of Pt nanoparticles. To compare the migration rate, we find the temperature at which the motion of Pt nanoparticles

migrating a distance over 1 nm within 5 seconds is observed in the field of view. We call this the onset temperature, and there is no motion of particles longer than a 1 nm distance below this temperature over 5 minutes of observation. The onset temperature of PMC varied by the gas environment, and the onset temperature of PMC was at 300 ˚C in O_2 gas. Figure 4-1 shows the series of HAADF-STEM and SE images depicting the structural dynamics of Pt nanoparticles on a high surface area carbon support in O_2 gas (2.4×10^{-2} Pa) at the onset temperature. HAADF-STEM image series of Pt nanoparticle dynamics on the carbon support in the earlier stage of the experiment (Figure 4-1a) depicts that the migration kinetics took place within a few tens of seconds. Representative examples of PMC are shown within white dotted boxes of Figure 4-1a, where the particles indicated by white arrows are migrating and merging. Further migrations were followed by the merged particles, which is one of the clear evidence of PMC.[168] Another important feature observed is the continued movement of particles regardless of their size and shape. Constant migration of the particles led to the various time durations of PMC, as indicated by PMC lasting over several minutes in Figure 4-1b, compared with 20 seconds of duration in Figure 4-1a. After the duration of PMC, the motion stops until the end of the experiment. Moreover, the time series of SE images (Figure 4-1c) simultaneously acquired with HAADF-STEM revealed the dynamics of Pt nanoparticles relative to the carbon support. Dotted boxes of Figure 4-1b and 4-1c indicate the region where particles embedded in the carbon support migrate and coalesce until $\Delta t = 2$ minutes. After the particles merge, SE images (Figure 4-1c) display how the merged particles rise above the support and move along the surface. Note that a few nanometers thick of carbon is thick enough to block the SE signal from the material below, which again suggests that the SE from the Pt particles are not coming from beneath the carbon support, and therefore Pt particles are indeed above the support surface as shown in the SE

image.[174] These HAADF-STEM images coupled with SE images demonstrate that the particles undergo dynamics not only within the support or on the support, but also pass through the support which is difficult to capture using only with 2D projected images and static 3D topological images. In addition, the SE image captured how trenches are formed near migrating particles following their pathway, as indicated by the black arrows in Figure 4-1c. Since trenches are formed along the migration path, we suggest that these can be attributed to the carbon corrosion in O_2 catalyzed by Pt nanoparticles.[175] Trench formation could be explained through the asymmetric nature of the boundary between the Pt nanoparticle and the surface of the support, leading to the propagation of the trench in a single direction. Trench formation on the support also explains the continuous migration of the nanoparticle since the nanoparticles make less contact with the support as the support corrodes along the trench, and therefore, the relative driving force from the interaction between the gas and the nanoparticles becomes stronger leading to the continued migration. The mechanism of support corrosion is critical as it is one of the significant contributors to the catalyst surface area loss by possible particle detachment. [176–178] This suggests that *in situ* SE images can be used to understand the degradation mechanisms of catalysts not only limited to sintering but also support corrosions.

Note that the particles show round morphology, which is previously reported as the result of an increase in the percentage of higher-order facets compared to faceted surface morphology from lower-order planes in the H_2 environment.[179] Although we found that the sintering captured in our results was dominated by the PMC process, it is important to note that the role of OR should be addressed in the actual sintering process, although higher temporal resolution would be required to experimentally capture the OR.[53] Another critical assumption of OR is the immobility of the smaller particles. However, previous studies have shown that the energy barrier of particle

migration is lower when the nanoparticle sizes are smaller, indicating the possibility of small particles generated by OR being swept away by PMC,[50,52,53] therefore making it experimentally difficult to probe.

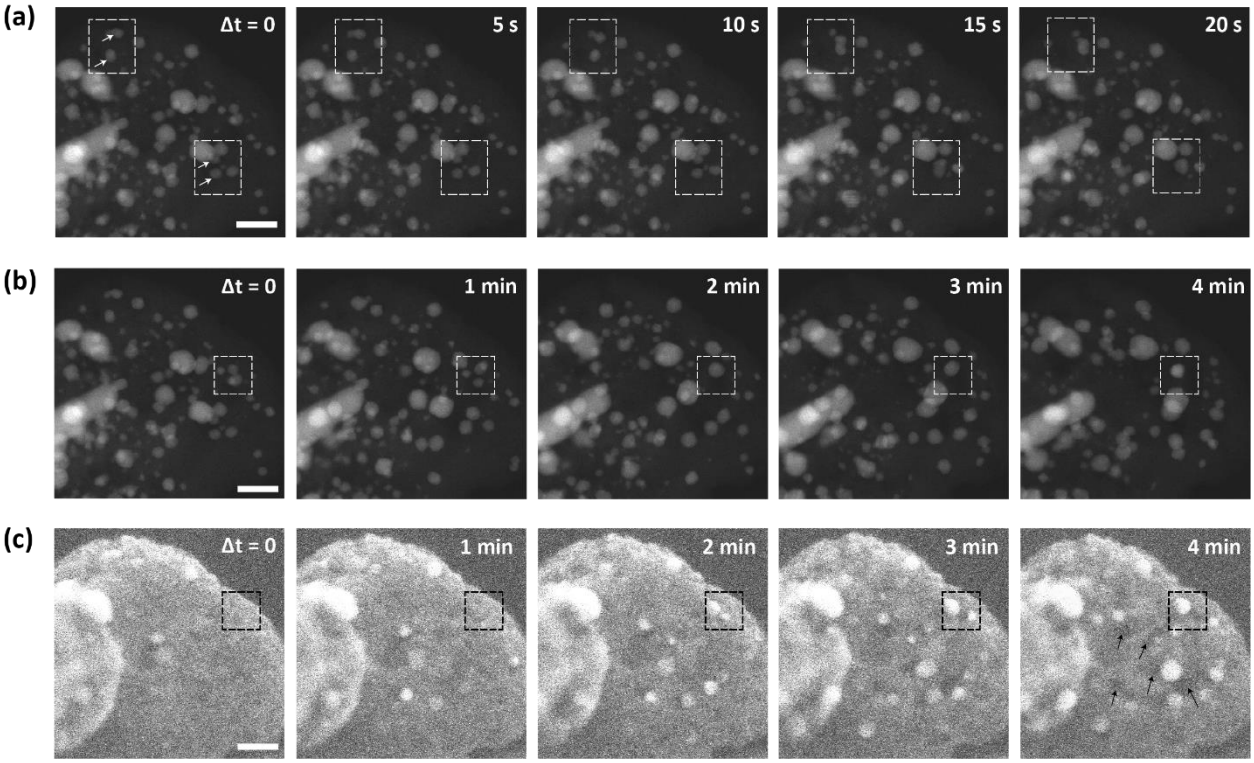

Figure 4-1. Structural dynamics of Pt nanoparticles on a high surface area carbon support in O_2 gas (2.4×10^{-2} Pa) at 300 ˚C. (a) HAADF-STEM image series showing migration and coalescence of Pt nanoparticles within 20 seconds. Particles indicated by white arrows in white-dotted boxes migrate and coalesce. (b) HAADF-STEM image series showing coalescence of 3 individual Pt particles over several minutes followed by migration in the region indicated by the white dotted rectangle, and (c) corresponding SE image series indicating a particle rising above the surface followed by migration along the surface as indicated by black dotted boxes. Black

arrows indicate the trenches formed along the migration pathway of the particles. Scale bars are 10 nm.

2D and 3D structural dynamics of Pt nanoparticles on a low surface area carbon support were also investigated, as depicted in Figure 4-2. The surface area of the support is three times less than the support used in Figure 4-1,[173] but the dynamics observed were similar as it mainly captured the PMC of the particles. HAADF-STEM image series in Figure 4-2a shows the PMC on a low surface area carbon support over a few minutes of duration, which is comparable to the duration of PMC on high surface area carbon support, as shown in Figure 4-1b. Simultaneously acquired SE images (Figure 4-2b) show how particles migrate and coalescence, followed by further migration and sinking below the carbon support as indicated in the white dotted box. SE images also show that the carbon support in the dotted box transforms from an extrusion to a relatively flat surface as particles migrate over, similar to the trench formation from carbon corrosion catalyzed by Pt in Figure 4-1c.

Previous studies have demonstrated that the migration of Pt nanoparticles on graphite surfaces in O_2 gas is the combined result of chemisorption, which is a strong gas-particle interaction, and a weak van der Waals interaction between particle and substrate.[180] Along with chemisorption, an oxygen environment can also lead to oxide growth to dewet Pt nanoparticles, which is another mechanism that facilitates migration.[181] Therefore, similar dynamics of PMC on carbon supports with different surface areas suggest that the process is indeed dominated by the interaction between the particle and the gas molecule. Moreover, a similar pattern of support degradation potentially caused by carbon corrosion is captured on both supports, suggesting that the overall

process is mainly governed by the effect of gas on the support. This could potentially guide through the role of carbon support in activating specific mechanisms of Pt degradation.

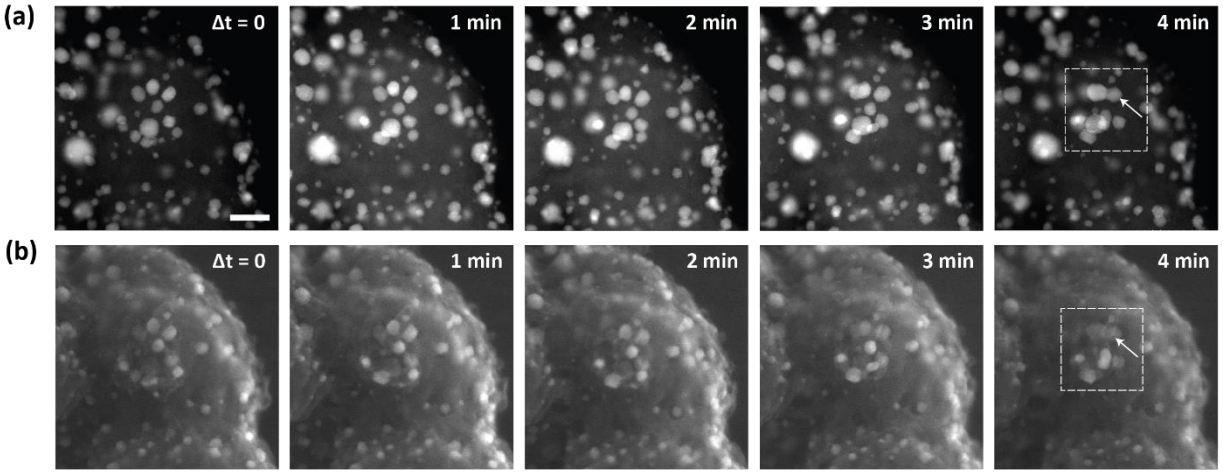

Figure 4-2. Structural dynamics of Pt nanoparticles on a low surface area carbon support in O_2 gas (2.4×10^{-2} Pa) at 300 ˚C. (a) HAADF-STEM image series showing PMC of Pt nanoparticles over several minutes and (b) corresponding SE image series indicating a particle sinking below the surface following the PMC as indicated by the white dotted box. Scale bars are 10 nm.

4.1.2 Dynamics in Water Vapor Environment

We further studied the structural dynamics of Pt nanoparticles on a high surface area carbon support in H_2O gas (2.0×10^{-2} Pa) at the onset temperature of PMC at 500 ˚C (Figure 4-3).

Higher onset temperature in H_2O gas can be attributed to the weak Pt-H_2O interaction compared to Pt-O_2 interaction.[181] Since H_2O is intactly adsorbed on the Pt surface, Pt on the carbon support is not as destabilized as in O_2 gas, leading to a higher kinetic energy barrier for migration of Pt nanoparticles in H_2O gas compared to O_2 gas and therefore higher onset temperature. Pt nanoparticles migrated and coalesced when they were exposed to H_2O gas as shown in the white

dotted box in Figure 4-3a, and similar behavior of PMC occurs on a low surface area carbon support.

However, in contrast to the continuous migration dynamics in O_2, Pt nanoparticles are discontinuous and display interrupted motion. This could be attributed to the less chemical reaction between the H_2O gas and the support that causes the degradation of the support which leads to the trench formation and the continuous migration motion of the particles.

An interesting feature to note is that particles displayed apparent oriented attachment behavior (Figure 4-3b). Series of HAADF-STEM images in Figure 4-3b show the region of the dotted box in Figure 4-3a over 15 seconds, where particles indicated by two white arrows migrated, rotated as they become close to each other to match the orientation of (111) plane, and merged. To the best of our knowledge, the oriented attachment of Pt nanoparticles in H_2O gas has not been captured in real time. Indeed, Raju et al.[182] have theoretically shown that the nanocrystals can reorient themselves and coalesce via oriented attachment when exposed to water vapor which agrees with our observation. Using molecular dynamics simulations, the authors explained that the oriented attachment followed by coalescence is accomplished by the creation of dynamic network of hydrogen bonds formed between surface hydroxyl groups and surface oxygens. In this regard, *in situ* images shown in Figure 4-3 can be an experimental demonstration of the effect of H_2O gas on the oriented particle attachment and PMC. This demonstration is critical as hydroxyls and surface oxygens are also known to play active roles in oxidative catalytic reactions.[183,184]

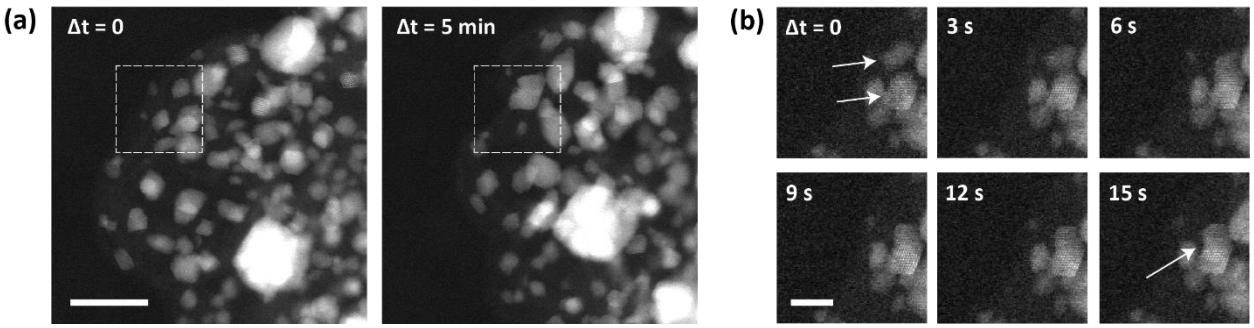

Figure 4-3 Structure dynamics of Pt nanoparticles on a high surface area carbon support in H_2O gas (2.0×10^{-2} Pa) at 500 ˚C. (a) HAADF-STEM images showing particles before and after PMC over 5 minutes and (b) Enlarged HAADF-STEM image series of the region indicated by the white dotted box in (a), showing the early stages of oriented attachment during PMC. Scale bars in Images (a) and (b) are 10 nm and 3nm, respectively.

4.1.3 Dynamics in Hydrogen Environment.

In contrast, when Pt nanoparticles on a high surface area carbon support are exposed to H_2 gas (2.1×10^{-2} Pa), PMC followed by further migration was also observed, although the onset temperature was at 700 ˚C (Figure 4-4), higher than that of in O_2 or H_2O gas. One of the possible explanations for the higher onset temperature in the H_2 gas is the weak interaction between the H_2 gas and Pt nanoparticles, which is known as the weak chemisorption of H_2 on Pt.[185–187] This is in contrast with the previously mentioned strong chemisorption of O_2 on Pt nanoparticles leading to PMC. At the onset temperature, particles indicated by the white dotted box in Figure 4-4a migrated and coalesced after 1 minute, followed by the additional migration of the merged particle. These dynamics are similar to the dynamics in O_2 or H_2O gas, but it is important to note that some of the particles showed faster migration kinetics in H_2 gas than in O_2 or H_2O gas. One of those particles indicated by the yellow dotted box in Figure 4-4a and 4-4b has the average

migration rate of 20 nm/minute and spans over a few tens of nanometers of distance, whereas the particles in O_2 or H_2O move within a few nanometers. After the system reaches the threshold thermal energy to overcome the energy barrier from the weak interaction between gas and nanoparticles, we suggest that the migration kinetics of Pt nanoparticles follow the Arrhenius relation, leading to the faster migration in H_2 .[52] Moreover, trenches on the support were formed along the migration pathway as indicated by yellow arrows which is similar to the dynamics in O_2 gas.

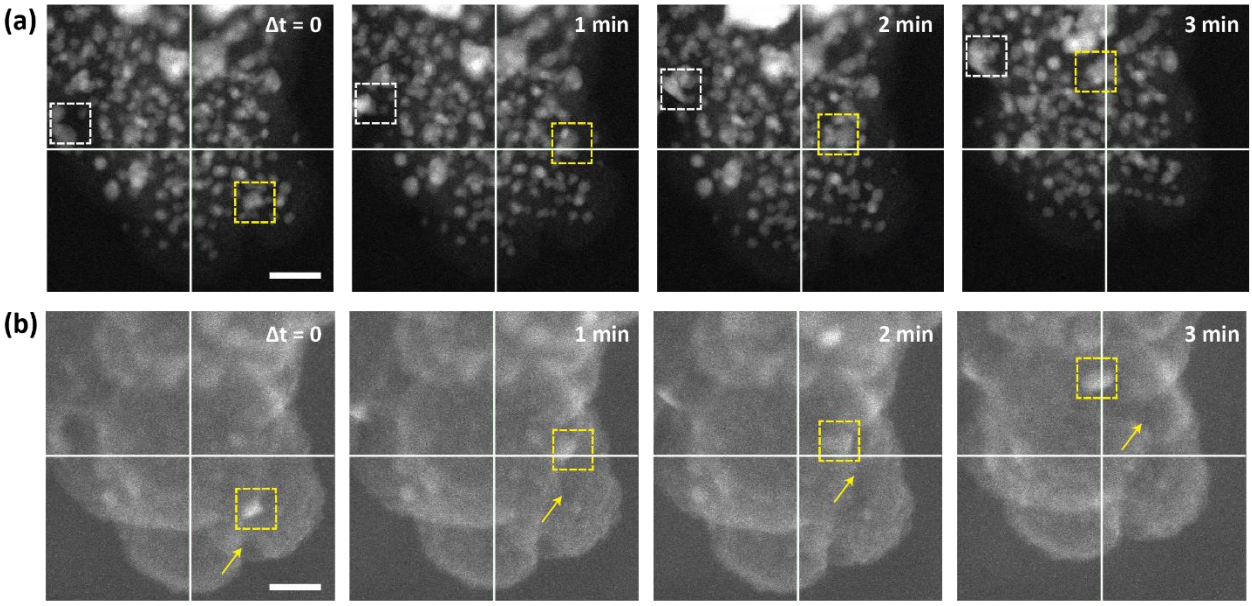

Figure 4-4. Structural dynamics of Pt nanoparticles on a high surface area carbon support in H_2 gas (2.1×10^{-2} Pa) at 700 ˚C. (a) HAADF-STEM image series showing migration and coalescence of Pt nanoparticles over several minutes. Particles indicated by the white dotted box migrate and coalesce, and the particle indicated by the yellow dotted box shows fast migration kinetics. (b) SE image series corresponding to (a), also indicates a particle with fast migration kinetics within the yellow dotted box. Yellow arrows indicate the trenches formed along the migration pathway of the particles. Scale bars are 10 nm.

The degradation of carbon support was more apparent on the low surface area carbon support (Figure 4-5), captured in the HAADF-STEM (Figure 4-5a) and SE image (Figure 4-5b) series, along with the sintering of Pt nanoparticles. We suggest that trench formation on the carbon support along with the continuous migration of the Pt nanoparticles is due to the catalyzed asymmetric support degradation, similar to the dynamics in O_2, but it is possible that the chemical mechanisms may be different. The carbon support degradation in H_2 can be attributed to the reaction between the carbon support and the gas. One of the feasible reactions is the formation of gaseous CH_4, which is reported to be possible at high temperature around 800 ˚C when catalyzed by metal catalysts.[188] The reaction between H_2 and sulfur in the carbon support could also contribute to the support degradation. Sulfur and H_2 react to form H_2S, as often takes place in coal desulfurization reactions during pyrolysis.[189,190] Previous study has shown that commercial-grade carbon supports that are also used in this study have sulfur content, which leads to the mass loss after exposure to H_2 gas.[173] Therefore, carbon support degradation in different gas environments should be interpreted while considering the interaction between the gas and the components of the support, along with the interaction of the gas and particle.

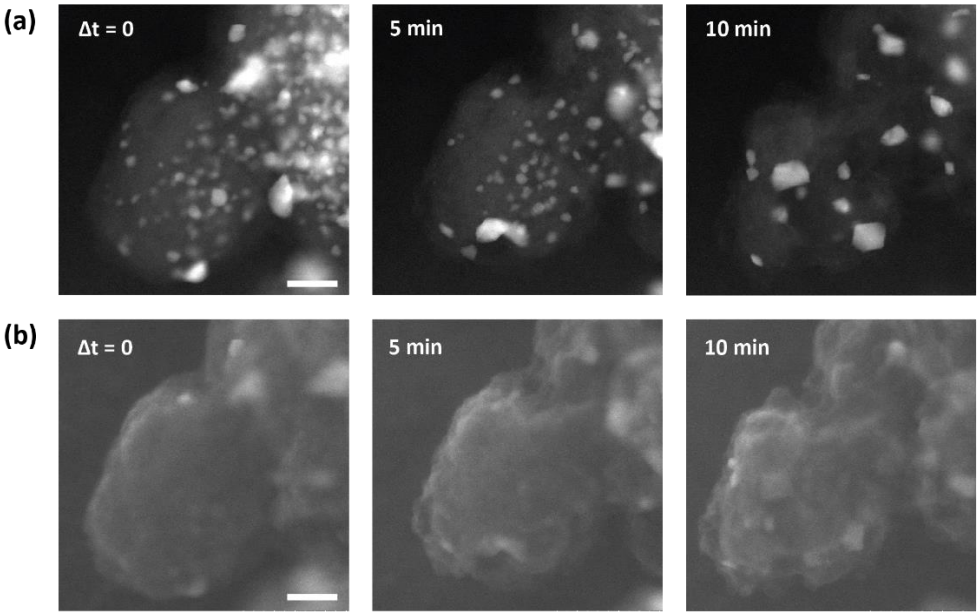

Figure 4-5. Structural dynamics of Pt nanoparticles on a low surface area carbon support in H_2 gas (2.1×10^{-2} Pa) at 700 ˚C. (a) HAADF-STEM images showing particles before and after PMC and degradation of carbon support over 10 minutes and (b) corresponding SE image series. Scale bars are 10 nm.

We suggest that trench formation on the carbon support along with the continuous migration of the Pt nanoparticles is due to the catalyzed asymmetric support degradation, similar to the dynamics in O_2, but it is possible that the chemical mechanisms may be different. The carbon support degradation in H_2 can be attributed to the reaction between the carbon support and the gas. One of the feasible reactions is the formation of gaseous CH_4, which is reported to be possible at high temperature around 800 ˚C when catalyzed by metal catalysts.[188] The reaction between H_2 and sulfur in the carbon support could also contribute to the support degradation. Sulfur and H_2 react to form H_2S, as often takes place in coal desulfurization reactions during pyrolysis.[189,190] Previous study has shown that commercial-grade carbon supports that are also

used in this study have sulfur content, which leads to the mass loss after exposure to H_2 gas.[173] Therefore, carbon support degradation in different gas environments should be interpreted while considering the interaction between the gas and the components of the support, along with the interaction of the gas and particle.

4.2 Interplay between Particle-Support-Gas

We finally discuss the combinative interplay between the Pt nanoparticle, support, and the three different gas environments used in this study. First, the onset temperature of the dynamics can be explained by the difference in the interaction energy between the gas and the particle. Since the interaction between the O_2 and the Pt nanoparticle is stronger compared to the interaction with H_2O and H_2, the onset temperature is the lowest in O_2 as it requires the smallest thermal energy to overcome the kinetic barrier. Moreover, in O_2 and H_2 gas, supports are degraded along the trench following the continuous migration of the Pt nanoparticles, whereas in H_2O gas, local support migration is not observed, and the migration is discontinuous and interrupted by pinning on the support. This could be attributed to the catalyzed chemical reaction between the carbon support and the O_2 and H_2 gas that leads to the support degradation, which does not occur in H_2O gas. The asymmetric nature of the boundary between the particle and the support leads to directional degradation and, therefore, trench formation. Along the degraded trench, the particles experience less hindrance of migration caused by the interaction with the support, which also explains the continuous migration of nanoparticles in O_2 and H_2 along with the trench formation.

4.3 Conclusion

In this chapter, the structural dynamics of Pt nanoparticles on carbon support, mainly including sintering via PMC and carbon support degradation were investigated using ETEM. Dynamics

were observed in 2D and 3D, which were simultaneously acquired by HAADF-STEM and SE images. PMC was the dominantly observed pathway of sintering in every ETEM experiment, and even after PMC, merged particles migrated at extra distances. More importantly, SE images revealed that Pt nanoparticles not only move across the carbon support but also migrate through the carbon support, which was most clearly shown in the dynamics of Pt nanoparticles in O_2. This suggests that the 3D morphology of particles on the support should also be considered while understanding the structural dynamics of the catalysts. In addition, SE images captured the trench formation on the support due to its degradation in O_2 and H_2, although the potential chemical reaction mechanisms are different. The trench formation and the support degradation also lead to the continuous migration of Pt nanoparticles in O_2 and H_2, whereas interrupted migration motion is captured in H_2O. The difference in the dynamics' onset temperature can be attributed to the variation in the interaction strength between the gas molecule and the Pt nanoparticle. Variations in the support degradation, migration of the particles, and the onset temperature of the migration indicate the different interactions between the gas, particle, and support, which is relevant to the design of catalytic materials. In particular, particles showed oriented attachment behavior in H_2O, which could be used as a demonstration of the theoretical studies on the effect of H_2O gas and hydrogen bond formation leading to the oriented attachment in catalytic nanoparticles. These results reveal the complex interaction between the different chemical species in a dynamic and evolving environment. Therefore, we suggest that ETEM experiments that reveal 2D and 3D dynamics combined with theoretical studies would lead to more comprehensive and universal insights into catalyst degradation mechanisms. Moreover, this work can suggest the guidelines for the engineering decision-making process regarding materials

selection, operating conditions, and assessing the lifetime of catalysts using the 2D and 3D dynamics captured from ETEM.

Chapter 5. Conclusion and Outlook

5.1 Conclusion

This thesis begins with the introduction to the need for *in situ* electron microscopy of nanomaterials dynamics for applications in optimizing functional materials. Functional materials, especially materials used in energy storage or conversion technologies experience dynamic physical and chemical changes during the reaction or operating cycles. Investigating the dynamics in real-time gives insight into the structure-property-performance relationships of those materials, contributing to the designing of energy materials with improved performance and lifetime.

In Chapter 2, I summarized the temperature-dependent electron beam induced nanocrystal growth captured in liquid cell TEM. I combined the microscopy results with the model I developed, which is the temperature-dependent radiolysis model to interpret the growth kinetics of the metal nanocrystals. The model I developed includes the temperature-dependent parameter and full reaction sets including the precursor materials and coupled anions. I showcased the use of the model by applying it to another metal system; the growth of branched Pd nanocrystals. I demonstrated that the branched nanocrystals were formed under a surface reaction-limited regime, which was generally known to be possible through diffusion-limited growth. The results in this chapter suggests that the temperature-dependent modeling of the chemical environment combined with microscopy can provide the guideline for the correct

interpretation of the thermally controlled liquid cell TEM experiments and also insights into the synthesis process for nanocrystals with desired structures.

In Chapter 3, I discussed the nanoscale electrochemistry under a controlled environment, in particular, the effect of temperature and the substrate on the kinetics of the electrochemical deposition of Cu. I demonstrated that the temperature not only accelerates the growth rate by enhancing the reaction rate but also affects the transition of growth modes. In particular, I used the calculation of the temporal evolution of the concentration profile to show that at higher temperatures, the transition from the reaction-limited to the diffusion-limited growth is faster compared to the lower temperatures. I also demonstrated the effect of 2D material graphene as a substrate for the electrochemical deposition of Cu. Along with the classical nucleation and growth during the pulse on stage, transient deposition and coarsening occurred after the pulse was turned off. I attribute this additional growth to the intrinsic chemical and physical properties of graphene that allow it to hold additional charges to reduce the Cu ions. These results suggest that the understanding of the effect of electrochemical parameters enables the nanoscale control of the electrochemical phenomena.

In Chapter 4, I summarized the structural dynamics of supported nanoparticles for catalytic applications in a gas environment using simultaneously acquired 2D projection images and 3D topographical images. Pt on carbon catalysts, which are commonly used catalysts for fuel cells, was used as a model system. In every gas environment that was tested (O_2, H_2O, H_2), PMC was dominantly observed. However, the onset temperature of the dynamics was the highest in H_2, followed by H_2O and O_2, reflecting the kinetic energy barrier from the gas and particle interaction that the particles should overcome. Secondary electron images for 3D topography have captured that particles also migrate through the surface along with the movement across the

surface. Moreover, 3D topography images captured that in O_2 and H_2, continuous migration of the particles along with the trench formation of the support takes place, which could be attributed to the local degradation of the support catalyzed by the Pt nanoparticles. In H_2O on the other hand, discontinuous motions were captured, but oriented attachment of the particles via hydrogen bond formation among the H_2O vapor was observed, which has only been theoretically predicted. These results demonstrated that the combination of TEM 2D images and Secondary Electron 3D topography images can be a tool to explain the interplay between particle-support-gas.

Overall, this thesis shows the assessment of nanostructure dynamics under controlled environments using *in situ* TEM with a combination of external stimuli. *In situ* TEM coupled with an understanding of the physical and chemical environments can provide insight into the nanostructure dynamics, which could contribute to revealing the degradation mechanisms of energy materials.

5.2 Opportunities and Challenges for Electrochemical Liquid Cell TEM

In this chapter, opportunities and challenges to broaden the scope of *in situ* TEM for studying nanomaterial dynamics are discussed. The experimental challenges of liquid cell TEM to more accurately mimic the realistic operating conditions of electrochemical energy materials are explained, including the effect of organic compounds and the role of non-continuous pulses.

5.2.1 Addressing the Effect of Organic Materials: Electrolytes, Ligands

Many of the most promising materials systems for energy conversion involve organic compounds in their operations. For example, lithium-ion batteries are usually cycled in organic

liquid electrolytes,[191] and most of the recent synthesis of mental nanoparticles for catalytic applications involve the use of organic solvent and electrolyte.[192] In order to properly expand the applicability of liquid cell TEM towards nanomaterial systems with organic materials, it is important to understand the potential reactions and side effects that can be induced by these materials.

First, I introduce the results of liquid cell TEM of electrochemically cycling battery anode materials in organic electrolyte. Besides the morphology change on the electrode and the electrode/electrolyte interface, understanding the electrochemical degradation of electrolytes is critical to fully describe the battery operation in liquid cell TEM. The electron beam effect on the stability of the organic electrolyte must be quantified to extract quantitative information. The electron beam induced radiolysis of an aqueous solution system and temperature effect on it have been discussed in the previous section. However, in more complex solutions such as lithium-battery electrolytes, the hydrated electrons, and other beam indued radicals will interact through secondary chemical reactions. For example, one of the commonly used Li salt – lithium hexafluoroarsenate ($LiAsF_6$) dissolved in organic electrolyte goes through the following reaction with the hydrated electron [193,194]

(1) $AsF_6^- + 2e^- \leftrightarrow AsF_3 + 3F^-$ (2) $3F^- + 3Li^+ \leftrightarrow 3LiF$

Total: $LiAsF_6 + 2e^- + 2Li^+ \leftrightarrow AsF_3 + 3LiF$

Once AsF_3 is formed from reaction (1) at a high rate ($K_e = 9 \times 10^9 M^{-1}s^{-1}$),[195] precipitation of LiF can occur, where LiF is frequently observed on electrode cycles after battery cycling. Electron beam-induced breakdown of various electrolytes ($LiAsF_6$ salt dissolved in 1,3-dioxolane (DOL), dimethyl carbonate (DMC), and a mixture of DMC and ethylene carbonate

(EC). lithium triflate (LiTf) in dimethyl sulfoxide (DMSO), $LiPF_6$ in EC/DMC) has already been systematically investigated upon electron beam irradiation under controlled electron dose. [196]
As a demonstration of capturing the cycling of battery anode material in organic solvent, we used Tin oxide (SnO_2)/zinc oxide (ZnO) core/shell nanowires in 1.0M $LiPF_6$ in vol% 1:1:1 mixture of EC/DMC/diethyl carbonate (DEC). However, as soon as the electron beam was irradiated, nanoparticles precipitated near the anode and bubbles formed in the electrolyte along with the decrease in the intensity (Figure 5-1). These results indicate that the potential reactions with the organic electrolyte with the electron beam induced radiolysis should be addressed and the windows of the electron beam dose should be chosen accordingly in order to decouple the effects from the electron beam irradiations and the electrochemical cycling results.

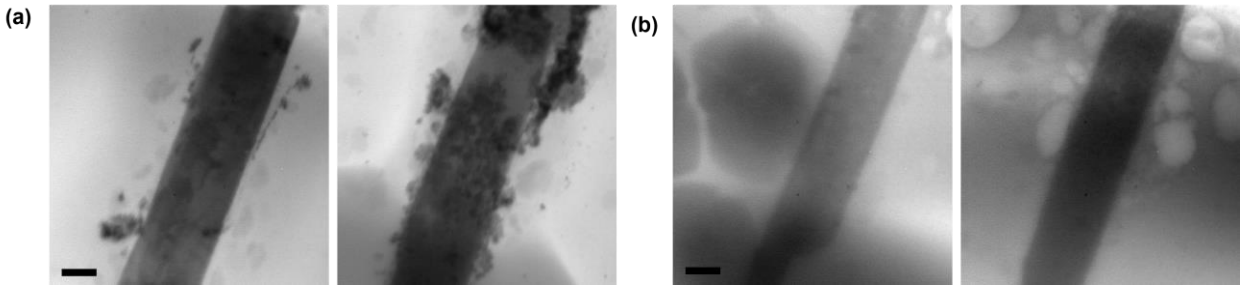

Figure 5-1. Liquid cell TEM of SnO_2/ZnO core/shell nanowires using organic electrolytes. Electron beam effect on the (a) precipitation and (b) electrolyte degradation. Scale bars are 200 nm.

Moreover, organic compounds could potentially impede the measurement of electrochemical signals and morphological changes during reactions under current or voltage applications. As previously mentioned, metal nanoparticles are usually synthesized using organic solvents, surfactants, and ligands. Therefore, synthesized metal nanoparticles are likely to have organic residue on the surface which could affect the electrochemical reactions that usually takes place

on the surface. We used commercially available synthesized Pt nanoparticles with bimodal sizes (d= 30 nm and 70 nm) to induce Ostwald ripening, which is one of the most well-known mechanisms for sintering that reduces the active surface area (Figure 5-2 a and 5-2b). We placed the nanoparticles on the electrodes of the liquid cell chip for electrochemical cycling. However, the cyclic voltammogram (CV) (Figure 5-2 c and 5-d) showed only the peaks from unstable and rapid bubble formation from gas formation, without the peaks indicating the redox reactions on Pt, including desorption and absorption of H, and reduction and oxidation of Pt-O. The lack of essential peaks in the CV could be attributed to several factors including the insufficient electrical connection between the electrode and the Pt nanoparticles, but it is important to acknowledge the effect of organic residues that could alter the CV. [197] Therefore, nanoparticles should be properly cleaned using methods such as oxygen plasma cleaning, or argon plasma, to prevent any undesired oxidations.

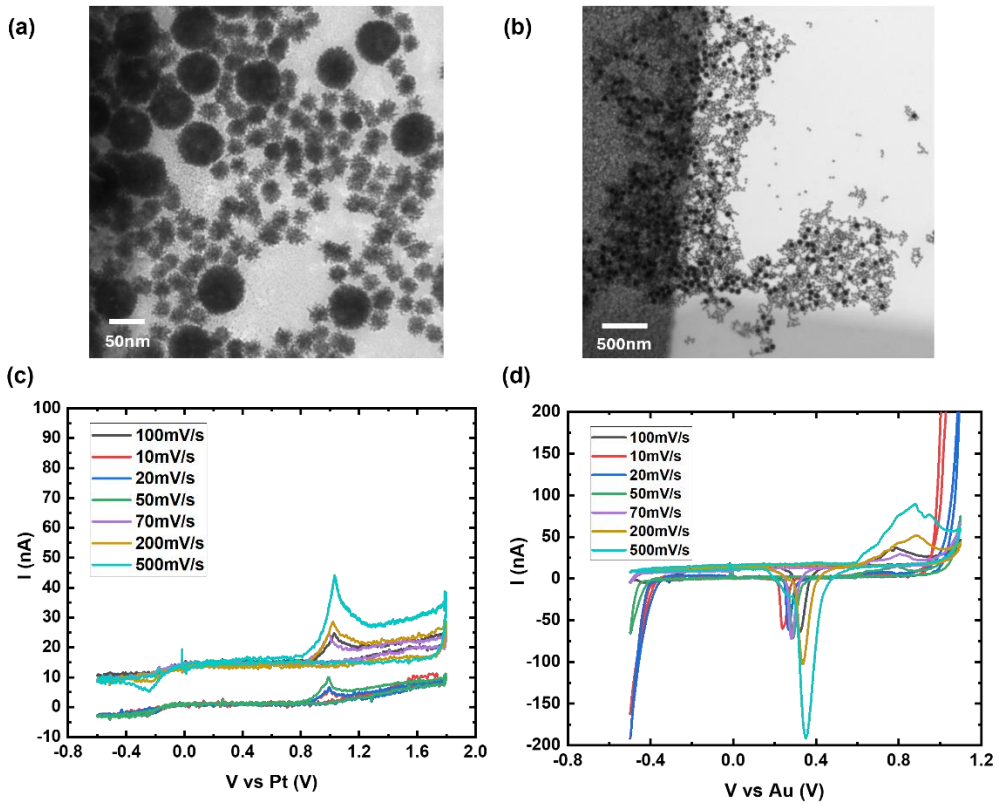

Figure 5-2. Electrochemical cycling of Pt nanoparticles in liquid cell TEM. (a) Bright-field TEM image of bimodal Pt nanoparticles. (b) Bright-field TEM image of Pt nanoparticles placed on the electrode of the liquid cell chip. Cyclic voltammogram of the system when (c) Pt and (d) Au are used as electrode materials.

5.2.2 Addressing the Role of Pulse Duration

Along with the choice of electrode, electrolyte, electrochemical biasing and temperature control, control of the 'temporal' duration of the electrochemical pulses can have significant impact on the electrochemical reactions of materials. In particular, tuning the temporal profile of the electrochemical pulsing applied can tune the product selectivity in electrochemical transformation of CO_2 into fuels and hydrocarbon feedstocks.[198] In particular, developing high-performance catalysts for CO_2 reduction reaction (CO2RR) is gaining more interest. The most desirable products of CO2RR are hydrocarbons and oxygenates containing two or more carbon atoms (C2+, i.e., C_2H_4, C_2H_5OH, C_3H_7OH), as these products can be converted to higher molecular weight products using known catalysts. Among various catalysts investigated for this process, copper (Cu)-containing materials are uniquely capable of producing C2+ products with high faradaic efficiency (FE).[199] However, Cu-based catalysts suffer from poor selectivity since a significant portion of the reduction current is passed to the hydrogen evolution reaction from the aqueous electrolyte.[200]

Recent studies has shown that control of the temporal profile of the electrochemical pulsing can increase the product selectivity of Cu catalysts for CO2RR. This offers opportunities to optimize the system to an unprecedented level. When alternating pulses of reducing 'cathodic' potential and oxidizing 'anodic' potential are applied, the formation of C2+ products is enhanced

compared to the static application of potential (Figure 5-3). Multiple phenomena have been suggested as the factors improving the selectivity, including the repeated reconstruction of the Cu surface, oxidation state, surface adsorbate coverage, local pH, and CO_2 concentration, [201] but foundational questions remain concerning the mechanisms and underlying physicochemical processes. [202] In order to answer these questions, electrochemical liquid cell could be used to probe the structure evolution of Cu as a catalyst for CO2RR during pulsed electrochemical operation.

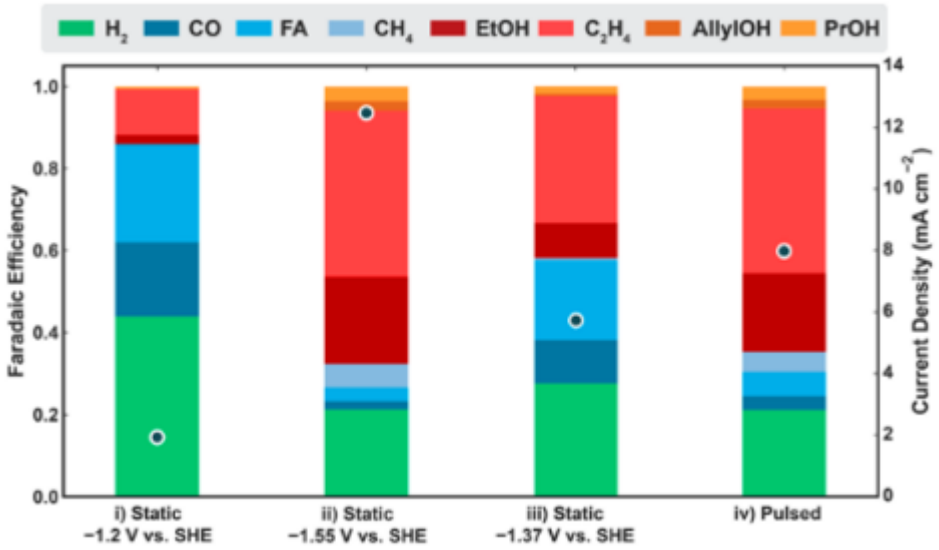

Figure 5-3. Comparison of the product selectivity of Cu catalyst for CO2RR reaction. Figure adpated from [203]

As proof of concept of the applications of liquid cell TEM on characterizing the Cu catalyst dynamics under pulsed electrochemical operation, we performed Cu deposition experiment during the application of a pulsed current. (Figure 5-4) With a constant current, a uniform or dendritic Cu layer would form, depending on the deposition rate.[204] However, in the conditions of Figure 5-4, copper is added and a fraction is removed on each cycle. The still images and

movies captured that the numerous small copper clusters grow but on some cycles the smaller ones dissolve preferentially, and the larger ones grow rapidly to leave one large cluster. Moreover, dendritic features are formed at the tip of the nanoparticles. As atoms dissolve away from catalysts they are redeposited on the same catalyst or elsewhere. If the driving force favors dissolution from the more highly curved surfaces of smaller particles and deposition onto the less curved surfaces of larger particles, the smaller particles will disappear over time. This result clearly shows that depending on the temporal profile and current, pulsed electrochemistry can reduce the surface-to-volume ratio of the particles and related activity - yet pulsing is known to improve selectivity in Cu CO2RR catalysts. With correct design of the electrode geometry, pulse amplitude, duration , and strength can be used as an experimental parameter to probe the fundamentals of Cu nanoparticle evolution during catalytic reaction cycles.

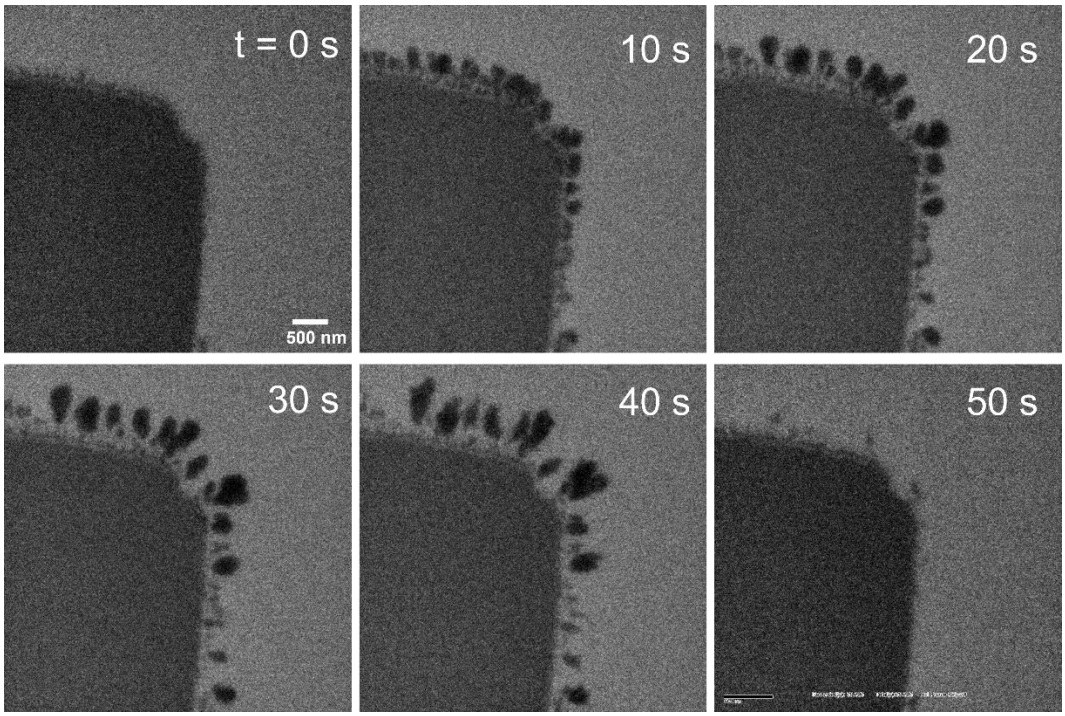

Figure 5-4. Time series of bright field TEM images of Cu deposition on Pt electrode under pulsed current flow. Pulses consisted of -400nA plating current for 0.05 second followed by 1nA stripping current for 0.05 second, repeated 500x.

5.3 Future Directions of *In Situ* Electron Microscopy

In this chapter, the importance of optical stimuli and spectroscopy technique added to the *in situ* electron microscopy is discussed. Optically coupled electron microscopy and spectroscopy data will broaden the understanding of the properties of materials to apply in utilizing solar energy for the sustainable future. Moreover, spectroscopy techniques that can be coupled with ETEM in complex chemical environments is introduced.

5.3.1 Adding Complex External Stimuli: Light

In addition to improving the performance of existing materials for energy conversion and storage, optical properties of nanomaterials can be investigated using *in situ* TEM to open new opportunities to harness the new sustainable energy source, namely, solar energy. In particular, plasmonic nanostructures for efficient photocatalysis are gaining interest as they drive reactions through strong light-matter interactions, and enable the harvesting of solar energy for catalysis, lowering the energy demand for high temperatures or harsh conditions.[205] Therefore, the development of plasmonic photocatalysts with efficient utilization of solar energy is considered as one of the potential approaches in realizing sustainable chemical manufacturing. Moreover, reactions such as photocatalytic CO_2 conversion to useful chemicals are one of the potential approaches to reduce greenhouse gas emissions.[206] However, to meet the energy demand of

large-scale chemical processes, harnessing optical energy via plasmonic photocatalysis has to be improved in its efficiency, stability, and performance. [207]

Optically coupled TEM with high spatial and temporal resolution can visualize catalytic and photocatalytic phase transformations at the nanoscale.[208] These techniques have monitored the interaction between Pd nanocrystals and hydrogen gas in response to light and revealed that plasmons enable new catalytic sites on the nanocrystal surface.[209–211] Real-time optical responses of plasmonic nanostructures can be captured using optically coupled TEM coupled with spectroscopy such as electron energy loss spectroscopy (EELS) for measuring plasmonic performances. The underlying complex mechanisms of photocatalytic reactions remain a challenge, and *in situ* probing of these reactions would contribute to understanding the reaction mechanisms and designing catalysts with high selectivity and efficiency.

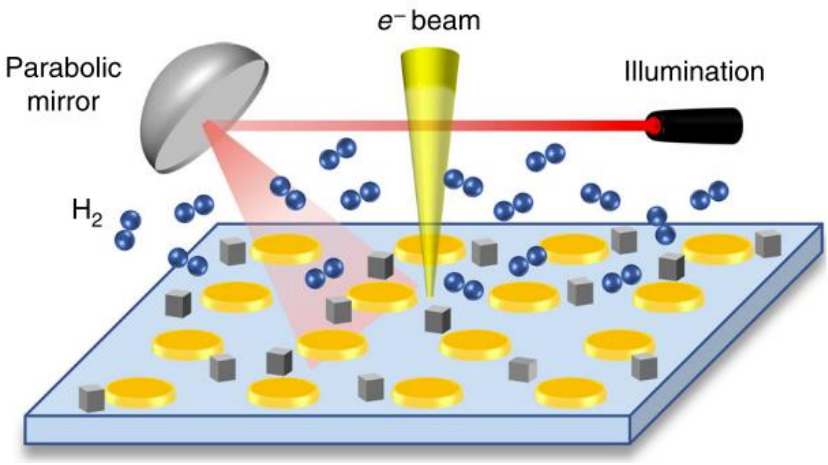

Figure 5-5. Schematic of optically coupled ETEM. Optically coupled ETM enables characterization of plasmon-induced phase transformation in the antenna-reactor configuration. Figure adapted from [212]

5.3.2 Combination with Spectroscopy Techniques

The development in characterization techniques has enabled the investigation of catalyst materials under near-ambient atmospheric pressures couples with temperature control up to 1300 ºC. ETEM and ambient pressure X-ray photoelectron spectroscopy (APXPS) are two examples of those techniques. As previously mentioned, ETEM captures structural and chemical changes under reaction conditions. APXPS has similar pressure limits (5-20 mbar) with ETEM, and recent study[213] has demonstrated the coupling of those techniques. APXPS can compensate the local length scale of ETEM as it enables monitoring of surface species, electronic structure, and oxidation state changes. Moreover, MEMS microheaters can also be adapted for APXPS for temperature controlled experiments. Using the custom designed microheater holder in APXPS experiments, the authors have shown that the chemical reactions of Pd film including CO adsorption-desoprtion, Pd oxidation, and PdO reduction under temperature and pressure conditions identical to those of ETEM instruments with high speed, spectroscopy acquisition (0.5 second per spectrum) and heating to the desired temperature(2 second to reach 500 ºC). The combination of ETEM and APXPS would allow the correlation of multimodal chemical and electronic structure information spanning different length scales. Furthermore, application of the window and gasket adapted from the liquid cell structure could also be applied in APXPS, suggesting the establishment of combination of liquid, gas, temperature control and acquisition of microscopy and spectroscopy data for holistic study of energy materials dynamics.

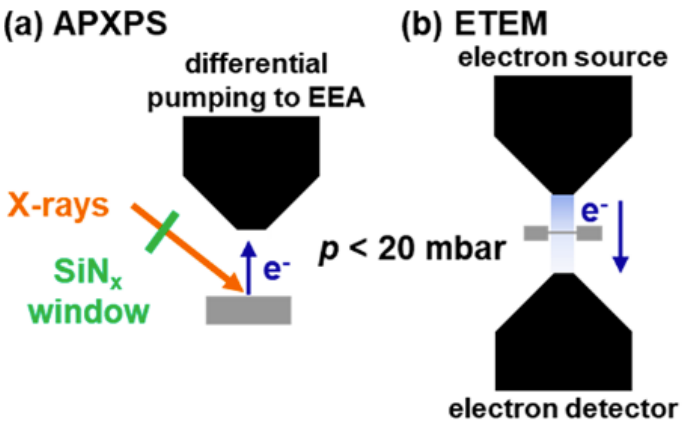

Figure 5-6. Schematic of (a) APXPS and (b) ETEM. Samples are shown to be placed near differential pumping apertures. Figure adapted from [213]

Supplementary Materials

Supplementary Table S1: The reactions describing the radiolysis of aqueous $AgNO_3$ solution.

Reaction #	Equilibria	pK_a (25 °C)	Arrhenius coefficient (A)	Activation energy (E_a, average: 14.93)
1	$H_2O \leftrightarrow H^+ + OH^-$	13.999		
2	$H_2O_2 \leftrightarrow H^+ + HO_2^-$	11.65		
3	$HO_2 \leftrightarrow H^+ + O_2^-$	4.57		
4	$H \leftrightarrow H^+ + e_{aq}^-$	9.77		
	Chemical Reaction	**Rate Constant (25 °C) ($M^{-1}s^{-1}$ unless specified otherwise)**		
5	$H^+ + OH^- \rightarrow H_2O$	1.4×10^{11}	1.88×10^{13}	12.62
6	$H_2O \rightarrow H^+ + OH^-$	$\frac{k_7 \times K_2}{[H_2O]}\ s^{-1}$	1.70×10^{6}	62.37
7	$H_2O_2 \rightarrow H^+ + HO_2^-$	$k_{10} \times K_3\ s^{-1}$	4.12×10^{6}	43.77
8	$H^+ + HO_2^- \rightarrow H_2O_2$	5.0×10^{10}	5.59×10^{12}	11.73
9	$H_2O_2 + OH^- \rightarrow HO_2^- + H_2O$	1.3×10^{10}	3.66×10^{12}	13.98
10	$HO_2^- + H_2O \rightarrow H_2O_2 + OH^-$	$\frac{k_{11} \times K_2}{K_3 \times [H_2O]}$	4.54×10^{11}	31.74
11	$e_{aq}^- + H_2O \rightarrow H + OH^-$	1.9×10^{1}	5.58×10^{6}	31.73
12	$H + OH^- \rightarrow e_{aq}^- + H_2O$	2.2×10^{7}	8.52×10^{13}	37.36
13	$H \rightarrow e_{aq}^- + H^+$	$k_{16} \times K_6\ s^{-1}$	2.84×10^{12}	66.66
14	$e_{aq}^- + H^+ \rightarrow H$	2.3×10^{10}	1.98×10^{12}	11.17
15	$HO_2 \rightarrow O_2^- + H^+$	$k_{22} \times K_5\ s^{-1}$	2.63×10^{8}	14.58
16	$O_2^- + H^+ \rightarrow HO_2$	5.0×10^{10}	5.59×10^{12}	11.73
17	$HO_2 + OH^- \rightarrow O_2^- + H_2O$	5.0×10^{10}	7.13×10^{9}	60.93
18	$O_2^- + H_2O \rightarrow HO_2 + OH^-$	$\frac{k_{23} \times K_2}{K_5 \times [H_2O]}$	3.66×10^{12}	13.98
19	$e_{aq}^- + OH \rightarrow OH^-$	3.0×10^{10}	2.64×10^{12}	10.65
20	$e_{aq}^- + H_2O_2 \rightarrow OH + OH^-$	1.1×10^{10}	7.75×10^{12}	15.72
21	$e_{aq}^- + O_2^- + H_2O \rightarrow HO_2^- + OH^-$	$\frac{1.3 \times 10^{10}}{[H_2O]}\ M^{-2}s^{-1}$	4.43×10^{10}	12.98
22	$e_{aq}^- + HO_2 \rightarrow HO_2^-$	2.0×10^{10}	2.45×10^{12}	12.98
23	$e_{aq}^- + O_2 \rightarrow O_2^-$	1.9×10^{10}	2.53×10^{12}	11.66
24	$e_{aq}^- + e_{aq}^- + 2H_2O \rightarrow H_2 + 2OH^-$	$\frac{5.5 \times 10^{9}}{[H_2O]^2}\ M^{-3}s^{-1}$	1.01×10^{10}	20.74
25	$e_{aq}^- + H + H_2O \rightarrow H_2 + OH^-$	$\frac{2.5 \times 10^{10}}{[H_2O]}\ M^{-2}s^{-1}$	2.06×10^{11}	14.93
26	$H + H_2O \rightarrow H_2 + OH$	1.1×10^{1}	7.39×10^{12}	98.24
27	$H + HO_2^- \rightarrow OH + OH^-$	9.0×10^{7}		
28	$H + H \rightarrow H_2$	7.8×10^{9}	2.69×10^{12}	15.51
29	$H + OH \rightarrow H_2O$	7.0×10^{9}	4.19×10^{11}	9.03
30	$H + H_2O_2 \rightarrow OH + H_2O$	9.0×10^{7}	1.76×10^{11}	21.01
31	$H + O_2 \rightarrow HO_2$	2.1×10^{10}	9.01×10^{11}	10.52
32	$H + HO_2 \rightarrow H_2O_2$	1.8×10^{10}	5.05×10^{12}	15.09
33	$H + O_2^- \rightarrow HO_2^-$	1.8×10^{10}	5.05×10^{12}	15.09
34	$OH + OH \rightarrow H_2O_2$	3.6×10^{9}	9.78×10^{10}	7.48
35	$OH + HO_2 \rightarrow H_2O + O_2$	6.0×10^{9}	1.31×10^{11}	6.68

36	$OH + O_2^- \rightarrow OH^- + O_2$	8.2×10^9	8.75×10^{11}	10.84
37	$OH + H_2 \rightarrow H + H_2O$	4.3×10^7	6.55×10^{10}	18.45
38	$OH + H_2O_2 \rightarrow HO_2 + H_2O$	2.7×10^7	7.72×10^9	13.82
39	$OH + HO_2^- \rightarrow HO_2 + OH^-$	7.5×10^9	1.00×10^{12}	11.92
40	$HO_2 + O_2^- \rightarrow HO_2^- + O_2$	8.0×10^7	2.62×10^9	8.09
41	$HO_2 + HO_2 \rightarrow H_2O_2 + O_2$	7.0×10^5	2.77×10^9	20.07
42	$HO_2 + H_2O_2 \rightarrow OH + O_2 + H_2O$	5.0×10^{-1}		
43	$HO_2 + HO_2^- \rightarrow OH + O_2 + OH^-$	5.0×10^{-1}		
44	$O_2^- + O_2^- + 2H_2O \rightarrow H_2O_2 + O_2 + 2OH^-$	$\frac{1.0 \times 10^2}{[H_2O]^2}\ M^{-3}s^{-1}$		
45	$O_2 + Ag \rightarrow Ag^+ + O_2^-$	5×10^9		
46	$e_{aq}^- + Ag^+ \rightarrow Ag$	3.3×10^{10}		17.8
47	$OH + Ag^+ \rightarrow AgOH^+$	9.7×10^9		
48	$Ag^+ + H \rightarrow Ag + H^+$	2×10^{10}		
49	$NO_3^- + e_{aq}^- \rightarrow NO_3^{2-}$	9.7×10^9		
50	$OH + NO_2^- \rightarrow OH^- + NO_2$	6.0×10^9		
51	$NO_3^{2-} + OH \rightarrow NO_3^- + OH^-$	3.0×10^9		
52	$OH + NO_2 \rightarrow HNO_3$	4.5×10^9		
53	$H + NO_2 \rightarrow HNO_2$	1.0×10^{10}		
54	$H^+ + NO_3^{2-} \rightarrow OH^- + NO_2$	2.0×10^{10}		
55	$HNO_3 \rightarrow NO_3^- + H^+$	1.46×10^{10}		
56	$NO_2 + e_{aq}^- \rightarrow NO_2^-$	1.0×10^{10}		
57	$HNO_2 + OH \rightarrow H_2O + NO_2$	2.0×10^9		

Supplementary Table S2: ΔI values of the plot shown in Figure 3-2.

Pulse	45 ˚C (Red)	45 ˚C (Yellow)	35 ˚C (Purple)	35 ˚C (Green)	25 ˚C (Blue)	25 ˚C (Light Green)
1	22.034	16.695	7.712	7.966	5.763	9.492
2	13.729	16.271	8.644	6.271	5.763	9.153
3	9.153	11.102	7.712	5.424	5.593	7.966
4	5.932	7.034	7.373	6.271	4.153	5.932
5	5.254	4.407	5.508	5.169	4.237	4.407
6	5.085	4.294	5.127	5.593	4.576	4.407
7	3.39	3.503	5.297	3.333	5.254	3.051
8	3.475	2.938	5.085	2.373	4.576	3.729
9	3.136	3.051	4.237	3.164	2.881	3.051
10	3.305	1.78	4.011	3.051	3.051	
11	2.034	1.13	4.181	3.842	2.373	
12	3.475	2.147	3.093	4.576	2.373	
13	2.754	1.653	3.432	3.39	2.486	
14	2.669	1.271	3.559	3.277	3.616	
15	2.458	1.13	2.924	2.415	2.994	
16	1.412	1.102	2.246	2.331		
17	1.751	2.415	2.542	2.119		
18	1.356	1.271	2.203	1.992		
19		1.377	2.486			
20		1.243				

Reference

(1) Mefford, J. T.; Akbashev, A. R.; Kang, M.; Bentley, C. L.; Gent, W. E.; Deng, H. D.; Alsem, D. H.; Yu, Y. S.; Salmon, N. J.; Shapiro, D. A.; Unwin, P. R.; Chueh, W. C. Correlative Operando Microscopy of Oxygen Evolution Electrocatalysts. *Nature* **2021**, *593* (7857), 67–73.

(2) Khan, M. A.; Zhao, H.; Zou, W.; Chen, Z.; Cao, W.; Fang, J. Recent Progresses in Electrocatalysts for Water Electrolysis. *Electrochem. Energy Rev.* **2018**, *1*, 483–530.

(3) Jännsch, Y.; Leung, J. J.; Hämmerle, M.; Magori, E.; Wiesner-Fleischer, K.; Simon, E.; Fleischer, M.; Moos, R. Pulsed Potential Electrochemical CO2 Reduction for Enhanced Stability and Catalyst Reactivation of Copper Electrodes. *Electrochem. Commun.* **2020**, *121*, 106861.

(4) Meier, J. C.; Katsounaros, I.; Galeano, C.; Bongard, H. J.; Topalov, A. A.; Kostka, A.; Karschin, A.; Schüth, F.; Mayrhofer, K. J. J. Stability Investigations of Electrocatalysts on the Nanoscale. *Energy Environ. Sci*. **2012**, *5* (11), 9319–9330.

(5) Holby, E. F.; Shao-Horn, Y.; Sheng, W.; Morgan, D. New Understanding of Pt Surface Area Loss in PEMFC's: Temperature Effects. *ECS Trans.* **2019**, *33* (1), 369–377.

(6) Luo, L.; Nian, Y.; Wang, S.; Dong, Z.; He, Y.; Han, Y.; Wang, C. Real-Time Atomic-Scale Visualization of Reversible Copper Surface Activation during the CO Oxidation Reaction. *Angew. Chem*. **2020**, *132* (6) 2505–2509.

(7) Hwang, S.; Chen, X.; Zhou, G.; Su, D. In Situ Transmission Electron Microscopy on Energy-Related Catalysis. *Adv. Energy. Mater.* **2020**, *10* (11), 1902105.

(8) Fan, Z.; Zhang, L.; Baumann, D.; Mei, L.; Yao, Y.; Duan, X.; Shi, Y.; Huang, J.; Huang, Y.; Duan, X. In Situ Transmission Electron Microscopy for Energy Materials and Devices. *Adv. Mater.* **2019**, *31* (33), 1900608.

(9) Grogan, J. M.; Schneider, N. M.; Ross, F. M.; Bau, H. H. The Nanoaquarium: A New Paradigm in Electron Microscopy. *J. Indian. Inst. Sci.* **2012**, *92* (2), 295–308.

(10) Ross, F. M. Opportunities and Challenges in Liquid Cell Electron Microscopy. *Science* **2015**, *350* (6267), aaa9886.

(11) Williamson, M. J.; Tromp, R. M.; Vereecken, P. M.; Hull, R.; Ross, F. M. Dynamic Microscopy of Nanoscale Cluster Growth at the Solid-Liquid Interface. *Nat. Mater.* **2003**, *2* (8), 532–536.

(12) De Jonge, N.; Ross, F. M. Electron Microscopy of Specimens in Liquid. *Nat. Nanotechnol.* **2011**, *6* (11), 695–704.

(13) Woehl, T. J.; Evans, J. E.; Arslan, I.; Ristenpart, W. D.; Browning, N. D. Direct in Situ Determination of the Mechanisms Controlling Nanoparticle Nucleation and Growth. *ACS Nano* **2012**, *6* (10), 8599–8610.

(14) Jung, W. G.; Park, J. H.; Jo, Y. R.; Kim, B. J. Growth Kinetics of Individual Au Spiky Nanoparticles Using Liquid-Cell Transmission Electron Microscopy. *J. Am. Chem. Soc.* **2019**, *141* (32), 12601–12609.

(15) Gu, M.; Parent, L. R.; Mehdi, B. L.; Unocic, R. R.; McDowell, M. T.; Sacci, R. L.; Xu, W.; Connell, J. G.; Xu, P.; Abellan, P.; Chen, X.; Zhang, Y.; Perea, D. E.; Evans, J. E.; Lauhon, L. J.; Zhang, J. G.; Liu, J.; Browning, N. D.; Cui, Y.; Arslan, I.; Wang, C. M. Demonstration of an Electrochemical Liquid Cell for Operando Transmission Electron Microscopy Observation of the Lithiation/Delithiation Behavior of Si Nanowire Battery Anodes. *Nano Lett.* **2013**, *13* (12), 6106–6112.

(16) Tan, S. F.; Reidy, K.; Klein, J.; Pinkowitz, A.; Wang, B.; Ross, F. M. Real-Time Imaging of Nanoscale Electrochemical Ni Etching under Thermal Conditions. *Chem. Sci.* **2021**, *12* (14), 5259–5268.

(17) Tan, S. F.; Reidy, K.; Lee, S.; Klein, J.; Schneider, N. M.; Lee, H. Y.; Ross, F. M. Multilayer Graphene—A Promising Electrode Material in Liquid Cell Electrochemistry. *Adv. Funct. Mater.* **2021**, *31* (46), 2104628.

(18) Leenheer, A. J.; Jungjohann, K. L.; Zavadil, K. R.; Harris, C. T. Phase Boundary Propagation in Li-Alloying Battery Electrodes Revealed by Liquid-Cell Transmission Electron Microscopy. *ACS Nano* **2016**, *10* (6), 5670–5678.

(19) Sacci, R. L.; Dudney, N. J.; More, K. L.; Parent, L. R.; Arslan, I.; Browning, N. D.; Unocic, R. R. Direct Visualization of Initial SEI Morphology and Growth Kinetics during Lithium Deposition by in Situ Electrochemical Transmission Electron Microscopy. *Chem. Commun.* **2014**, *50* (17), 2104–2107.

(20) Zeng, Z.; Liang, W. I.; Liao, H. G.; Xin, H. L.; Chu, Y. H.; Zheng, H. Visualization of Electrode-Electrolyte Interfaces in LiPF 6/EC/DEC Electrolyte for Lithium Ion Batteries via in Situ TEM. *Nano Lett.* **2014**, *14* (4), 1745–1750.

(21) Mehdi, B. L.; Qian, J.; Nasybulin, E.; Park, C.; Welch, D. A.; Faller, R.; Mehta, H.; Henderson, W. A.; Xu, W.; Wang, C. M.; Evans, J. E.; Liu, J.; Zhang, J. G.; Mueller, K. T.; Browning, N. D. Observation and Quantification of Nanoscale Processes in Lithium Batteries by Operando Electrochemical (S)TEM. *Nano Lett.* **2015**, *15* (3), 2168–2173.

(22) Keskin, S.; Kunnas, P.; De Jonge, N. Liquid-Phase Electron Microscopy with Controllable Liquid Thickness. *Nano Lett.* **2019**, *19* (7), 4608–4613.

(23) Wu, J.; Gao, W.; Yang, H.; Zuo, J. M. Dissolution Kinetics of Oxidative Etching of Cubic and Icosahedral Platinum Nanoparticles Revealed by in Situ Liquid Transmission Electron Microscopy. *ACS Nano* **2017**, *11* (2), 1696–1703.

(24) Hermannsdörfer, J.; De Jonge, N.; Verch, A. Electron Beam Induced Chemistry of Gold Nanoparticles in Saline Solution. *Chem. Commun.* **2015**, *51* (91), 16393–16396.

(25) Korpanty, J.; Parent, L. R.; Gianneschi, N. C. Enhancing and Mitigating Radiolytic Damage to Soft Matter in Aqueous Phase Liquid-Cell Transmission Electron Microscopy in the Presence of Gold Nanoparticle Sensitizers or Isopropanol Scavengers. *Nano Lett.* **2021**, *21* (2), 1141–1149.

(26) Lee, S.; Schneider, N. M.; Tan, S. F.; Ross, F. M. Temperature Dependent Nanochemistry and Growth Kinetics Using Liquid Cell Transmission Electron Microscopy. *ACS Nano* **2023**, *17* (6), 5609–5619.

(27) Zheng, H.; Smith, R. K.; Jun, Y. W.; Kisielowski, C.; Dahmen, U.; Paul Alivisatos, A. Observation of Single Colloidal Platinum Nanocrystal Growth Trajectories. *Science* **2009**, *324* (5932), 1309–1312.

(28) Park, J. H.; Schneider, N. M.; Grogan, J. M.; Reuter, M. C.; Bau, H. H.; Kodambaka, S.; Ross, F. M. Control of Electron Beam-Induced Au Nanocrystal Growth Kinetics through Solution Chemistry. *Nano Lett* **2015**, *15* (8), 5314–5320.

(29) Wang, M.; Park, C.; Woehl, T. J. Quantifying the Nucleation and Growth Kinetics of Electron Beam Nanochemistry with Liquid Cell Scanning Transmission Electron Microscopy. *Chem. Mater.* **2018**, *30* (21), 7727–7736.

(30) Son, Y.; Kim, B. H.; Choi, B. K.; Luo, Z.; Kim, J.; Kim, G.-H.; Park, S.-J.; Hyeon, T.; Mehraeen, S.; Park, J. In Situ Liquid Phase TEM of Nanoparticle Formation and Diffusion in a Phase-Separated Medium. *ACS Appl. Mater. Interfaces* **2022**, *14* (20), 22810-22817.

(31) Liang, W. I.; Zhang, X.; Bustillo, K.; Chiu, C. H.; Wu, W. W.; Xu, J.; Chu, Y. H.; Zheng, H. In Situ Study of Spinel Ferrite Nanocrystal Growth Using Liquid Cell Transmission Electron Microscopy. *Chem. Mater.* **2015**, *27* (23), 8146–8152.

(32) Abellan, P.; Woehl, T. J.; Parent, L. R.; Browning, N. D.; Evans, J. E.; Arslan, I. Factors Influencing Quantitative Liquid (Scanning) Transmission Electron Microscopy. *Chem. Commun.* **2014**, *50* (38), 4873–4880.

(33) Jungjohann, K. L.; Bliznakov, S.; Sutter, P. W.; Stach, E. A.; Sutter, E. A. In Situ Liquid Cell Electron Microscopy of the Solution Growth of Au-Pd Core-Shell Nanostructures. *Nano Lett.* **2013**, *13* (6), 2964–2970.

(34) Alloyeau, D.; Dachraoui, W.; Javed, Y.; Belkahla, H.; Wang, G.; Lecoq, H.; Ammar, S.; Ersen, O.; Wisnet, A.; Gazeau, F.; Ricolleau, C. Unravelling Kinetic and Thermodynamic

Effects on the Growth of Gold Nanoplates by Liquid Transmission Electron Microscopy. *Nano Lett*. **2015**, *15* (4), 2574–2581.

(35) Ahmad, N.; Wang, G.; Nelayah, J.; Ricolleau, C.; Alloyeau, D. Exploring the Formation of Symmetric Gold Nanostars by Liquid-Cell Transmission Electron Microscopy. *Nano Lett.* **2017**, *17* (7), 4194–4201.

(36) Ievlev, A. V.; Jesse, S.; Cochell, T. J.; Unocic, R. R.; Protopopescu, V. A.; Kalinin, S. V. Quantitative Description of Crystal Nucleation and Growth from in Situ Liquid Scanning Transmission Electron Microscopy. *ACS Nano* **2015**, *9* (12), 11784–11791.

(37) Ou, Z.; Wang, Z.; Luo, B.; Luijten, E.; Chen, Q. Kinetic Pathways of Crystallization at the Nanoscale. *Nat. Mater.* **2020**, *19* (4), 450–455.

(38) Sutter, P.; Tkachenko, A. V; Krahne, R.; Graaf, J. De; Arciniegas, M.; Sutter, E.; Manna, L. In situ Microscopy of the Self-Assembly of Branched Nanocrystals in Solution. *Nat. Commun.* **2016**, *7* (1), 11213.

(39) Park, J.; Zheng, H.; Lee, W. C.; Geissler, P. L.; Rabani, E.; Alivisatos, A. P. Direct Observation of Nanoparticle Superlattice Formation by Using Liquid Cell Transmission Electron Microscopy. *ACS Nano* **2012**, *6* (3), 2078–2085.

(40) Tan, S. F.; Chee, S. W.; Baraissov, Z.; Jin, H.; Tan, T. L.; Mirsaidov, U. Intermediate Structures of Pt-Ni Nanoparticles during Selective Chemical and Electrochemical Etching. *J. Phys. Chem. Lett.* **2019**, *10* (20), 6090–6096.

(41) Wu, F.; Yao, N. Advances in Sealed Liquid Cells for In-Situ TEM Electrochemial Investigation of Lithium-Ion Battery. *Nano Energy* **2015**, *11*, 196–210.

(42) Impagnatiello, A.; Cerqueira, C. F.; Coulon, P. E.; Morin, A.; Escribano, S.; Guetaz, L.; Clochard, M. C.; Rizza, G. Degradation Mechanisms of Supported Pt Nanocatalysts in Proton Exchange Membrane Fuel Cells: An Operando Study through Liquid Cell Transmission Electron Microscopy. *ACS Appl. Energy. Mater.* **2020**, *3* (3), 2360–2371.

(43) Jinschek, J. R. Advances in the Environmental Transmission Electron Microscope (ETEM) for Nanoscale in Situ Studies of Gas-Solid Interactions. *Chem. Commun.* **2014**, *50* (21), 2696–2706.

(44) Gai, P. L.; Sharma. R.; Ross. F. M. "Environmental (S) TEM studies of gas–liquid–solid interactions under reaction conditions." *MRS bulletin* **2008**, *33* (2), *107–114*.

(45) Panciera, F.; Chou, Y. C.; Reuter, M. C.; Zakharov, D.; Stach, E. A.; Hofmann, S.; Ross, F. M. Synthesis of Nanostructures in Nanowires Using Sequential Catalyst Reactions. *Nat. Mater.* **2015**, *14* (8), 820–825.

(46) Yang, J. C.; Small, M. W.; Grieshaber, R. V.; Nuzzo, R. G. Recent Developments and Applications of Electron Microscopy to Heterogeneous Catalysis. *Chem. Soc. Rev.* **2012**, *41* (24), 8179–8194.

(47) Hansen, T. W.; Wagner, J. B. Catalysts under Controlled Atmospheres in the Transmission Electron Microscope. *ACS Catal*. **2014**, *4* (6) 1673–1685.

(48) Gai, P. L.; Boyes, E. D.; Helveg, S.; Hansen, P. L.; Giorgio, S.; Henry, C. R. Atomic-Resolution Environmental Transmission Electron Microscopy for Probing Gas-Solid Reactions in Heterogeneous Catalysis. *MRS bulletin* **2007**, *32* (12), 1044–105.

(49) Tang, M.; Yuan, W.; Ou, Y.; Li, G.; You, R.; Li, S.; Yang, H.; Zhang, Z.; Wang, Y. Recent Progresses on Structural Reconstruction of Nanosized Metal Catalysts via Controlled-Atmosphere Transmission Electron Microscopy: A Review. *ACS Catal.* **2020**, *10* (24), 14419–14450.

(50) Hansen, T. W.; Delariva, A. T.; Challa, S. R.; Datye, A. K. Sintering of Catalytic Nanoparticles: Particle Migration or Ostwald Ripening? *Acc. Chem. Res.* **2013**, *46* (8), 1720–1730.

(51) Tieu, P.; Zang, W.; Lee, J.; Yan, X.; Christopher, P.; Tieu, P.; Zang, W.; Lee, J.; Yan, X.; Christopher, P.; Pan, X. Atomistic Understanding of CO and H2 Influence on Pt Sintering in Pt/CeO2. *Microsc. Microanal*. **2023**, *29* (1), 1573–1574.

(52) Dietze, E. M.; Abild-Pedersen, F.; Plessow, P. N. Comparison of Sintering by Particle Migration and Ripening through First-Principles-Based Simulations. *J. Phys. Chem. C* **2018**, *122* (46), 26563–26569.

(53) Datye, A. K.; Xu, Q.; Kharas, K. C.; Mccarty, J. M. Particle Size Distributions in Heterogeneous Catalysts : What Do They Tell Us about the Sintering Mechanism? *Catal. Today* **2006**, *111* (1-2), 59–67.

(54) Cherevko, S.; Kulyk, N.; Mayrhofer, K. J. J. Durability of Platinum-Based Fuel Cell Electrocatalysts: Dissolution of Bulk and Nanoscale Platinum. *Nano Energy* **2016**, *29*, 275–298.

(55) Jiang, Y.; Li, H.; Wu, Z.; Ye, W.; Zhang, H.; Wang, Y.; Sun, C. In Situ Observation of Hydrogen-Induced Surface Faceting for Palladium – Copper Nanocrystals at Atmospheric Pressure. *Angew. Chem., Int. Ed.* **2016**, *55* (40), 12427–12430.

(56) Fujiwara, K.; Okuyama, K.; Pratsinis, S. E. Metal-Support Interactions in Catalysts for Environmental Remediation. *Environ Sci Nano* **2017**, *4* (11), 2076–2092.

(57) Tang, H.; Su, Y.; Guo, Y.; Zhang, L.; Li, T.; Zang, K.; Liu, F.; Li, L.; Luo, J.; Qiao, B.; Wang, J. Oxidative Strong Metal-Support Interactions (OMSI) of Supported Platinum-Group Metal Catalysts. *Chem. Sci.* **2018**, *9* (32), 6679–6684.

(58) Kuwauchi, Y.; Yoshida, H.; Akita, T.; Haruta, M.; Takeda, S. Intrinsic Catalytic Structure of Gold Nanoparticles Supported on TiO2. *Angew. Chem., Int. Ed*. **2012**, *51* (31), 7729–7733.

(59) Woehl, T. J. Metal Nanocrystal Formation during Liquid Phase Transmission Electron Microscopy: Thermodynamics and Kinetics of Precursor Conversion, Nucleation, and Growth. *Chem. Mater*. **2020**, *32* (18) ,7569**–**7581.

(60) Zheng, H.; Smith, R. K.; Jun, Y. W.; Kisielowski, C.; Dahmen, U.; Paul Alivisatos, A. Observation of Single Colloidal Platinum Nanocrystal Growth Trajectories. *Science* **2009**, *324* (5932), 1309–1312.

(61) Jungjohann, K. L.; Bliznakov, S.; Sutter, P. W.; Stach, E. A.; Sutter, E. A. In Situ Liquid Cell Electron Microscopy of the Solution Growth of Au-Pd Core-Shell Nanostructures. *Nano Lett.* **2013**, *13* (6), 2964–2970.

(62) Khelfa, A.; Nelayah, J.; Amara, H.; Wang, G.; Ricolleau, C.; Alloyeau, D. Quantitative In Situ Visualization of Thermal Effects on the Formation of Gold Nanocrystals in Solution. *Adv. Mater.* **2021**, *33* (38), 2102514.

(63) Ambrožič, B.; Prašnikar, A.; Hodnik, N.; Kostevšek, N.; Likozar, B.; Rožman, K. Ž.; Šturm, S. Controlling the Radical-Induced Redox Chemistry inside a Liquid-Cell TEM. *Chem. Sci.* **2019**, *10* (38), 8735–8743.

(64) Ross, F. M. *Liquid Cell Electron Microscopy*; Cambridge University Press, 2017.

(65) White, E. R.; Mecklenburg, M.; Singer, S. B.; Aloni, S.; Regan, B. C. Imaging Nanobubbles in Water with Scanning Transmission Electron Microscopy. *Appl. Phys. Express* **2011**, *4* (5), 55201.

(66) Xin, H. L.; Zheng, H. In Situ Observation of Oscillatory Growth of Bismuth Nanoparticles. *Nano Lett.* **2012**, *12* (3), 1470–1474.

(67) Niu, K.-Y.; Park, J.; Zheng, H.; Alivisatos, A. P. Revealing Bismuth Oxide Hollow Nanoparticle Formation by the Kirkendall Effect. *Nano Lett.* **2013**, *13* (11), 5715–5719.

(68) Liu, Y.; Tai, K.; Dillon, S. J. Growth Kinetics and Morphological Evolution of ZnO Precipitated from Solution. *Chem. Mater.* **2013**, *25* (15), 2927–2933.

(69) Ma, S.; Jiang, M.; Tao, P.; Song, C.; Wu, J.; Wang, J.; Deng, T.; Shang, W. Temperature Effect and Thermal Impact in Lithium-Ion Batteries: A Review. *Prog. Nat. Sci.: Mater. Int.* **2018**, *28* (6), 653–666.

(70) Khanna, A. S. *High Temperature Corrosion*; World Scientific, 2016.

(71) Chee, S. W.; Tan, S. F.; Baraissov, Z.; Bosman, M.; Mirsaidov, U. Direct Observation of the Nanoscale Kirkendall Effect during Galvanic Replacement Reactions. *Nat. Commun.* **2017**, *8* (1), 1224.

(72) Millstone, J.E.; Hurst, S.J.; Métraux, G.S.; Cutler, J.I.; Mirkin, C.A. Colloidal Gold and Silver Triangular Nanoprisms. *Small*, **2009**, *5* (6), 646–664.

(73) Dong, H.; Chen, Y.; Feldmann, C. Polyol Synthesis of Nanoparticles: Status and Options Regarding Metals, Oxides, Chalcogenides, and Non-Metal Elements. *Green Chem*. **2015**, *17* (8), 4107–4132.

(74) Hauwiller, M. R.; Ondry, J. C.; Chan, C. M.; Khandekar, P.; Yu, J.; Alivisatos, A. P. Gold Nanocrystal Etching as a Means of Probing the Dynamic Chemical Environment in Graphene Liquid Cell Electron Microscopy. *J. Am. Chem. Soc.* **2019**, *141* (10), 4428–4437.

(75) Schneider, N. M.; Norton, M. M.; Mendel, B. J.; Grogan, J. M.; Ross, F. M.; Bau, H. H. Electron-Water Interactions and Implications for Liquid Cell Electron Microscopy. *J. Phys. Chem. C* **2014**, *118* (38), 22373–22382.

(76) Fritsch, B.; Zech, T. S.; Bruns, M. P.; Körner, A.; Khadivianazar, S.; Wu, M.; Zargar Talebi, N.; Virtanen, S.; Unruh, T.; Jank, M. P. M.; Spiecker, E.; Hutzler, A. Radiolysis-Driven Evolution of Gold Nanostructures – Model Verification by Scale Bridging In Situ Liquid-Phase Transmission Electron Microscopy and X-Ray Diffraction. *Adv. Sci.* **2022**, *2* (1), 2202803.

(77) Hauwiller, M. R.; Zhang, X.; Liang, W. I.; Chiu, C. H.; Zhang, Q.; Zheng, W.; Ophus, C.; Chan, E. M.; Czarnik, C.; Pan, M.; Ross, F. M.; Wu, W. W.; Chu, Y. H.; Asta, M.; Voorhees, P. W.; Alivisatos, A. P.; Zheng, H. Dynamics of Nanoscale Dendrite Formation in Solution Growth Revealed Through in Situ Liquid Cell Electron Microscopy. *Nano Lett.* **2018**, *18* (10), 6427–6433.

(78) White, E. R.; Singer, S. B.; Augustyn, V.; Hubbard, W. A.; Mecklenburg, M.; Dunn, B.; Regan, B. C. In Situ Transmission Electron Microscopy of Lead Dendrites and Lead Ions in Aqueous Solution. *ACS Nano* **2012**, *6* (7), 6308–6317.

(79) Abbaschian, R.; Reed-Hill, R. E. *Physical Metallurgy Principles-SI Version*; Cengage Learning, 2009.

(80) Liu, W.; Liu, P.; Mitlin, D. Tutorial Review on Structure-Dendrite Growth Relations in Metal Battery Anode Supports. *Chem. Soc. Rev.* **2020**, *49* (20), 7284–7300.

(81) NIST Database.

(82) Horne, G. P.; Donoclift, T. A.; Sims, H. E.; Orr, R. M.; Pimblott, S. M. Multi-Scale Modeling of the Gamma Radiolysis of Nitrate Solutions. *J. Phys. Chem. B* **2016**, *120* (45), 11781–11789.

(83) Woehl, T. J.; Abellan, P. Defining the Radiation Chemistry during Liquid Cell Electron Microscopy to Enable Visualization of Nanomaterial Growth and Degradation Dynamics. *J. Microsc.* **2017**, *265* (2), 135–147.

(84) Tan, S. F.; Bisht, G.; Anand, U.; Bosman, M.; Yong, X. E.; Mirsaidov, U. In Situ Kinetic and Thermodynamic Growth Control of Au-Pd Core-Shell Nanoparticles. *J. Am. Chem. Soc.* **2018**, *140* (37), 11680–1168517.

(85) Xia, Y.; Xia, X.; Peng, H. C. Shape-Controlled Synthesis of Colloidal Metal Nanocrystals: Thermodynamic versus Kinetic Products. *J. Am. Chem. Soc.* **2015**, *137* (25), 7947–7966.

(86) Wu, J.; Gao, W.; Wen, J.; Miller, D. J.; Lu, P.; Zuo, J. M.; Yang, H. Growth of Au on Pt Icosahedral Nanoparticles Revealed by Low-Dose in Situ TEM. *Nano Lett.* **2015**, *15* (4), 2711–2715.

(87) Wook, K.; Liu, Y.; Sun, L.; Dillon, S. J. Ultramicroscopy Challenges Associated with In-Situ TEM in Environmental Systems: The Case of Silver in Aqueous Solutions. *Ultramicroscopy* **2012**, *116*, 34–38.

(88) Ahn, T. Y.; Hong, S. P.; Kim, S. Il; Kim, Y. W. In Situ Liquid-Cell Transmission Electron Microscopy for Direct Observation of Concentration-Dependent Growth and Dissolution of Silver Nanoparticles. *RSC Adv.* **2015**, *5* (100), 82342–82345.

(89) Tombs, M. C.; Crittenden, J.C; Trussell, R.R; Hand, D.W.; Howe, K. J.; Tchobanoglous, G. MWH Water Treatment Principles and Design. Third Edition. *Chromatographia* **2014**, *77* (5), 527–528.

(90) Radisic, A.; Ross, F. M.; Searson, P. C. In Situ Study of the Growth Kinetics of Individual Island Electrodeposition of Copper. *J. Phys. Chem. B* **2006**, *110* (15), 7862–7868.

(91) Hutzler, A.; Fritsch, B.; Jank, M. P. M.; Branscheid, R.; Martens, R. C.; Spiecker, E.; März, M. In Situ Liquid Cell TEM Studies on Etching and Growth Mechanisms of Gold Nanoparticles at a Solid–Liquid–Gas Interface. *Adv. Mater. Interfaces.* **2019**, *6* (20). 1901027.

(92) Woehl, T. J.; Prozorov, T. The Mechanisms for Nanoparticle Surface Diffusion and Chain Self-Assembly Determined from Real-Time Nanoscale Kinetics in Liquid. *J. Phys. Chem. C* **2015**, *119* (36), 21261–21269.

(93) Verch, A.; Pfaff, M.; De Jonge, N. Exceptionally Slow Movement of Gold Nanoparticles at a Solid/Liquid Interface Investigated by Scanning Transmission Electron Microscopy. *Langmuir* **2015**, *31* (25), 6956–6964.

(94) Harned, H. S.; Hildreth Jr, C. L. The Diffusion Coefficient of Silver Nitrate in Dilute Aqueous Solution at 25. *J. Am. Chem. Soc.* **1951**, *73* (7), 3292–3293.

(95) Jamnig, A.; Sangiovanni, D. G.; Abadias, G.; Sarakinos, K. Atomic-Scale Diffusion Rates during Growth of Thin Metal Films on Weakly-Interacting Substrates. *Sci. Rep*. **2019**, *9* (1), 6640.

(96) Murph, S. E. H.; Murphy, C. J.; Leach, A.; Gall, K. A Possible Oriented Attachment Growth Mechanism for Silver Nanowire Formation. Cryst. Growth Des. **2015**, *15* (4), 1968–1974.

(97) Rodrigues, T. S.; Zhao, M.; Yang, T.; Gilroy, K. D. Synthesis of Colloidal Metal Nanocrystals: A Comprehensive Review on the Reductants. *Chem. - Eur. J.* **2018**,*24* (64), 16944–16963.

(98) Komanicky, V.; Lddir, H.; Chang, K. C.; Menzel, A.; Karapetrov, G.; Hennessy, D.; Zapol, P.; You, H. Shape-Dependent Activity of Platinum Array Catalyst. *J. Am. Chem. Soc.* **2009**, *131* (16), 5732–5733.

(99) Kang, S. W.; Lee, Y. W.; Park, Y.; Choi, B.; Hong, J. W.; Park, K. One-Pot Synthesis of Trimetallic Au @ PdPt Core À Shell Nanoparticles with High Catalytic Performance. *ACS Nano* **2013**, *7* (9), 7945–7955.

(100) Tan, S. F.; Wu, L.; Yang, J. K. W.; Bai, P.; Bosman, M.; Nijhuis,C. A. Quantum Plasmon Resonances Controlled by Molecular Tunnel Junctions. *Science* **2014**, *343* (6178), 1496−1499.

(101) Nguyen, K. T.; Zhao, Y. Integrated Graphene/Nanoparticle Hybrids for Biological and Electronic Applications. *Nanoscale* **2014**, *6* (12), 6245–6266.

(102) Zubkov, M. A.; Kogan, S. M.; Levitov, L. S.; Spivak, B. Z.; Dzero, M.; Axt, V. M.; Kuhn, T.; Eckstein, M.; Werner, P.; Varma, C. M.; Klein, M. V; Varma, C. M.; Hoffmann, M. C.; Bartal, B.; Nelson, K. A.; Kampfrath, T.; Tanaka, K.; Nelson, K. A.; Shimano, R.; Watanabe, S.; Matsunaga, R.; Terai, H.; Takeda, M.; Uzawa, Y.; Wang, Z.; Aoki, H.; Uzawa, Y.; Wang, Z.; Goldman, A. M. Self-Assembly of Magnetite Nanocubes into Helical Superstructures. Science **2014**, *345* (6201), 1149–1153.

(103) Sheikholeslami, S. N.; Dionne, J. A. Controlling the Interplay of Electric and Magnetic Modes via Fano-like Plasmon Resonances. *Nano Lett*. **2011**, *11* (9), 3927–3934.

(104) Scholl, J. A.; Garc, A.; Koh, A. L.; Dionne, J. A. Observation of Quantum Tunneling between Two Plasmonic Nanoparticles. *Nano Lett*. **2013**, *13* (2), 564–569.

(105) Scholl, J. A.; Koh, A. L.; Dionne, J. A. Quantum Plasmon Resonances of Individual Metallic Nanoparticles. *Nature* **2012**, *483* (7390), 421–427.

(106) Lu, X.; Rycenga, M.; Skrabalak, S. E.; Wiley, B.; Xia, Y. Chemical Synthesis of Novel Plasmonic Nanoparticles. *Annu. Rev. Phys. Chem*. **2009**, *60*, 167–192.

(107) Wang, M.; Park, C.; Woehl, T. J. Quantifying the Nucleation and Growth Kinetics of Electron Beam Nanochemistry with Liquid Cell Scanning Transmission Electron Microscopy. *Chem. Mater.* **2018**, *30* (21), 7727–7736.

(108) Watt, J.; Cheong, S.; Toney, M. F.; Ingham, B.; Cookson, J.; Bishop, P. T.; Tilley, R. D. Ultrafast Growth of Highly Branched Palladium Nanostructures for Catalysis. *ACS Nano* **2010**, *4* (1), 396–402.

(109) Huang, W.; Johnston-Peck, A. C.; Wolter, T.; Yang, W. C. D.; Xu, L.; Oh, J.; Reeves, B. A.; Zhou, C.; Holtz, M. E.; Herzing, A. A.; Lindenberg, A. M.; Mavrikakis, M.; Cargnello, M. Steam-Created Grain Boundaries for Methane C–H Activation in Palladium Catalysts. *Science* **2021**, *373* (6562), 1518−1523.

(110) Oh, J.; Boucly, A.; van Bokhoven, J. A.; Artiglia, L.; Cargnello, M. Palladium Catalysts for Methane Oxidation: Old Materials, New Challenges. *Acc. Chem. Res.* **2023**, *57* (1), 23−36.

(111) Oh, J.; Beck, A.; Goodman, E. D.; Roling, L. T.; Boucly, A.; Artiglia, L.; Abild-Pedersen, F.; van Bokhoven, J. A.; Cargnello, M. Colloidally Engineered Pd and Pt Catalysts Distinguish Surface- and Vapor-Mediated Deactivation Mechanisms. *ACS Catal.* **2023**, *13* (3), 1812–1822.

(112) Xie, X.; Gao, G.; Pan, Z.; Wang, T.; Meng, X.; Cai, L. Large-Scale Synthesis of Palladium Concave Nanocubes with High-Index Facets for Sustainable Enhanced Catalytic Performance. *Sci. Rep.* **2015**, *5* (1), 8515.

(113) Collins, G.; Schmidt, M.; O'Dwyer, C.; McGlacken, G.; Holmes, J. D. Enhanced Catalytic Activity of High-Index Faceted Palladium Nanoparticles in Suzuki–Miyaura Coupling Due to Efficient Leaching Mechanism. *ACS Catal.* **2014**, *4* (9), 3105–3111.

(114) Liu, M.; Zhou, S.; Choi, S.-I.; Xia, Y. Deterministic Synthesis of Pd Nanocrystals Enclosed by High-Index Facets and Their Enhanced Activity toward Formic Acid Oxidation. *Precis. Chem.* **2023**, *1* (6), 372–381.

(115) Jin, M.; Zhang, H.; Xie, Z.; Xia, Y. Palladium Nanocrystals Enclosed by {100} and {111} Facets in Controlled Proportions and Their Catalytic Activities for Formic Acid Oxidation. *Energy Environ. Sci.* **2012**, *5* (4), 6352–6357.

(116) Jin, B.; Liu, Z.; Tang, R.; Jin, C. Quantitative Investigation of the Formation and Growth of Palladium Fractal Nanocrystals by Liquid-Cell Transmission Electron Microscopy. *Chem. Commun.* **2019**, *55* (56), 8186–8189.

(117) Kettemann, F.; Wuithschick, M.; Caputo, G.; Kraehnert, R.; Pinna, N.; Rademann, K.; Polte, J. Reliable Palladium Nanoparticle Syntheses in Aqueous Solution: The Importance of Understanding Precursor Chemistry and Growth Mechanism. *CrystEngComm* **2015**, *17* (8), 1865–1870.

(118) Ikeda, S.; Ishino, S.; Harada, T.; Okamoto, N.; Sakata, T.; Mori, H.; Kuwabata, S.; Torimoto, T.; Matsumura, M. Ligand-Free Platinum Nanoparticles Encapsulated in a Hollow Porous Carbon Shell as a Highly Active Heterogeneous Hydrogenation Catalyst. *Angew. Chem.* **2006**, *118* (42), 7221–7224.

(119) Niu, Z.; Li, Y. Removal and Utilization of Capping Agents in Nanocatalysis. *Chem. Mater*. **2014**, *26* (1), 72−83.

(120) Naresh, N.; Wasim, F. G. S.; Ladewig, B. P.; Neergat, M. Removal of Surfactant and Capping Agent from Pd Nanocubes (Pd-NCs) Using Tert-Butylamine: Its Effect on Electrochemical Characteristics. *J. Mater. Chem. A* **2013**, *1* (30), 8553–8559.

(121) Dachraoui, W.; Erni, R. Nonclassical Nucleation and Growth of Pd Nanocrystals from Aqueous Solution Studied by In Situ Liquid Transmission Electron Microscopy. *Chem. Mater.* **2023**, *35* (3), 1201–1208.

(122) Fan, F. R.; Attia, A.; Sur, U. K.; Chen, J. Bin; Xie, Z. X.; Li, J. F.; Bin, R.; Tian, Z. Q. An Effective Strategy for Room-Temperature Synthesis of Single-Crystalline Palladium Nanocubes and Nanodendrites in Aqueous Solution. *Cryst. Growth Des.* **2009**, *9* (5), 2335–2340.

(123) Sau, T. K.; Murphy, C. J. Room Temperature, High-Yield Synthesis of Multiple Shapes of Gold Nanoparticles in Aqueous Solution. *J. Am. Chem. Soc.* **2004**, *126* (28), 8648–8649.

(124) López-Miranda, A.; López-Valdivieso, A.; Viramontes-Gamboa, G. Silver Nanoparticles Synthesis in Aqueous Solutions Using Sulfite as Reducing Agent and Sodium Dodecyl Sulfate as Stabilizer. *J. Nanopart. Res.* **2012**, *14* (9), 1−11.

(125) Xu, L.; Henkelman, G.; Campbell, C. T.; Jónsson, H. Small Pd Clusters, up to the Tetramer at Least, Are Highly Mobile on the MgO(100) Surface. *Phys. Rev. Lett.* **2005**, *95* (14), 146103.

(126) Radisic, A.; Vereecken, P. M.; Hannon, J. B.; Searson, P. C.; Ross, F. M. Quantifying Electrochemical Nucleation and Growth of Nanoscale Clusters Using Real-Time Kinetic Data. *Nano Lett.* **2006**, *6* (2), 238–242.

(127) Abel, B.; Buck, U.; Sobolewski, A. L.; Domcke, W. On the Nature and Signatures of the Solvated Electron in Water. *Phys. Chem. Chem. Phys*. **2012**, *14* (1), 22–34.

(128) Liao, H. G.; Niu, K.; Zheng, H. Observation of Growth of Metal Nanoparticles. *Chem. Commun.* **2013**, *49* (100), 11720–11727.

(129) Čubová, K.; Čuba, V. Synthesis of Inorganic Nanoparticles by Ionizing Radiation–a Review. *Radiat. Phys. Chem.* **2020**, *169*, 108774.

(130) Park, J. H.; Steingart, D. A.; Kodambaka, S.; Ross, F. M. Electrochemical Electron Beam Lithography: Write, Read, and Erase Metallic Nanocrystals on Demand. *Sci. Adv.* **2017**, *3* (7), e1700234.

(131) Yang, J.; Prabhudev, S.; Soleymani, L.; Andrei, C. M.; Botton, A. Deposition and Morphological Evolution of Nanostructured Palladium during Potential Cycling: A Liquid-Cell TEM Study. *Chem. Commun*. **2019**, *55* (62), 9204–9207.

(132) Zhu, G. Z.; Prabhudev, S.; Yang, J.; Gabardo, C. M.; Botton, G. A.; Soleymani, L. In Situ Liquid Cell TEM Study of Morphological Evolution and Degradation of Pt-Fe Nanocatalysts during Potential Cycling. *J. Phys. Chem. C* **2014**, *118* (38), 22111–22119..

(133) White, E. R.; Singer, S. B.; Augustyn, V.; Hubbard, W. A.; Mecklenburg, M.; Dunn, B.; Regan, B. C. In Situ Transmission Electron Microscopy of Lead Dendrites and Lead Ions in Aqueous Solution. *ACS Nano* **2012**, *6* (7), 6308–6317.

(134) Beermann, V.; Holtz, M. E.; Padgett, E.; De Araujo, J. F.; Muller, D. A.; Strasser, P. Real-Time Imaging of Activation and Degradation of Carbon Supported Octahedral Pt-Ni Alloy Fuel Cell Catalysts at the Nanoscale Using: In Situ Electrochemical Liquid Cell STEM. *Energy Environ Sci* **2019**, *12* (8), 2476–2485.

(135) Leng, F.; Tan, C. M.; Pecht, M. Effect of Temperature on the Aging Rate of Li Ion Battery Operating above Room Temperature. *Sci. Rep.* **2015**, *5* (1), 12967.

(136) Shan, Y.; Choe, S. Y. A High Dynamic PEM Fuel Cell Model with Temperature Effects. *J. Power Sources* **2005**, *145* (1), 30–39.

(137) Nurlaela, E.; Shinagawa, T.; Qureshi, M.; Dhawale, D. S.; Takanabe, K. Temperature Dependence of Electrocatalytic and Photocatalytic Oxygen Evolution Reaction Rates Using NiFe Oxide. *ACS Catal.* **2016**, *6* (3), 1713–1722.

(138) Govind Rajan, A.; Martirez, J. M. P.; Carter, E. A. Coupled Effects of Temperature, Pressure, and PH on Water Oxidation Thermodynamics and Kinetics. *ACS Catal.* **2021**, *11* (18), 11305–11319

(139) Czioska, S.; Ehelebe, K.; Geppert, J.; Escalera-López, D.; Boubnov, A.; Saraçi, E.; Mayerhöfer, B.; Krewer, U.; Cherevko, S.; Grunwaldt, J. D. Heating up the OER: Investigation of IrO2 OER Catalysts as Function of Potential and Temperature. *ChemElectroChem* **2022**, *9* (19), *202200514*.

(140) Conway, B. E.; Wilkinson, D. P. Non-Isothermal Cell Potentials and Evaluation of Entropies of Ions and of Activation for Single Electrode Processes in Non-Aqueous Media. *Electrochim. Acta* **1993**, *38* (7), 997–1013.

(141) Forryan, C. L.; Compton, R. G. Studies of the Electrochemical Reduction of 4-Nitrophenol in Dimethylformamide: Evidence for a Change in Mechanism with Temperature. *Phys. Chem. Chem. Phys.* **2003**, *5* (19), 4226–4230.

(142) Yi, T. F.; Yang, S. Y.; Ma, H. T.; Li, X. Y.; Ma, Y. Q.; Qiao, H. Bin; Zhu, R. S. Effect of Temperature on Lithium-Ion Intercalation Kinetics of LiMn1.5Ni0.5O4-Positive-Electrode Material. *Ionics* **2014**, *20* (3), 309–314.

(143) Wildgoose, G. G.; Giovanelli, D.; Lawrence, N. S.; Compton, R. G. High-Temperature Electrochemistry: A Review. *Electroanalysis* **2004**, *16* (6), 421–433.

(144) Giovanelli, D.; Lawrence, N. S.; Klymenko, O. V; Jiang, L.; Jones, T. G. J.; Compton, R. G. The Electrochemically Initiated Reaction of Sulfide with N, N-Diethyl-p-phenylenediamine in Dimethylformamide. Part II: Implications for Sensing Strategies. *Electroanalysis* **2003**, *15* (11), 961–968.

(145) Klymenko, O. V; Giovanelli, D.; Lawrence, N. S.; Rees, N. V; Jiang, L.; Jones, T. G. J.; Compton, R. G. The Electrochemical Oxidation of N, N-Diethyl-p-Phenylenediamine in DMF and Analytical Applications. Part I: Mechanistic Study. *Electroanalysi* **2003**, *15* (11), 949–960.

(146) Flechsig, G.; Korbut, O.; Gründler, P. Investigation of Deposition and Stripping Phenomena at the Heated Gold Wire Electrode in Comparison to the Rotating Disk Electrode: Copper (II), Mercury (II), and Arsenic (III). *Electroanalysis* **2001**, *13* (8-9), 786–788.

(147) Tsai, Y.; Coles, B. A.; Holt, K.; Foord, J. S.; Marken, F.; Compton, R. G. Microwave-Enhanced Anodic Stripping Detection of Lead in a River Sediment Sample. A Mercury-Free Procedure Employing a Boron-Doped Diamond Electrode. *Electroanalysis* **2001**, *13* (10), 831–835.

(148) Zhang, Q.; Wan, J.; Shangguan, J.; Betzler, S.; Zheng, H. Influence of Sub-Zero Temperature on Nucleation and Growth of Copper Nanoparticles in Electrochemical Reactions. *IScience* **2021**, *24* (11).

(149) Yan, K.; Wang, J.; Zhao, S.; Zhou, D.; Sun, B.; Cui, Y.; Wang, G. Temperature-Dependent Nucleation and Growth of Dendrite-Free Lithium Metal Anodes. *Angew. Chem.* **2019**, *131* (33), 11486–11490.

(150) Vereecken, P. M.; Radisic, A.; Ross, F. M. Differential Inhibition during Cu Electrodeposition on Ru: Combined Electrochemical and Real-Time TEM Studies. *J. Electrochem. Soc.* **2019**, *166* (1), D3129–D3135.

(151) Chmielowiec, B.; Cai, T.; Allanore, A. Simultaneous Spatial and Temporal Measurements of the Current Distribution in a Miniature Hull Cell. *J Electrochem. Soc.* **2016**, *163* (5), E142–E146.

(152) Price, D. C.; Davenport, W. G. Densities, Electrical Conductivities and Viscosities of CuSO4/H2SO4 Solutions in the Range of Modern Electrorefining and Electrowinning Electrolytes. *Metall. Trans. B* **1980**, *11*, 159–163.

(153) Petersen, H. A.; Miller, E. N.; Pham, P. H.; Katsirubas, J. L.; Koltunski, H. J.; Luca, O. R. On the Temperature Sensitivity of Electrochemical Reaction Thermodynamics. *ACS Phys. Chem. Au.* **2023**, *3* (3), 241–251.

(154) Electrode, S. C. Standard Electrode Potentials and Temperature Coefficients in Water at 298.15 K. *J. Phys. Chem. Ref. Data* **1989**, *18* (1), 1–21.

(155) Moats, M. S.; Hiskey, J. B.; Collins, D. W. Effect of Copper, Acid, and Temperature on the Diffusion Coefficient of Cupric Ions in Simulated Electrorefining Electrolytes. *Hydrometallurgy* **2000**, *56* (3), 255–268.

(156) Emanuel, A.; Olander, D. R. Diffusion Coefficients of Copper Sulfate in Water and Water in N-Butyl Alcohol. *J. Chem. Eng. Data* **1963**, *8* (1), 31–32.

(157) Enterkin, J. A.; Poeppelmeier, K. R.; Marks, L. D. Oriented Catalytic Platinum Nanoparticles on High Surface Area Strontium Titanate Nanocuboids. *Nano Lett.* **2011**, *11* (3), 993–997.

(158) Huang, Y.; Duan, X.; Wei, Q.; Lieber, C. M. Directed Assembly of One-Dimensional Nanostructures into Functional Networks. *Science* **2001**, *291* (5504), 630–633.

(159) Li, W.; Huang, L.; Tringides, M. C.; Evans, J. W.; Han, Y. Thermodynamic Preference for Atom Adsorption on versus Intercalation into Multilayer Graphene. *J. Phys. Chem. Lett.* **2020**, *11* (22), 9725–9730.

(160) Zhong, J. H.; Liu, J. Y.; Li, Q.; Li, M. G.; Zeng, Z. C.; Hu, S.; Wu, D. Y.; Cai, W.; Ren, B. Interfacial Capacitance of Graphene: Correlated Differential Capacitance and in Situ Electrochemical Raman Spectroscopy Study. *Electrochim. Acta* **2013**, *110*, 754–761.

(161) Viinikanoja, A.; Wang, Z.; Kauppila, J.; Kvarnström, C. Electrochemical Reduction of Graphene Oxide and Its in Situ Spectroelectrochemical Characterization. *Phys. Chem. Chem. Phys.* **2012**, *14* (40), 14003–14009.

(162) Chiang, Y.-M.; Birnie, D. P.; Kingery, W. D. Physical Ceramics: Principles for Ceramic Science and Engineering. John Wiley & Sons: New York, **1997**.

(163) Schneider, N. M.; Park, J. H.; Grogan, J. M.; Steingart, D. A.; Bau, H. H.; Ross, F. M. Nanoscale Evolution of Interface Morphology during Electrodeposition. *Nat. Commun.* **2017**, *8* (1), 2174.

(164) Nguyen, C. T.; Kim, B. H. Stress and Surface Tension Analyses of Water on Graphene-Coated Copper Surfaces. *Int. J. Precis. Eng. Manuf.* **2016**, *17* (4), 503–510.

(165) Tang, M.; Yuan, W.; Ou, Y.; Li, G.; You, R.; Li, S.; Yang, H.; Zhang, Z.; Wang, Y. Recent Progresses on Structural Reconstruction of Nanosized Metal Catalysts via Controlled-Atmosphere Transmission Electron Microscopy: A Review. *ACS Catal.* **2020**, *10* (24), 14419–14450.

(166) Wei, S.; Li, A.; Liu, J. C.; Li, Z.; Chen, W.; Gong, Y.; Zhang, Q.; Cheong, W. C.; Wang, Y.; Zheng, L.; Xiao, H.; Chen, C.; Wang, D.; Peng, Q.; Gu, L.; Han, X.; Li, J.; Li, Y. Direct Observation of Noble Metal Nanoparticles Transforming to Thermally Stable Single Atoms. *Nat. Nanotechnol.* **2018**, *13* (9), 856–861.

(167) Dai, S.; Zhang, S.; Katz, M. B.; Graham, G. W.; Pan, X. In Situ Observation of Rh-CaTiO3 Catalysts during Reduction and Oxidation Treatments by Transmission Electron Microscopy. *ACS Catal.* **2017**, *7* (3), 1579–1582.

(168) Frey, H.; Beck, A.; Huang, X.; Bokhoven, J. A. Van; Willinger, M. G. Dynamic Interplay between Metal Nanoparticles and Oxide Support under Redox Conditions. *Science* **2022**, *376* (6596), 982–987.

(169) Yu, K.; Li, C.; Xie, J.; Ferreira, P. J. Understanding the Degradation Mechanisms of Pt Electrocatalysts in PEMFCs by Combining 2D and 3D Identical Location TEM. *Nano Lett.* **2023**, *23* (5), 1858–1864.

(170) Egerton, R.; Hwang, S.; Zhu, Y. Atomic-Scale Secondary-Electron Imaging in the STEM and SEM. *Microsc. Microanal.* **2023**, *29* (1), 452–453.

(171) Katsuhiro; Hosoki, S. ; Komoda, T. Observation of Tungsten Field Emitter Tips with an Ultra-High Resolution Field Emission Scanning Electron Microscope. *Scanning Microsc*. **1987**, *1* (3), 4.

(172) Zhu, Y.; Inada, H.; Nakamura, K.; Wall, J. Imaging Single Atoms Using Secondary Electrons with an Aberration-Corrected Electron Microscope. *Nat. Mater.* **2009**, *8* (10), 808–812.

(173) Pirjamali, M.; Kiros, Y. Effects of Carbon Pretreatment for Oxygen Reduction in Alkaline Electrolyte. *J Power Sources* **2002**, *109* (2), 446–451.

(174) Angelucci, M.; Novelli, A.; Spallino, L.; Liedl, A.; Larciprete, R.; Cimino, R. Minimum Thickness of Carbon Coating for Multipacting Suppression. *Phys. Rev. Res.* **2020**, *2* (3), 023030.

(175) Willsau, J.; Heitbaum, J. The Influence of Pt-Activation on the Corrosion of Carbon in Gas Diffusion Electrodes-A DEMS Study. *J. Electroanal. Chem. Interfacial Electrochem.* **1984**, *161* (1), 93–101.

(176) Hodnik, N.; Dehm, G.; Mayrhofer, K. J. J. Importance and Challenges of Electrochemical in Situ Liquid Cell Electron Microscopy for Energy Conversion Research. *Acc. Chem. Res.* **2016**, *49* (9), 2015–2022.

(177) Sun, S.; Zhang, G.; Geng, D.; Chen, Y.; Li, R.; Cai, M.; Sun, X. A Highly Durable Platinum Nanocatalyst for Proton Exchange Membrane Fuel Cells: Multiarmed Starlike Nanowire Single Crystal. *Angew. Chem., Int. Ed.* **2011**, *50* (2), 422–426.

(178) Lin, R.; Cai, X.; Zeng, H.; Yu, Z. Stability of High-Performance Pt-Based Catalysts for Oxygen Reduction Reactions. *Adv. Mater.* **2018**, *30* (17), 1705332.

(179) Altantzis, T.; Lobato, I.; De Backer, A.; Béché, A.; Zhang, Y.; Basak, S.; Porcu, M.; Xu, Q.; Sánchez-Iglesias, A.; Liz-Marzán, L. M.; Van Tendeloo, G.; Van Aert, S.; Bals, S. Three-Dimensional Quantification of the Facet Evolution of Pt Nanoparticles in a Variable Gaseous Environment. *Nano Lett.* **2019**, *19* (1), 477–481.

(180) Ramos-Sanchez, G.; Balbuena, P.B. Interactions of Platinum Clusters with a Graphite Substrate. *Phys. Chem. Chem. Phys*. **2013**, *15* (28), 11950–11959.

(181) Luo, L.; Engelhard, M. H.; Shao, Y.; Wang, C. Revealing the Dynamics of Platinum Nanoparticle Catalysts on Carbon in Oxygen and Water Using Environmental TEM. *ACS Catal.* **2017**, *7* (11), 7658–7664.

(182) Raju, M.; Duin, A. C. T. Van; Fichthorn, K. A. Mechanisms of Oriented Attachment of TiO 2 Nanocrystals in Vacuum and Humid Environments: Reactive Molecular Dynamics. *Nano Lett* .**2014**, *14* (4), 1836–1842.

(183) Fujitani, T.; Nakamura, I.; Takahashi, A. H2O Dissociation at the Perimeter Interface between Gold Nanoparticles and TiO2 Is Crucial for Oxidation of CO. *ACS Catal.* **2020**, *10* (4), 2517–2521.

(184) Yuan, W.; Zhu, B.; Li, X.; Hansen, T. W.; Ou, Y.; Fang, K.; Yang, H.; Zhang, Z.; Wagner, J. B.; Gao, Y.; Wang, Y. Visualizing H2O Molecules Reacting at TiO2 Active Sites with Transmission Electron Microscopy. *Science* **2020**, *367* (6476), 428–430.

(185) Kostoglou, N.; Liao, C.; Wang, C.; Kondo, J. N.; Tampaxis, C.; Steriotis, T.; Giannakopoulos, K.; Kontos, A. G.; Hinder, S.; Baker, M.; Bousser, E.; Matthews, A.;

Rebholz, C.; Mitterer, C. Effect of Pt Nanoparticle Decoration on the H2 Storage Performance of Plasma-Derived Nanoporous Graphene. *Carbon* **2021**, *171*, 294–305.

(186) Bernardet, P.; Franco, A. A.; Lemaire, O.; Gelin, P. Study of CO and Hydrogen Interactions on Carbon-Supported Pt Nanoparticles by Quadrupole Mass Spectrometry and Operando Diffuse Reflectance FTIR Spectroscopy. *J. Phys. Chem. C* **2013**, *117* (44), 22756–22767.

(187) Rossmeisl, J.; Nørskov, J. K.; Taylor, C. D.; Janik, M. J.; Neurock, M. Calculated Phase Diagrams for the Electrochemical Oxidation and Reduction of Water over Pt(111). *J. Phys. Chem. C B* **2006**, *110* (43), 21833–21839.

(188) Baddour, R. F.; Iwasyk1, J. M. Reactions Between Elemental Carbon and Hydrogen at Temperatures above 2800° K. *Ind. Eng. Chem. Process Des. Dev*. **1962**, *1* (3), 169-176.

(189) Guo, Z.; Fu, Z.; Wang, S. Sulfur Distribution in Coke and Sulfur Removal during Pyrolysis. *Fuel Process. Technol.* **2007**, *88* (10), 935–941.

(190) Lin, B.; Mallaye, M.; Mallah, A.; Huang, Q.; Ali, M.; Chi, Y. Effects of Temperature and Potassium Compounds on the Transformation Behavior of Sulfur during Pyrolysis of Oily Sludge. *Energy Fuels* **2017**, *31* (7), 7004–7014.

(191) Zhang, W.; Hein Alsem, D.; Salmon, N.; Wang, F. In-Situ Liquid Cell TEM Studies of Electrochemical Reactions in Lithium-Ion Batteries. *Microsc. Microanal.* **2015**, *21* (S3), 2431–2432.

(192) Sun, Y.; Xia, Y. Shape-Controlled Synthesis of Gold and Silver Nanoparticles. *Science* **2002**, *298* (5601), 2176–2179.

(193) Xu, K. Nonaqueous Liquid Electrolytes for Lithium-Based Rechargeable Batteries. *Chem. Rev.* **2004**, *104* (10), 4303–4418.

(194) Nanjundiah, C.; Goldman, J. L.; Dominey, L. A.; Koch, V. R. Electrochemical Stability of LiMF6 (M= P, As, Sb) in Tetrahydrofuran and Sulfolane. *J. Electrochem. Soc.* **1988**, *135* (12), 2914.

(195) Peled, E.; Golodnitsky, D.; Menachem, C.; Bar-Tow, D. An Advanced Tool for the Selection of Electrolyte Components for Rechargeable Lithium Batteries. *J. Electrochem. Soc.* **1998**, *145* (10), 3482.

(196) Abellan, P.; Mehdi, B. L.; Parent, L. R.; Gu, M.; Park, C.; Xu, W.; Zhang, Y.; Arslan, I.; Zhang, J. G.; Wang, C. M.; Evans, J. E.; Browning, N. D. Probing the Degradation Mechanisms in Electrolyte Solutions for Li-Ion Batteries by in Situ Transmission Electron Microscopy. *Nano Lett.* **2014**, *14* (3), 1293–1299.

(197) Myland, J. C.; Oldham, K. B. A Model of Cyclic Voltammetry for a Thin Organic Layer Sandwiched between an Electrode and an Aqueous Solution. Convolutive Modelling in the Absence of Supporting Electrolyte. *J. Electroanal. Chem*. **2002**, *530* (1–2), 1–9.

(198) Liu, T.; Wang, J.; Yang, X.; Gong, M. A Review of Pulse Electrolysis for Efficient Energy Conversion and Chemical Production. *J. Energy Chem.* **2021**, *59*, 69–82.

(199) Kim, C.; Weng, L. C.; Bell, A. T. Impact of Pulsed Electrochemical Reduction of CO2on the Formation of C2+Products over Cu. *ACS Catal.* **2020**, *10* (21), 12403–12413.

(200) Kimura, K. W.; Fritz, K. E.; Kim, J.; Suntivich, J.; Abruña, H. D.; Hanrath, T. Controlled Selectivity of CO2 Reduction on Copper by Pulsing the Electrochemical Potential. *ChemSusChem* **2018**, *11* (11), 1781–1786.

(201) Xu, L.; Ma, X.; Wu, L.; Tan, X.; Song, X.; Zhu, Q.; Chen, C.; Qian, Q.; Liu, Z.; Sun, X.; Liu, S.; Han, B. In Situ Periodic Regeneration of Catalyst during CO 2 Electroreduction to C2+ Products. *Angew. Chem.* **2022**, *134* (37), 2–9.

(202) Casebolt, R.; Levine, K.; Suntivich, J.; Hanrath, T. Pulse Check: Potential Opportunities in Pulsed Electrochemical CO2 Reduction. *Joule* **2021**, *5* (8), 1987–2026.

(203) Bui, J. C.; Kim, C.; Weber, A. Z.; Bell, A. T. Dynamic Boundary Layer Simulation of Pulsed CO2Electrolysis on a Copper Catalyst. *ACS Energy Lett.* **2021**, *6* (4), 1181–1188.

(204) Pu, S. D.; Gong, C.; Gao, X.; Ning, Z.; Yang, S.; Marie, J. J.; Liu, B.; House, R. A.; Hartley, G. O.; Luo, J.; Bruce, P. G.; Robertson, A. W. Current-Density-Dependent Electroplating in Ca Electrolytes: From Globules to Dendrites. *ACS Energy Lett.* **2020**, *5* (7), 2283–2290.

(205) Jiang, W.; Low, B. Q. L.; Long, R.; Low, J.; Loh, H.; Tang, K. Y.; Chai, C. H. T.; Zhu, H.; Zhu, H.; Li, Z.; Loh, X. J.; Xiong, Y.; Ye, E. Active Site Engineering on Plasmonic Nanostructures for Efficient Photocatalysis. *ACS Nano* **2023**, *17* (5), 4193–4229.

(206) Verma, R.; Belgamwar, R.; Polshettiwar, V. Plasmonic Photocatalysis for CO2Conversion to Chemicals and Fuels. *ACS Mater. Lett.* **2021**, *3* (5), 574–598.

(207) Dong, Y.; Hu, C.; Xiong, H.; Long, R.; Xiong, Y. Plasmonic Catalysis: New Opportunity for Selective Chemical Bond Evolution. *ACS Catal.* **2023**, *13* (10), 6730–6743.

(208) Swearer, D. F.; Bourgeois, B. B.; Angell, D. K.; Dionne, J. A. Advancing Plasmon-Induced Selectivity in Chemical Transformations with Optically Coupled Transmission Electron Microscopy. *Acc. Chem. Res.* **2021**, *54* (19), 3632–3642.

(209) Baldi, A.; Narayan, T. C.; Koh, A. L.; Dionne, J. A. In Situ Detection of Hydrogen-Induced Phase Transitions in Individual Palladium Nanocrystals. *Nat. Mater.* **2014**, *13* (12), 1143–1148.

(210) Angell, D. K.; Bourgeois, B.; Vadai, M.; Dionne, J. A. Lattice-Resolution, Dynamic Imaging of Hydrogen Absorption into Bimetallic AgPd Nanoparticles. *ACS Nano* **2022**, *16* (2), 1781–1790.

(211) Sytwu, K.; Vadai, M.; Hayee, F.; Angell, D. K.; Dai, A.; Dixon, J.; Dionne, J. A. Driving Energetically Unfavorable Dehydrogenation Dynamics with Plasmonics. *Science* **2021**, *371* (6526), 280–283.

(212) Vadai, M.; Angell, D. K.; Hayee, F.; Sytwu, K.; Dionne, J. A. In-Situ Observation of Plasmon-Controlled Photocatalytic Dehydrogenation of Individual Palladium Nanoparticles. *Nat. Commun.* **2018**, *9* (1), 4658.

(213) Karagoz, B.; Carpena-Núñez, J.; Zhu, Y.; Baker, L.; Attenkofer, K.; Maruyama, B.; Stacchiola, D.; Zakharov, D. N.; Head, A. R. Adapting an Electron Microscopy Microheater for Correlated and Time-Resolved Ambient Pressure X-Ray Photoelectron Spectroscopy. *Chem. Mater.* **2023**, *35* (15), 5744–5751.